NASA Contractor Report 4483

Discrimination of Ionic Species From Broad-Beam Ion Sources

J. R. Anderson
Colorado State University
Fort Collins, Colorado

Prepared for
George C. Marshall Space Flight Center
under Grant NGT-50370

National Aeronautics and
Space Administration

Office of Management

Scientific and Technical
Information Program

1993

TABLE OF CONTENTS

LIST OF FIGURES

LIST OF TABLES

I. INTRODUCTION

Satellites in low-Earth-orbit, about 200-400 km altitude, encounter a rarified atmosphere which consists primarily of atomic oxygen, produced by solar radiation induced photo-dissociation of diatomic oxygen, and diatomic nitrogen. Since the gases are in thermal equilibrium, the speed distribution of the less massive atomic oxygen is skewed to higher speeds than the more massive diatomic nitrogen. As a result, only a small fraction of the most energetic diatomic nitrogen can reach elevations accessible to atomic oxygen. Therefore, the main constituent of the low-Earth-orbit atmosphere is atomic oxygen.

In order to be serviced by the space shuttle, the proposed space station Freedom, which is intended to operate for several years, must be placed in low-Earth-orbit. There is concern about how the chemically active atomic oxygen will affect the exposed surfaces of the space station. This concern arises because tests, conducted in low-Earth-orbit, have demonstrated that high-energy oxygen atoms strike the surfaces of spacecraft at a sufficiently high rate to cause some spacecraft materials to erode rapidly [1,2]. The speed of these atoms relative to the spacecraft, which is determined by the spacecraft orbital speed, corresponds to an atomic oxygen kinetic energy near 5 eV.

In order for the space station to operate for many years in low-Earth-orbit, protective coatings or materials resistant to atomic oxygen attack must be used for the exposed surfaces. To evaluate the suitability of various spacecraft materials that might be exposed to this oxygen flux, it is desirable to have an earth-based facility that can produce a broad beam of 5 eV atomic oxygen at low-Earth-orbit flux levels

(10^{14} to 10^{16} oxygen atoms per second per square centimeter [3]).

Several approaches have been used in attempts to simulate the low-Earth-orbit environment [4]. Reference [4] lists thirty-three facilities and gives a brief description of the methods used in each. There are two basic types of systems: thermal and electric. In the thermal systems diatomic oxygen is heated and some of it is dissociated with either a laser or an electric discharge. The gas is then expanded through a nozzle and directed onto the material being tested. The major drawback of these systems is that the kinetic energies achieved are less than 1 eV. Also diatomic oxygen is mixed in with the atomic oxygen.

In the electrical systems, atomic and diatomic oxygen ions are produced in either an arc discharge or a microwave discharge. To achieve energies greater than 1 eV these ions are accelerated electrostatically. Because it is difficult to control beams with ions having kinetic energies in the few eV range, many of the systems direct beams having tens to several thousand eV energies onto the sample of the material being tested.

In the simplest schemes both atomic and diatomic ions are directed onto the sample. More sophisticated systems either charge neutralize the ions or filter out the diatomic ions before directing the beam onto the sample. The most sophisticated systems either try to produce a pure atomic oxygen ion plasma or filter out the diatomic ion component of the beam and then charge neutralize the atomic oxygen to produce a pure oxygen-atom beam.

Before describing schemes for separation of diatomic and atomic oxygen ions, charge neutralization will be discussed briefly. Charge neutralization of atomic oxygen can be accomplished using grazing incidence impact with a polished metal surface [5,6,7]. If ions approach the metal plate at incidence angles of less than 2°, 40 to 50% of the ions can pick up an electron and reflect off the surface with

virtually no loss of kinetic energy [5]. It is also possible to charge neutralize ions approaching a metal plate at larger incidence angles, but these ions will lose kinetic energy while interacting with the surface. Theoretical computations have estimated the percentage of atomic ions impinging normal to a metal plate which are reflected and charge neutralized to be between 40 and 60% at incident energies between 10 and 50 eV [8]. These calculations also predict that ions approaching a molybdenum plate at normal incidence with a kinetic energy of 15 eV will be reflected at energies ranging from zero to 11 eV with the peak of the distribution at 6 eV.

Typically, separation of the atomic and diatomic ions is accomplished with a magnetic lens. Magnetic lenses are often used in ion accelerators [9,10,11] where ions have keV energies. Such systems tend to be large and ions must travel relatively long distances between the ion source and the target. These systems are designed to focus ions at or near the center of the beam onto the target; however, ions near the edges of the beam or ions on divergent trajectories will be lost. The performance of a magnetic lens is expected to be worse at low energies because ions take longer to travel from the source to the target. This would allow the mutually repulsive forces between ions to act for a longer time and this would cause increased beam divergence, resulting in larger loses.

This dissertation describes the experimental investigation of an alternative concept for separating diatomic and atomic oxygen ions. The alternative mass discrimination scheme is based on a single-stage Bennett mass spectrometer [12] which uses a radio frequency (RF) voltage signal to accomplish mass separation. First, a theoretical description of the single-stage Bennett mass spectrometer which predicts the energy of ions being extracted from it is given. Then experimental results, which demonstrate that the single-stage Bennett mass spectrometer operation agrees essentially with the theoretical predictions, are described. However, problems

with efficient extraction of ions using the single-stage Bennett mass spectrometer prompted design changes. The resulting device, which combines the function of a three-grid optics system [13] and the single-stage Bennett mass spectrometer, has been named the three-grid optics/RF mass discriminator. Next, experiments demonstrating that diatomic oxygen ions can be filtered out of the beam in the three-grid optics/RF mass discriminator are discussed. In addition, atomic oxygen ion energy, current density and beam divergence data are also presented. Finally, a configuration which could incorporate the charge-exchange process into the three-grid optics/RF mass discriminator is proposed.

II. THEORY OF ION EXTRACTION AND MASS DISCRIMINATION SYSTEM OPERATION

Before describing the three-grid optics/RF mass discriminator system, it is instructive to discuss how a single-stage Bennett mass spectrometer might be used to accomplish mass discrimination. A single-stage Bennett mass spectrometer has three, equally-spaced grids and is configured as shown in Fig. 1a. All three grids are held at a prescribed mean electric potential and a sinusoidal, RF voltage like the one illustrated in Fig. 1b is applied to grid 2. In order to understand the principle of operation of the device, consider the effect of this RF signal on an atomic and a diatomic ion represented, respectively, in Fig. 1a by the smaller and larger circles. Assuming both ions are drawn from the same ion source (i.e. accelerated through the same potential difference), the more massive diatomic ion will enter the system at a lower velocity, as its velocity vector suggests. Consider the case where both ions pass through grid 1 at time zero when the RF voltage on grid 2 begins to go positive. The electric field set up between these grids will cause the ions to decelerate as they travel toward grid 2. If the radio frequency is selected so that the atomic ion reaches grid 2 one-half cycle later as the voltage goes negative, the electric field between grids 2 and 3 will cause it to continue to decelerate as it travels toward grid 3. However, the diatomic ion, which is travelling slower, will not have reached grid 2 after half an RF cycle; therefore, after the potential on grid 2 goes negative, it will see an accelerating field until it reaches grid 2. The diatomic ion will also accelerate for a portion of the time it is between grids 2 and 3. As a result, at these particular conditions, the atomic ion will lose more kinetic energy than the diatomic one does

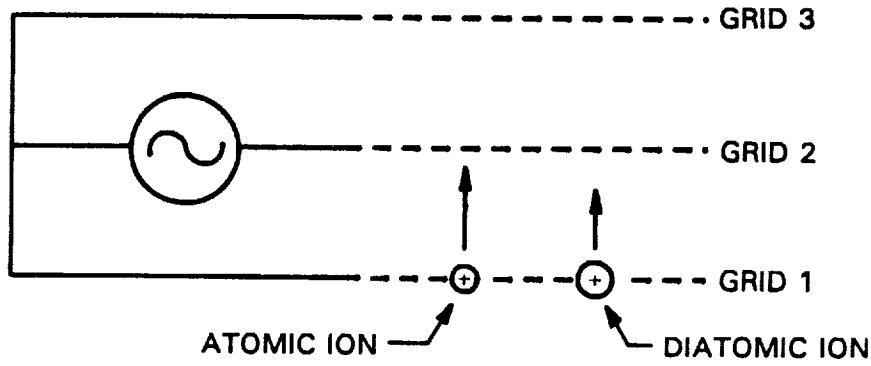

a. Grid System Arrangement

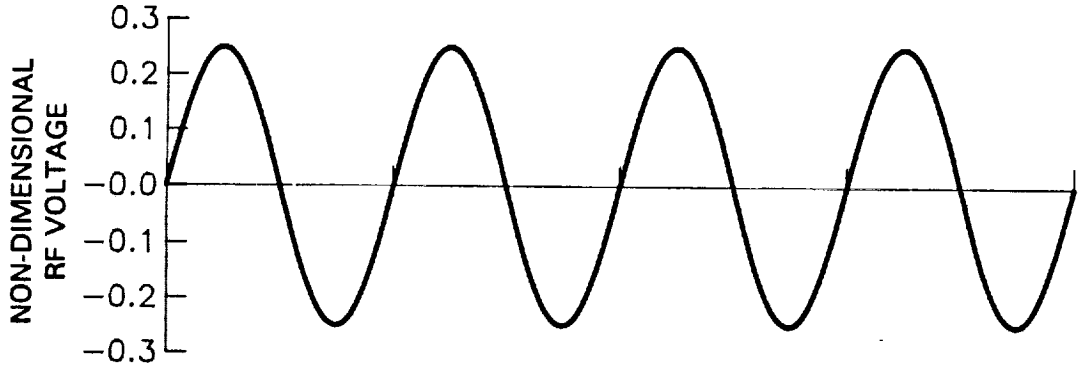

b. RF Voltage Applied to Grid 2

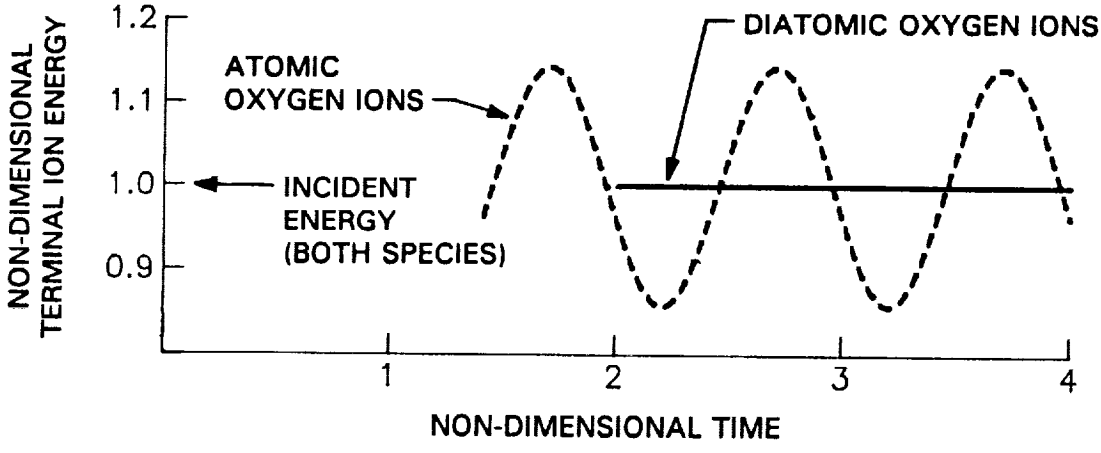

c. Energy of Ions Exiting Grid 3

Fig. 1 Single-Stage Bennett Mass Spectrometer

during its passage through the grids. Although the operating conditions just described are not the optimum conditions for separating atomic and diatomic oxygen, this tendency for atomic and diatomic ions to experience different kinetic energy changes is exploited to effect mass discrimination.

In operation, a steady stream (or beam) of atomic and diatomic ions is fed into the single-stage Bennett mass spectrometer. Depending on the phase of the RF signal when an ion enters the spectrometer, it could emerge at grid 3 with more, the same, or less kinetic energy than it had when it entered. Figure 1c shows the energies of atomic and diatomic oxygen ions as a function of the time at which they emerge from the third grid. In order to determine this time variation of the energies of the emerging ions, a simple, one-dimensional model of the intra-grid acceleration process has been developed (Appendix A). The model enables one to compute the kinetic energy at which ions emerge from the third grid, which is referred to as the terminal ion energy.

The model is cast in terms of non-dimensional variables which are convenient to describe the system. The non-dimensional kinetic energy (ξ) is the actual ion energy divided by the energy that ions have when they arrive at grid 3 when no RF signal is applied. When the RF signal is not applied, there are no time varying voltages so the system operates in a steady-state condition. During non-steady operation the kinetic energy will oscillate about the steady-state value. Non-dimensional voltage (ν) is the actual voltage divided by the difference between discharge chamber plasma potential (i.e. the potential at which ions are created) and the mean potential applied to grid 2. Non-dimensional frequency (F) is the actual frequency multiplied by the time it takes a diatomic oxygen ion to travel between grids 1 and 2 when the system is operated at steady-state. Non-dimensional time (T) is the actual time divided by the time it takes a diatomic oxygen ion to travel between

grids 1 and 2 during steady-state operation. Non-dimensional ion mass (M) is the actual ion mass divided by the mass of a diatomic oxygen ion and non-dimensional charge (Q) is the actual charge divided by the magnitude of the electron charge (e).

Before continuing the discussion, it is noted that these non-dimensional variables will be used throughout the dissertation. Unless otherwise stated, it is to be implicitly understood that the non-dimensional values are being referred to when energy, potential, frequency, mass, charge and time are used.

One additional parameter, the effective frequency for a particular species, is also useful. The effective frequency for a given species is defined as the mean number of cycles an ion experiences as it travels between grids 1 and 2. This is equal to the frequency (F) multiplied by the time it takes an ion of the species being considered to travel from grid 1 to grid 2 at steady-state (τ)[1]. In Appendix A it is shown that this transit time is related to the charge-to-mass ratio through

$$\tau = \sqrt{\frac{M}{Q}} \quad . \tag{1}$$

Since the charge-to-mass ratio is 1 for singly ionized diatomic oxygen, the frequency (F) is equal to the effective frequency ($F\tau$) for diatomic oxygen. When the spectrometer is operating, the frequency (F) is held fixed; however, because each species has a different charge-to-mass ratio, their velocities are different resulting in different transit times for each species. Consequently, the effective frequency is different for each species travelling through the system.

A first-order model, using the RF voltage as a perturbation to the steady-state solution, has been developed to determine the terminal ion energy (Appendix A). The

[1]Since the single-stage Bennett mass spectrometer grids are equally spaced and at the same mean potential, the time it take an ion to travel from grid 2 to grid 3 at steady-state is also τ.

first-order solution for the terminal ion energy is

$$\xi = 1 + \nu_{RF}\, \psi(F\tau)\, \sin[2\pi FT + \delta(F\tau)] \qquad (2)$$

where ψ, the energy spread parameter, depends on the effective frequency ($F\tau$) for a given species. The phase shift between the sinusoidal RF signal and the terminal ion energy, which is also a function of the effective frequency for a particular species, is denoted by δ. The equations for both ψ and δ are given in Appendix A. Since the sine function varies between ± 1, the product of the function ψ and the RF voltage (ν_{RF}) gives, to first order, the maximum variation of the terminal ion energy.

The energy spread parameter ψ is plotted as a function of the effective frequency ($F\tau$) in Fig. 2. If a single-stage Bennett mass spectrometer is to be used to separate atomic and diatomic oxygen ions, the system is operated so that the effective frequency for diatomic ions is unity and that for atomic ions is $\sqrt{0.5}$ as labeled in Fig. 2. Since $\tau=1$ for singly ionized diatomic oxygen, the frequency is fixed at unity ($F=1$). From the plot in Fig. 2 it is evident that $\psi(1.0) = 0$. Plugging this into Eq. 2 shows that, to first order, the diatomic oxygen ions emerge from the system as a mono-energetic group with an energy of unity. The reason the diatomic ions emerge as a mono-energetic group is that, to first order, all the diatomic ions take two full RF cycles to travel between grids 1 and 3. Because of this they experience the same amount of acceleration and deceleration, causing them to emerge with same energy they had when they entered the system[2]. Since atomic oxygen has half the mass of diatomic oxygen, the mass-to-charge ratio for singly ionized atomic oxygen ions is 0.5; therefore, the effective frequency for atomic oxygen ions is $\sqrt{0.5}$ (~ 0.71). From Fig. 2 it is seen that $\psi(0.71) = 0.57$. Using this value and an RF voltage (ν_{RF}) of 0.25 in Eq. 2, the terminal ion energies of the atomic oxygen ions are seen to

[2]The model assumes that a mono-energetic group of ions enters the system.

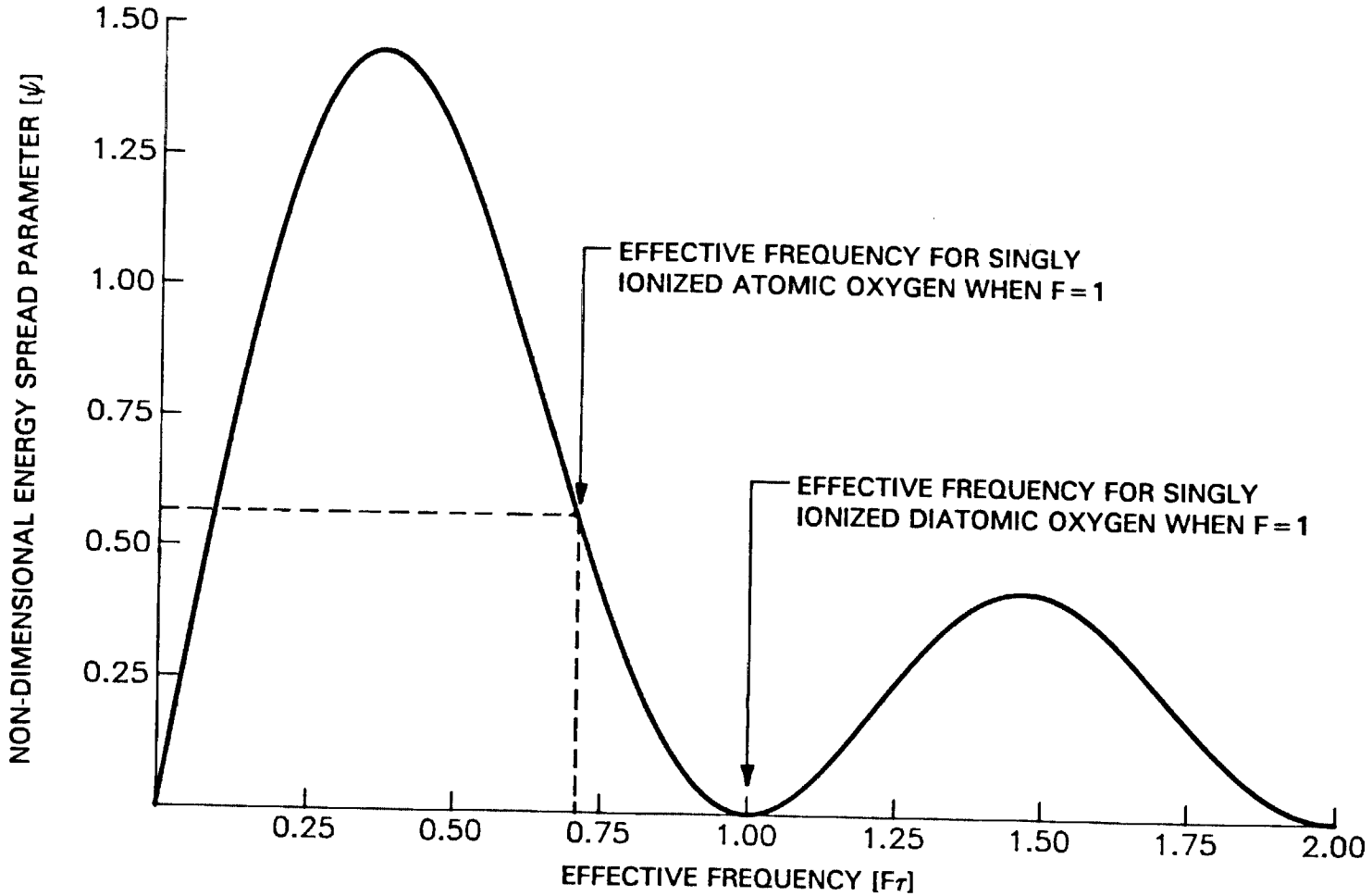

Fig. 2 First-Order Energy Spread Parameter

vary, to first order, between 0.86 to 1.14. The reason that atomic ions have a spread induced in their energies is that they do not experience an integer number of RF cycles through the single-stage Bennett mass spectrometer. Consequently, some of the ions experience more acceleration and some more deceleration, depending on the phase of the RF signal when they enter the system. As a result, a significant spread of atomic ion energies is induced in the system.

Figure 1c shows a plot of the terminal energy for atomic and diatomic ions, predicted by the first-order solution, as a function of the time at which they emerge from the system. This plot was made assuming that a mono-energetic group of ions begins entering the single-stage Bennett mass spectrometer at time zero. Since, to first order, diatomic ions take two RF cycles to travel through the system, the first diatomic ions emerge after two periods. The atomic ions, however, take about 0.7 periods to travel between each pair of grids. Therefore, the atomic ions that entered the single-stage Bennett mass spectrometer at time zero emerge after about 1.4 periods. Ions that enter the system later also exit at later times and the variation of their terminal energies with time are shown in Fig. 1c. It is evident that the atomic ions have a significant energy spread when they exit, while the atomic ions emerge as a mono-energetic group.

In order to understand how the energy dispersion introduced to the atomic ions can be used to effect mass discrimination, consider Fig. 3a. This figure shows the single-stage Bennett mass spectrometer connected to a filtering grid and power supply which can be used to adjust its potential. A mono-energetic beam of atomic and diatomic oxygen ions with an energy of unity enters the single-stage Bennett mass spectrometer where their energies are perturbed before they travel on to the filtering grid.

Figure 3b shows the effect of filtering potential on time-averaged, filtered-

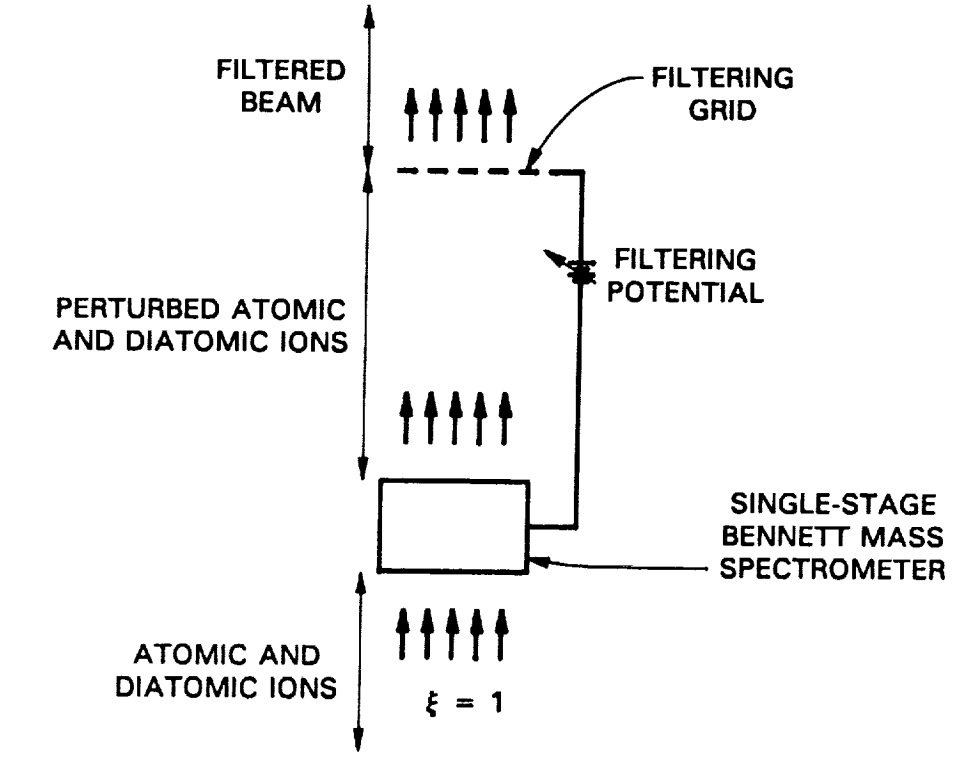

a. Physical System

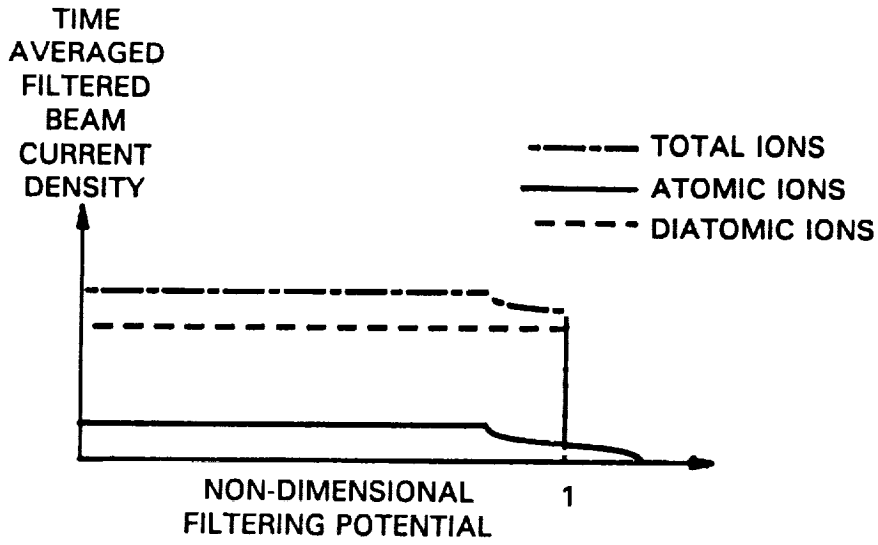

b. Frequency Selected to Perturb Atomic but not Diatomic Ions

Fig. 3 Species Selection Using Single-Stage Bennett Mass Spectrometer

beam current densities[3] when the operating conditions for the single-stage Bennett mass spectrometer of Fig. 3a are selected to induce a significant energy change in the atomic ions while not perturbing the energies of the diatomic ions. Shown are the atomic, diatomic and combined (or total) time-averaged, filtered-beam current densities that would be measured downstream of the filtering grid as a function of the potential applied to it. Diatomic oxygen accounts for most of the current because, typically, atomic oxygen accounts for less than 30% of the ions extracted from an arc discharge [14]. At low filtering potentials all of the ions are able to pass through the filtering grid. However, as the filtering potential increases, a point is eventually reached where the kinetic energies of the atomic ions that decelerate the most in the single-stage Bennett mass spectrometer are insufficient to overcome the adverse potential and they are removed from the filtered beam. Further increases in filtering potential cause the fraction of atomic ions removed from the beam to increase. Because the diatomic ions are a mono-energetic group, they are removed abruptly at a filtering potential of unity. At filtering potentials above that needed to stop the diatomic ions, the time-averaged, filtered-beam current density is due to atomic ions only. (This would be the desired operating condition if this system configuration were to be used in the 5 eV atomic oxygen source.) Further increases in filtering potential cause the time-averaged atomic ion current density to decrease and eventually drop to zero.

Two obvious drawbacks to the mass discrimination scheme just described are 1) at most half of the atomic ions drawn from an ion source will pass through the filtering grid onto a sample being tested and 2) the ions that do reach the sample will have an energy spread rather than having the preferred 5 eV mono-energetic

---

[3]Time-averaged, filtered-beam current density is the charge flowing through a unit area of the filtering grid per RF cycle divided by the period of the cycle.

distribution. The energy spread on the ions can be minimized by reducing the amplitude of the radio-frequency voltage, but some energy spread will always occur in a properly operating system. The great advantage of this discrimination concept is that it utilizes a compact combination of optics and mass discrimination system elements. This should minimize the divergence losses that plague magnetic field-induced mass discrimination systems.

III. PRELIMINARY EXPERIMENTS

Experimental Apparatus

The experimental apparatus used to conduct the preliminary investigation of the single-stage Bennett mass spectrometer is shown schematically in Fig. 4. Ions were generated in the 8 cm dia mildly-divergent-magnetic-field discharge chamber shown at the bottom of the figure. The discharge chamber was made with non-magnetic stainless steel and a magnetic field was induced with a solenoidal winding extending the length of the discharge chamber. Additional windings were placed at the back of the discharge chamber so that the magnetic field at the back of the chamber was 1.6 times stronger than it was at the screen grid. This discharge chamber could be run on a variety of source gases which were introduced through two gas injectors placed at the rear of the chamber. The discharge chamber bias supply could be used to bias the chamber with respect to ground. The cylindrical anode was biased with respect to the discharge chamber so that electrons emitted from the heated, tungsten filament cathode acquired the kinetic energy they needed to ionize the gas being used in the chamber. More information on this type of discharge chamber can be found in the literature [15,16,17,18].

Two different grid systems were used to study the single-stage Bennett mass spectrometer; one was a single aperture grid set (shown in Fig. 4) and the other was a 19-hole grid set. With the single aperture grid set, ion acceleration was accomplished using an optics system consisting of a sheath-constraining [19] screen grid and an accel grid. The accel grid could be biased up to 2 kV negative of ground to facilitate ion extraction at a reasonable beam current density level. The sheath-constraining

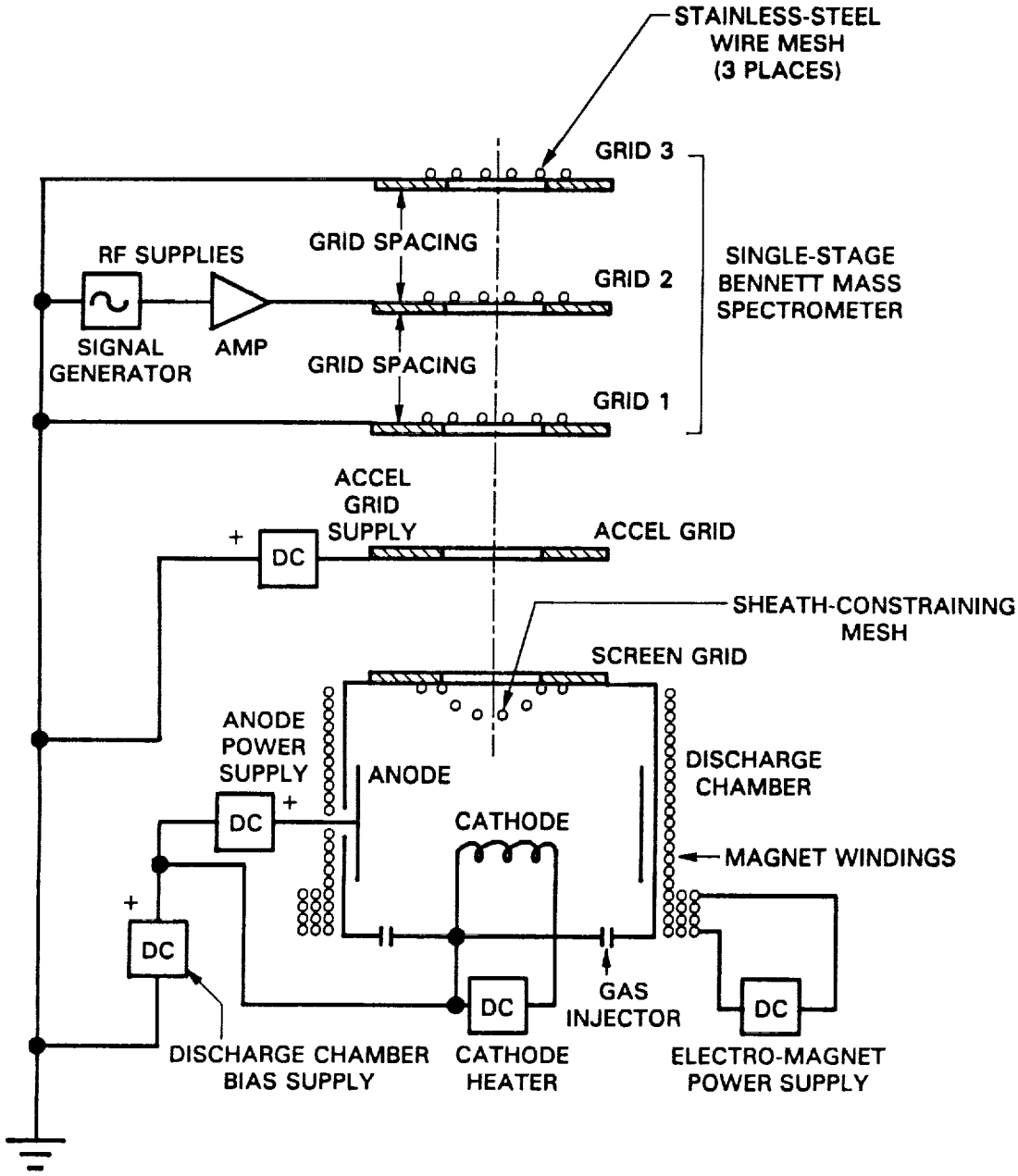

Fig. 4 Experimental Apparatus for Single-Stage Bennett Mass Spectrometer

screen served to control the sheath shape and hence beam divergence under optics system operating conditions where the accel grid was biased very negative. Both the screen and accel grids were made of 1.6 mm thick, 8.9 cm dia stainless steel disks with 2.9 cm dia holes machined at their centers. The sheath-constraining mesh was made by spot welding 0.25 mm dia tungsten wire to form a square mesh with 2 mm wire-to-wire spacing. The mesh was contoured to form a spherical segment over the 2.9 cm dia aperture, as suggested in Fig. 4.

Energy dispersion was induced in the single-stage Bennett mass spectrometer subsystem shown downstream of the accel grid in Fig. 4. The mean potential applied to all of the single-stage Bennett mass spectrometer grids was ground potential. The spectrometer grids were also made of 1.6 mm thick, 8.9 cm dia stainless steel disks with 2.9 cm dia holes machined in their centers. The grids were evenly spaced and grid spacing is defined at the distance between the adjacent faces of neighboring grids. To provide a planar, uniform potential across each of the apertures, stainless-steel wire mesh with a transparency of about 0.8 was spot welded over the aperture of each of the spectrometer grids. The radio-frequency signal applied to grid 2 was the amplified output of a sine-wave signal generator; an RF signal up to 100 V peak-to-peak could be applied.

One drawback to the single-aperture grid set was that about 20% of the current arriving at each of the single-stage Bennett mass spectrometer grids impinged on the wire mesh. Since there was stainless wire screen over three grids, a total of about half ($1-0.8^3$) of the ions supplied to the spectrometer were lost. In order to eliminate this impingement loss, a 19-hole grid set with matching 2 mm dia apertures was made of 0.25 mm thick graphite. Each grid had 19 holes arranged in a hexagonal close-pack pattern with 2.5 mm center-to-center spacing and the grids were aligned coaxially. The grids were used in the same configuration as the single-aperture grid

set; however, a sheath-constraining mesh was not placed over the screen grid holes and wire mesh was not placed over the single-stage Bennett mass spectrometer grid holes. It was anticipated that this would result in lower impingement loses because the ions should have been focused through the holes instead of being lost to the wire meshes.

Two pieces of diagnostic equipment were used during preliminary experiments. A retarding potential analyzer (RPA) was used to measure energy characteristics of the beams extracted from the single-stage Bennett mass spectrometer. A Faraday probe was used to measure current-density profiles of these beams. The RPA, shown in Fig. 5, was used to measure total-time-averaged beam current density as a function of the retarding potential applied to the collector. As this figure suggests, the beam ions passed through a 2 mm dia aperture in the Faraday cage and struck a molybdenum collector. The time-averaged current of these ions was determined by measuring the current of electrons through the ammeter required to neutralize them. The Faraday cage was biased sufficiently far below ground so that electrons in the ambient plasma, which had a Debye length [20] near 1 cm, should have been unable to reach the collector through the 2 mm dia aperture. Although electrons were not expected to pass through the aperture, a small electron current was still measured when the retarding potential was high enough to stop all of the ions. It is believed that these were secondary electrons which were emitted when ions repelled by the collector struck the inside surfaces of the Faraday cage. This secondary electron current was subtracted off the raw RPA data using the method developed in Appendix B. It should be noted that the RPA collector served the function of the filtering grid shown in Fig. 3a and discussed in the related text. Thus,

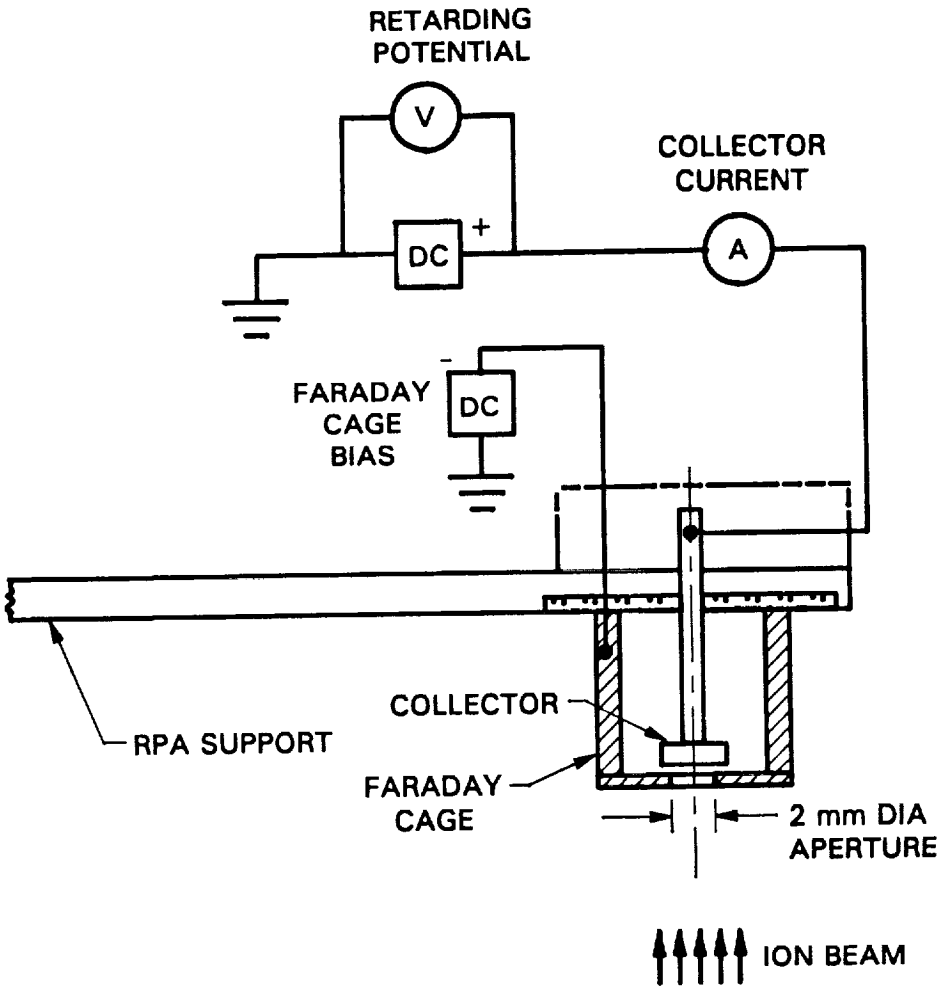

Fig. 5 Retarding Potential Analyzer

the retarding potential applied to the collector and time-averaged current density[4] correspond, respectively, to filtering potential and time-averaged, filtered-beam current density.

The Faraday probe was used to measure time-averaged, beam-current-density profiles which could be integrated to determine the total, time-averaged ion current extracted from the single-stage Bennett mass spectrometer. The Faraday probe shown in Fig. 6 was similar to the RPA of Fig. 5. As with the RPA, beam ions passed through the 2 mm dia aperture and impinged on the collector. However, the collector was held at ground potential and the Faraday probe was swept through the beam in a plane downstream of and parallel to the single-stage Bennett mass spectrometer grids. The current arriving at the collector was measured as a function of position using the position-sensing potentiometer. The Faraday cage was biased negative enough to stop plasma electrons from entering the aperture and impinging on the collector.

Experimental Procedure

Preliminary experiments designed to investigate the performance of the single-stage Bennett mass spectrometer were conducted using argon and krypton ions because they yielded a simple beam (essentially Ar^+ and Kr^+ ions only) with energy characteristics that could be analyzed readily and compared to theoretical predictions. Additional reasons for selecting these gases were that they are chemically inert, their mass ratio (84 a.m.u. to 40 a.m.u.) is about the same as the diatomic-to-atomic oxygen mass ratio and they have similar ionization cross sections (3.67 $Å^2$ for krypton and 2.49 $Å^2$ for argon [21] at the 45 eV discharge voltage used in all testing).

---

[4]The time-averaged current density is equal to the time-averaged ion current impinging on the collector divided by the area of the 2 mm dia aperture in the Faraday cage.

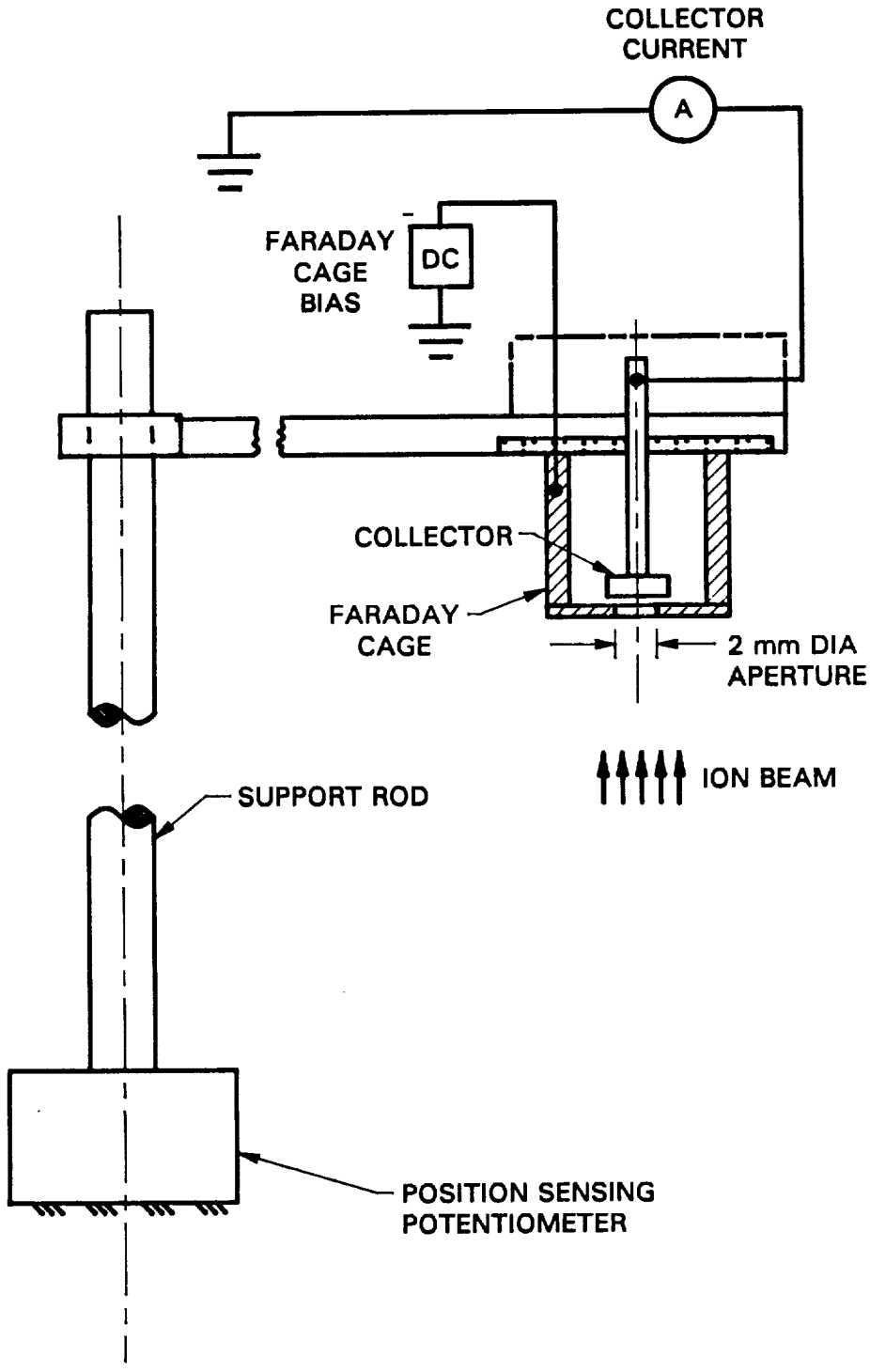

Fig. 6 Faraday Probe

One set of preliminary experiments involved demonstration that a single-stage Bennett mass spectrometer could induce a spread in the energies of one species while introducing a minimal spread in the energies of the other species. In order to obtain results that could be interpreted readily, the tests were conducted using beams extracted with about a 50%-50% mixture of krypton and argon ions. The exact proportions of each gas were controlled to assure operation with approximately equal krypton and argon current densities. This testing was done using the single-aperture grid set and the RPA was used to obtain current density v. retarding potential traces.

The Faraday probe was used, in another set of preliminary experiments, to measure currents extracted from the 19-hole grid set while a time-averaged current balance was performed to determine the magnitude of impingement losses. The system was set up with ammeters so that the time-averaged current to each of the single-stage Bennett mass spectrometer grids could be measured and the Faraday probe was swept through the beam downstream of the grid system. The current density profiles obtained with the Faraday probe were integrated to determine the total current extracted from the spectrometer. In addition, the effect of frequency on impingement currents were studied. All of these tests were conducted using argon only.

All experiments were conducted with the discharge chamber, grid systems and probes located inside a 30 cm dia pyrex vacuum bell jar. Power and the gas being used were fed into the vacuum system with feed-throughs from supplies located outside the bell jar. The bell jar was pumped by a 15 cm dia oil diffusion pump backed by a mechanical pump. Pressures in the bell jar during experiments ranged between 10^{-5} to 10^{-4} Torr.

Experimental Results

Experimental results are presented in terms of non-dimensional frequency,

energy and voltage. However, to identify the actual operating conditions, a pair of dimensional values will be listed on figures where experimental data are shown. One of the dimensional values is the kinetic energy that ions would have when they reach the third grid under steady-state operating conditions; this is termed the mean ion energy. The other dimensional value given is the grid spacing. As discussed in Appendix A, for the single-stage Bennett mass spectrometer, the dimensional operating conditions can be deduced from these two values if the ion species is known. Therefore, both these parameters, along with the source gas used to produce ions, will be listed on figures showing data obtained with the single-stage Bennett mass spectrometer.

Figure 7 shows a typical comparison between theoretical (solid line) and experimental (dashed line) RPA traces and corresponding distribution functions for the 50% krypton-50% argon mixture. The frequency of the signal used in the single-stage Bennett mass spectrometer is selected so the effective frequency for krypton ions is unity. Because krypton has a mass 2.1 times that of argon, the effective frequency for argon is about 0.69 ($\sqrt{1/2.1}$). Theory predicts that the time-averaged current density measured by the RPA remains constant for retarding potentials below about 0.87. Above this, the current begins to drop off as the argon ions that have lost energy in the single-stage Bennett mass spectrometer begin to be repelled by the retarding potential applied to the collector. At retarding potentials near unity, the current drops sharply as krypton ions are repelled from the collector. Further increases in retarding potential cause the theoretical current density to again decrease gradually as the argon ions that gained energy in the single-stage Bennett mass spectrometer are repelled.

The ion energy distribution function is proportional to the negative of the first derivative of the RPA trace and inversely proportional to the square root of the ion

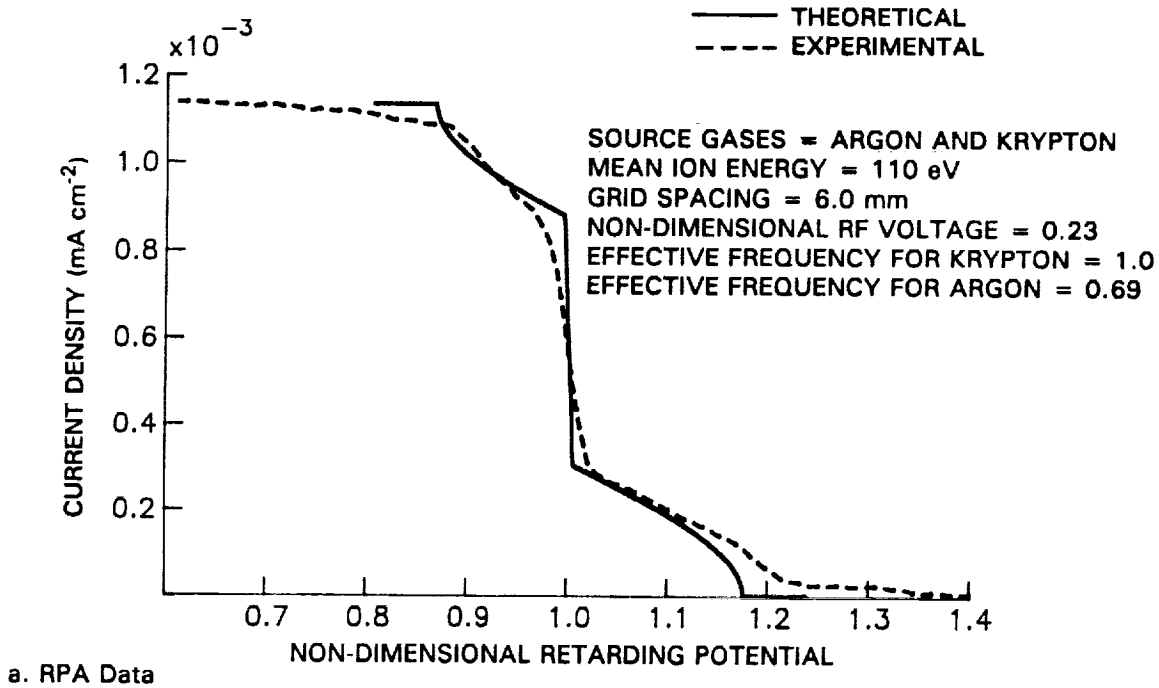

a. RPA Data

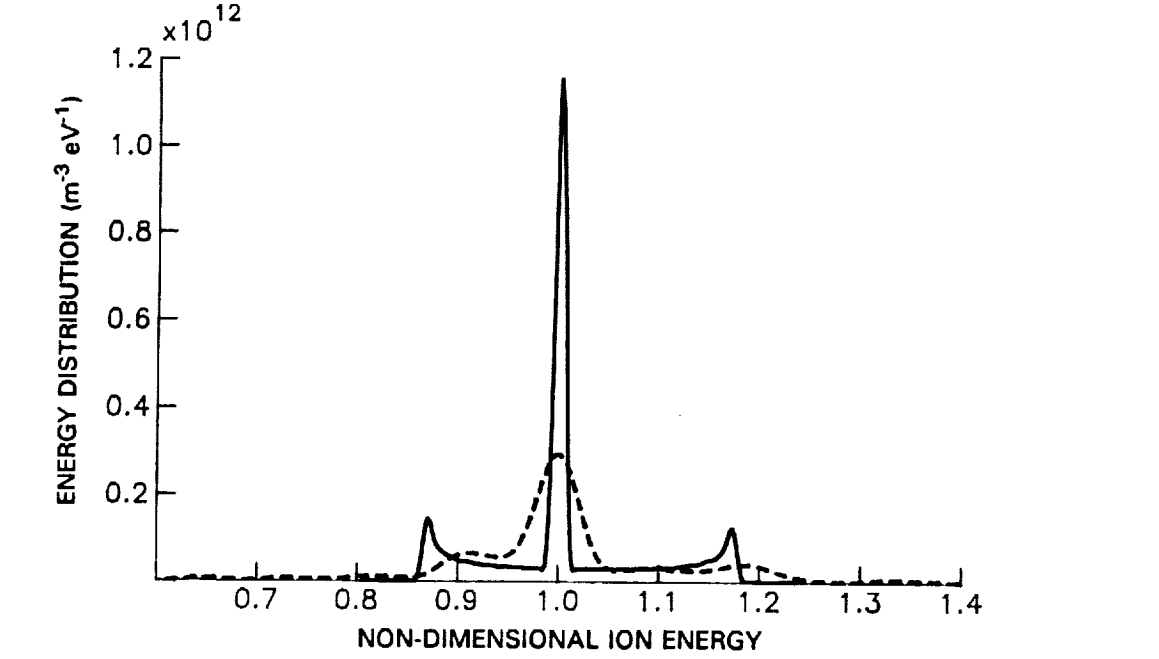

b. Energy Distribution Function

Fig. 7 RPA Trace and Energy Distribution for Krypton-Argon Ion Beam

energy [22]. In order to differentiate the RPA traces, a Fourier series is fit to the data and the Lanczos convergence factor (described in Appendix C) is used to assure convergence of the derivative of the Fourier series.

The theoretical energy distribution function shown in Fig. 7 is characterized by a relatively constant magnitude with two peaks at the ends and a large spike at unity. The spike at unity is due to the krypton ions and the rest of the distribution function represents the argon ion energy distribution. The experimental RPA trace and distribution function shown in Fig. 7 are seen to follow the same trends as the theoretical curve. The spike at unity in the experimental distribution function is wider than the theoretical one. This may be due to a krypton ion energy spread at the entrance to the single-stage Bennett mass spectrometer that is broader than the mono-energetic distribution assumed in the theoretical model. Peaks, although they are not as sharp as those predicted theoretically, are observed at the two ends of the argon ion distribution. It is interesting that both peaks appear at ion energies slightly greater than those predicted theoretically. The reason for this displacement has not been determined; however, this trend is also observed at other RF voltages.

The experimental results of Fig. 7 and other similar data obtained at a variety of grid spacings, ion energies and effective frequencies [23] are considered very important. They suggest that the single-stage Bennett mass spectrometer can indeed be used to discriminate between two ionic species with about a 2-to-1 mass ratio in a moderate current density application. They do not, however, show conclusively that only argon ions are present at energies above unity because the RPA measures current but does not differentiate between the charge carrying species. Demonstration that the two species can be separated will be deferred until the three-grid optics/RF mass discriminator is discussed.

Figure 8 shows time-averaged impingement current data obtained with the

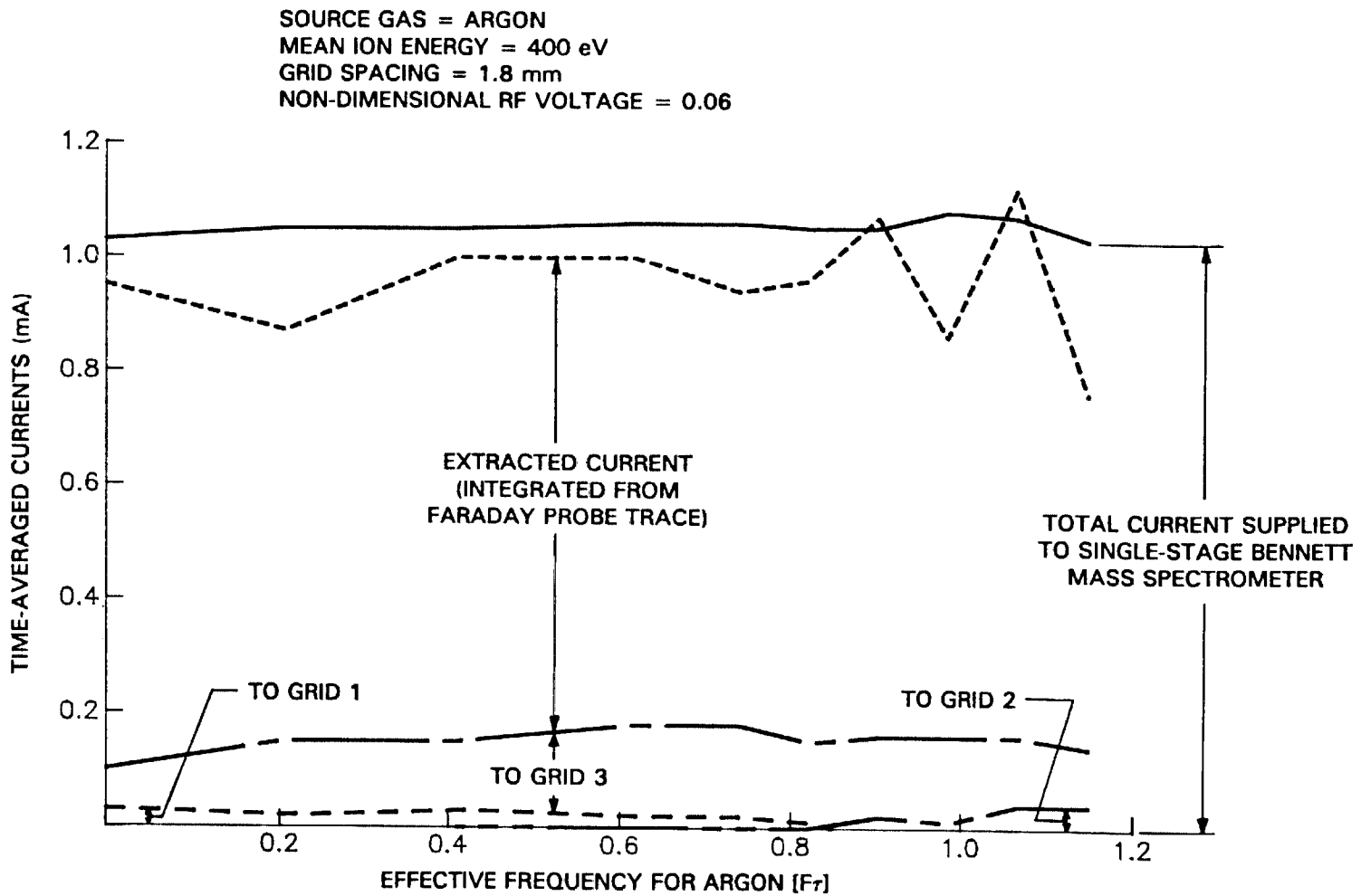

Fig. 8 Current Balance for 1 mA Current to Single-Stage Bennett Mass Spectrometer

19-hole, graphite grid set. Shown are the total current supplied to the single-stage Bennett mass spectrometer by the optics system as well as the currents to each of the grids and the extracted current determined by integrating Faraday probe traces. The sum of the impingement currents and the extracted current should equal the total current supplied to the single-stage Bennett mass spectrometer; generally they agree to within less than 15%. The data in Fig. 8 are obtained while the system is being operated at a condition that results in a minimum total impingement current (i.e. sum of the currents to each of the single-stage Bennett mass spectrometer grids is minimized). Figure 8 shows typical current data obtained with an RF voltage of 0.06 applied over a range of effective frequencies. These data show that the impingement currents going to grids 1 and 2 account for less than 25% of the total impingement current and over 75% of the impingement current goes to grid 3. These data show that impingement currents remain nearly constant over the range of effective frequencies investigated. At the operating conditions of Fig. 8, about 85% of the total current supplied was extracted from the 19-hole grid set which represents an improvement over the 50% extraction rate obtained with the wire mesh covered, single-aperture system.

One concern is whether the extracted current density is in the 0.016 to 1.6 mA/cm^2 range needed to simulate the low-Earth-orbit environment. A spatially-averaged current density can be estimated by dividing the extracted current by the grid area through which current is extracted. The area of a hexagon circumscribing the 19 holes through which the current is being extracted is about 0.85 cm^2 and the extracted current is about 0.85 mA which gives a spatially-averaged current density at the grids of about 1.0 mA/cm^2. This may appear to be in the desired range but there are several loss mechanisms. At typical discharge chamber operating conditions (discharge voltage of 45 V), atomic oxygen will account for about 20% of the beam

ions [14]. Since at least half of the atomic and all of the diatomic ions would be stopped with the filtering grid, over 90% of the beam will be lost. Further, some ions might be lost on divergent trajectories when ions are decelerated by the filtering grid. Loses during the charge-exchange process will further reduce the oxygen atom flux. Therefore, it is desirable to extract more current from the system.

Figure 9 shows time-averaged impingement currents to the grids and the extracted current as well as the total current supplied to the single-stage Bennett mass spectrometer when the current supplied is increased to 3.1 mA. Again the currents are measured as a function of radio frequency with an RF voltage of 0.06 applied. The impingement current to grid 1 of the single-stage Bennett mass spectrometer is negligible. Grid 2 is seen to collect about 15% of the total impingement current while grid 3 collects about 85% of this current. In this case, less than half of the current supplied is extracted from the 19-hole grid set and detected by the Faraday probe. The proportion of current extracted in this case is similar to the fraction extracted from the single-aperture grid set.

It is noteworthy that although the current supplied to the single-stage Bennett mass spectrometer tripled from the conditions in Fig. 8, the amount of current extracted increased by at most 50%. The rest of the current impinged on the downstream grids (i.e. grids 2 and 3). To eliminate the impingement currents to these grids, the system was modified by removing the two downstream grids. The resulting system accomplishes the ion extraction and RF mass discrimination processes in one system called the three-grid optics/RF mass discriminator.

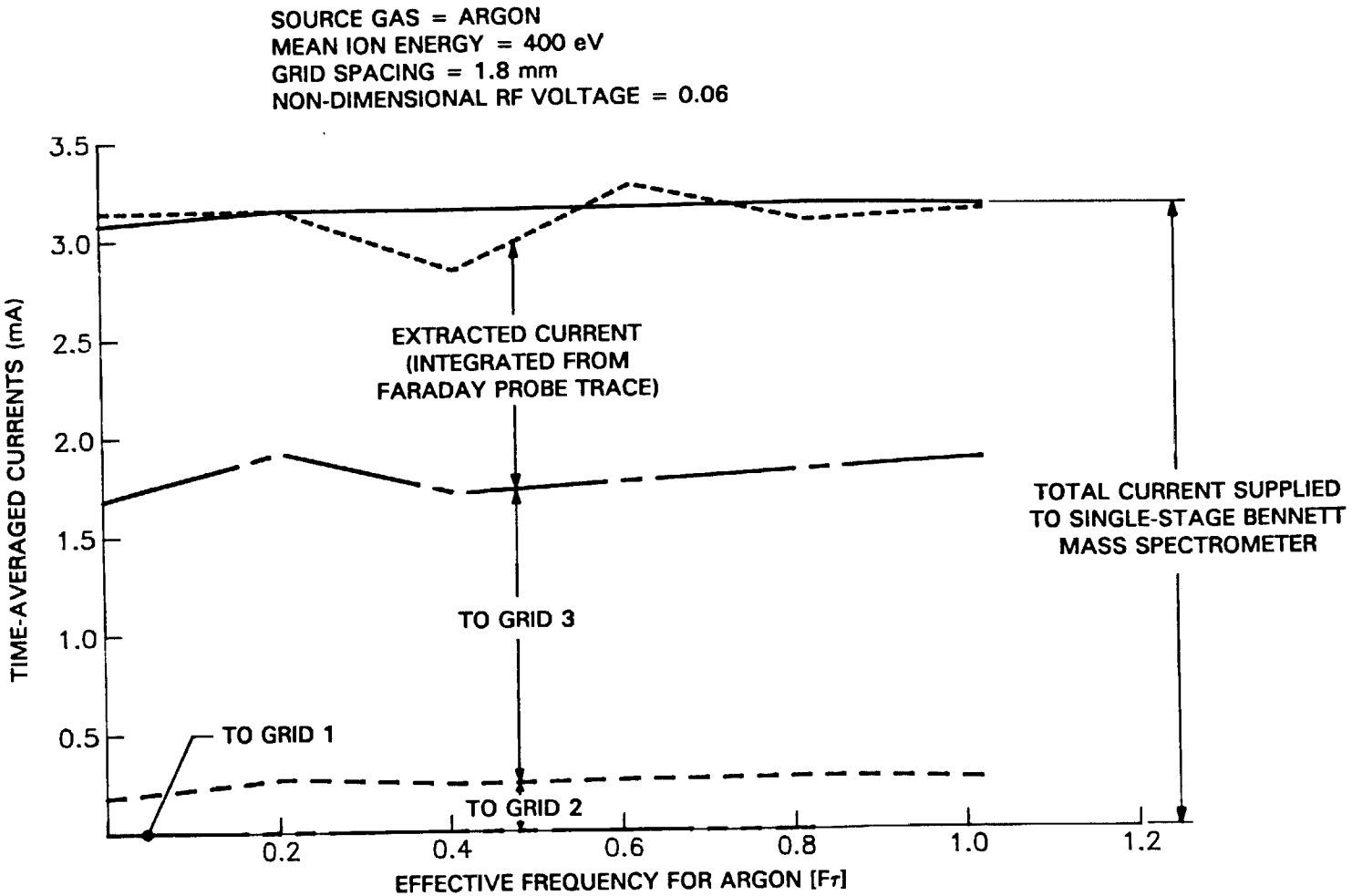

Fig. 9 Current Balance for 3 mA Current to Single-Stage Bennett Mass Spectrometer

IV. THREE-GRID OPTICS/RF MASS DISCRIMINATOR

The preliminary experiments described in the preceding chapter demonstrated that an RF signal could be used to induce a spread in the energies of ions extracted from a broad-beam source. However, to be effective the three-grid optics/RF mass discriminator must not only induce an energy spread, it must also accomplish two additional processes. The system must extract ions from the discharge chamber and the difference in energies induced by the RF signal must be exploited to remove the more massive species from the beam.

Figure 10 shows a schematic of the apparatus used to accomplish these processes. Shown downstream of the discharge chamber is the three-grid optics/RF mass discriminator which will be discussed briefly. The three grids combine the functions of an ion optics system and a single-stage Bennett mass spectrometer. As an optics system component, the screen grid acts to confine the plasma in the discharge chamber. Here it also serves the function of grid 1 of the single-stage Bennett mass spectrometer by providing a boundary which limits the spatial extent of the time-varying electric field. As part of an optics system, the accel grid is biased negative to create an electric field which draws ions from the discharge chamber. The accel grid also serves the function of grid 2 of the single-stage Bennett mass spectrometer by having a sinusoidal RF signal superposed on this mean negative potential. The decel grid serves the function of grid 3 of a single-stage Bennett mass spectrometer by providing a boundary to confine the electric field. In an optics system, the decel grid serves to decelerate but not stop ions. However, in the

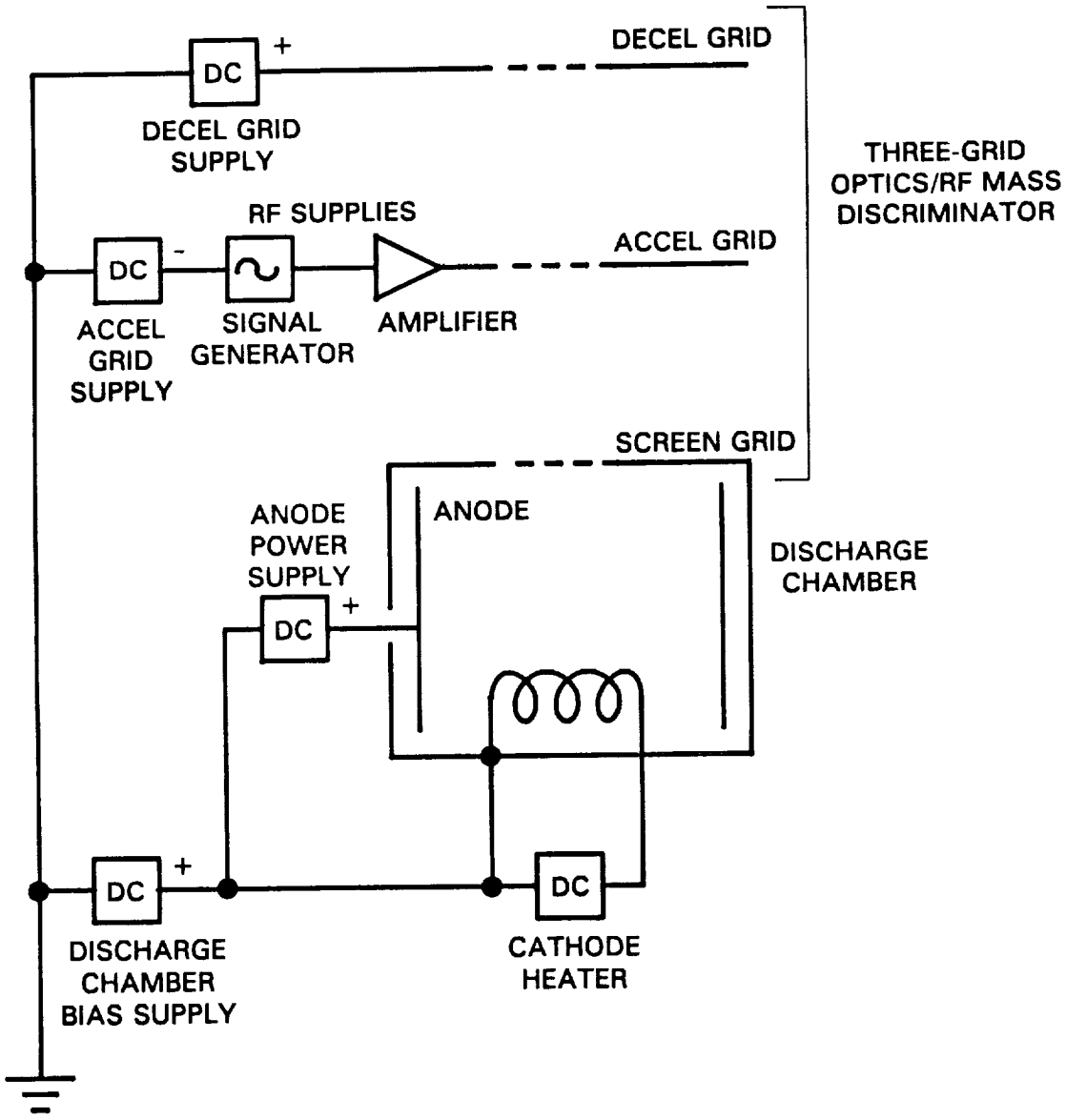

Fig. 10 Experimental Apparatus for Three-Grid Optics/RF Mass Discriminator

three-grid optics/RF mass discriminator, the decel grid is used to stop all of the unwanted ions and it, therefore, serves the function of the filtering grid described previously.

Most of the non-dimensional variables used to describe the single-stage Bennett mass spectrometer operating conditions are also applicable to the three-grid optics/RF mass discriminator. However, non-dimensional kinetic energy, which was an important parameter for the single-stage Bennett mass spectrometer, is not used here. Instead, for the three-grid optics/RF mass discriminator the important non-dimensional parameter is the non-dimensional retarding potential. This is the potential applied to the decel grid to slow or stop ions. The other non-dimensional variables--mass, charge, potential, time, frequency and effective frequency--are all used and defined in the same way as for the single-stage Bennett mass spectrometer.

Experimental Apparatus

Figure 10 shows the experimental apparatus used to study the three-grid optics/RF mass discriminator. The same discharge chamber that was used in the preliminary experiments with the single-stage Bennett mass spectrometer was also used during this testing. In addition, the 0.25 mm thick, 19-hole, graphite grids that were described for the preliminary experiments were used for the three-grid optics/RF mass discriminator. To provide a uniform potential at the decel grid a nickel wire mesh with a transparency of 0.85 and 0.4 mm wire-to-wire spacing was attached to the downstream side of the decel grid. This wire mesh provided a nearly uniform potential plane at the location of the decel grid.

The need for a uniform potential surface at the decel grid can be demonstrated with the following argument. The RF signal applied to the accel grid causes the kinetic energies of some of the less massive ions to be about 5 eV greater than those of the more massive species. The decel grid functions to stop the more massive ions

while slowing the less massive ones to about 5 eV. Because the decel grid surroundings are at lower potentials than the decel grid, the potential at the center of the decel grid hole is also at a lower potential than the grid webbing. Since all of the more massive ions must be stopped, the retarding potential applied to the decel grid must be increased until the potential is high enough to stop the more massive ions at the center of the hole. If the potential varies more than about 5 V between the center of the holes and the decel grid webbing, the potential will be high enough to stop the less massive ions in addition to the more massive ones in the region near the grid webbing. However, with a uniform potential the unwanted species can be stopped while allowing the less massive ions to be extracted over the entire area of the decel hole. Initial experiments suggested that the retarding potential needed to stop ions at the center of the decel hole was up to 50 V higher without the wire mesh than it was with the mesh in place; therefore, the nickel mesh was used during all subsequent experiments. Of course some potential difference between the center of the holes in the wire mesh and the mesh surface still existed. However, because the holes in the mesh were not as large as the decel hole the potential variation was smaller. Experimental results, which follow, demonstrate that the potentials provided by the nickel mesh were adequate to achieve reasonable performance.

In some of the testing it was desirable to use only a single hole to eliminate any effects associated with overlapping beamlets. In those tests all but the center hole of both the screen and decel grids were blocked by attaching a 0.25 mm thick piece of graphite to cover the holes on the downstream face of each of these grids. In other testing, where it was desired to show that diatomic oxygen could be removed in a broad-beam optics system, all 19 holes were used. Although, for the 5 eV atomic oxygen source to provide a beam to a large sample area, it may be necessary to use a system with considerably more holes, the 19-hole grid system is considered to be

adequate to model a broad-beam system. The diagnostic equipment used to study the beams extracted from the three-grid optics/RF mass discriminator included a retarding potential analyzer (RPA) and a Faraday probe. Additionally, an **ExB** probe was used to differentiate between the two species of ions.

The RPA, shown in Fig. 11, was used in a different manner than that described for testing the single-stage Bennett mass spectrometer. Unlike those preliminary tests, the RPA collector was not biased to stop ions; instead, ions were stopped by applying the retarding potential to the decel grid. Therefore, the RPA served to measure total, time-averaged beam current density as a function of the retarding potential applied to the decel grid. As this figure suggests, some of the ions extracted through the decel grid passed through the 2 mm dia aperture and struck a molybdenum collector held at ground potential. As in the preliminary experiments, the current of these ions was determined by measuring the current of electrons through the ammeter required to neutralize them. The Faraday cage was biased sufficiently far below ground potential to stop electrons from passing through the aperture and reaching the collector. Under these conditions no electron currents were observed when the decel grid was biased to high enough potential to stop all the ions.

The Faraday probe shown in Fig. 12 was used to measure time-averaged beam current density profiles. As with the RPA, beam ions passed through the 2 mm dia aperture and impinged on the collector held at ground potential. The Faraday probe was mounted on a structure which allowed it to pivot radially over the grids as suggested by the arc and centerlines in Fig. 12. The current arriving at the collector was measured as a function of angular position using a position sensing potentiometer mounted to the pivot which the probe support structure swung on. The Faraday cage was biased negative to stop electrons from entering the aperture; therefore, current measurement errors due to electron collection were negligible.

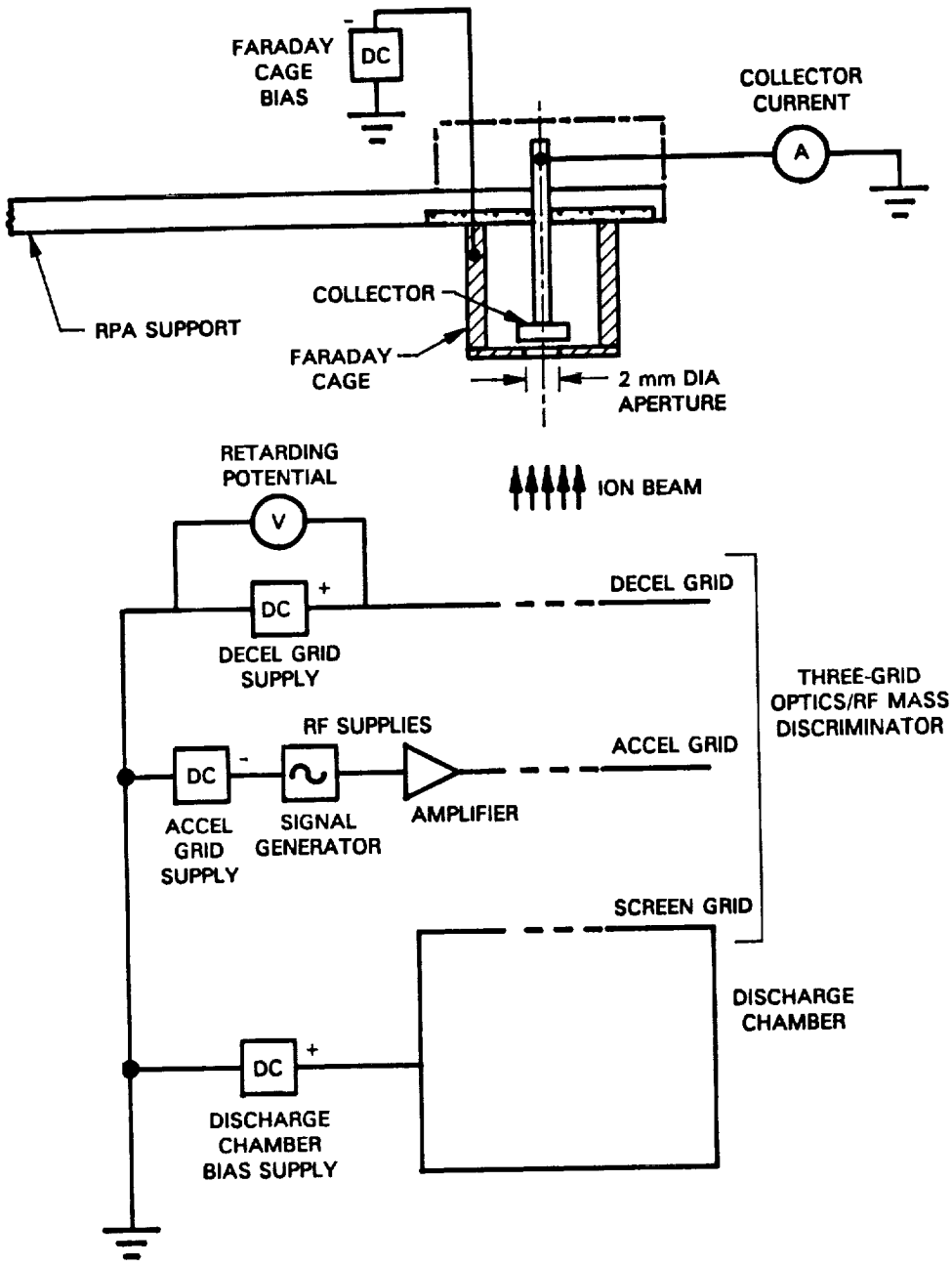

Fig. 11 Retarding Potential Analyzer (for Three-Grid Optics/RF Mass Discriminator)

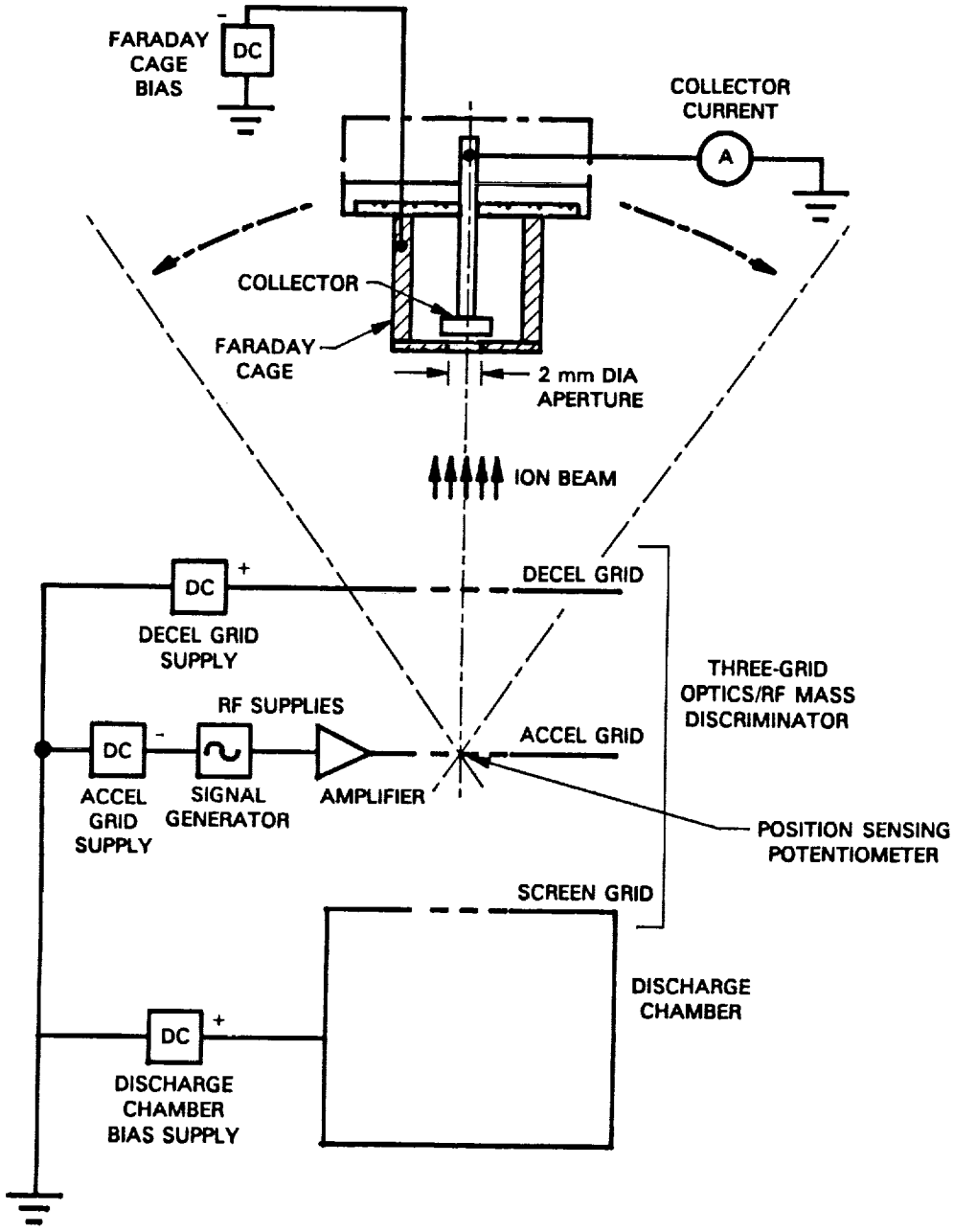

Fig. 12 Faraday Probe (for Three-Grid Optics/RF Mass Discriminator)

The **ExB** probe, shown schematically in Fig. 13, was used to determine the ion composition of the beam extracted from the three-grid optics/RF mass discriminator system. This was accomplished by first collimating a small diameter section of the incident ion beam. This beamlet was then directed into the plate region at normal incidence to both the mutually perpendicular electric (**E**) and magnetic (**B**) fields shown in Fig. 13. The permanent magnet-induced **B** field was fixed but the **E** field could be varied by changing the potential difference between the plates shown. Changes in the **E** field caused the trajectories of the ions to change through the range suggested by the dashed curves. The drift section shown in Fig. 13 increased the velocity resolution of the probe by allowing ions that were deflected only slightly in the **ExB** section to diverge away from the collector. Hence at a given plate potential difference, all ions travelling through the crossed-field region except those within a specific velocity range were deflect away from the collector. Because the probe distinguished on the basis of ion velocity, ions with different masses but nearly the same kinetic energy were sensed at different plate potential differences. By sweeping the plate potential difference, a plot of the current reaching the collector as a function of this difference could be generated; the various species of ions could be identified from such a plot. As with the RPA and Faraday probes, the **ExB** collector was shielded with a Faraday cage (not shown in Fig. 13) which was biased negative to repel stray electrons. More detail on this **ExB** probe can be found in the literature [24].

Experimental Procedure

Single-species testing was conducted using either argon or krypton. This testing was done with the RPA to determine the minimum retarding potential applied to the decel grid required to stop all ions in the beam as a function of RF voltage and effective frequency. During this testing the three-grid optics/RF mass discriminator

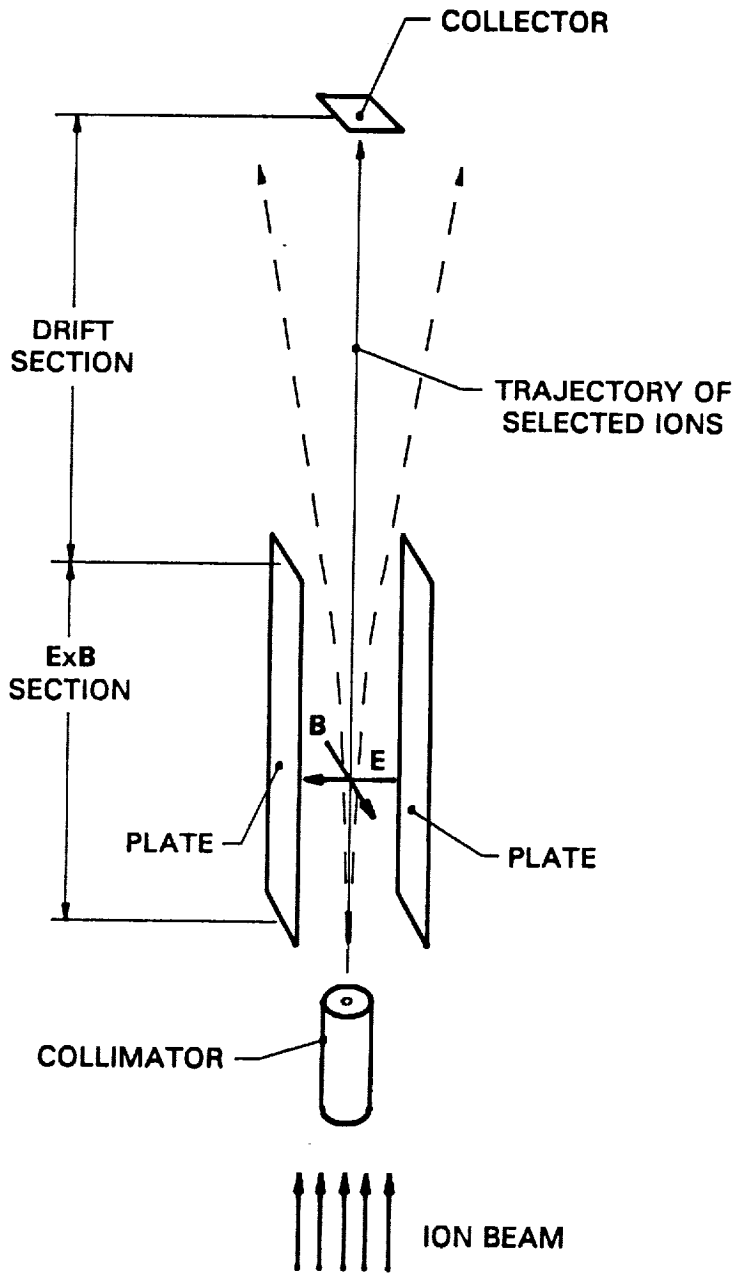

Fig. 13 **ExB** Probe Schematic Diagram

was used in the single-hole configuration and the RPA was aligned coaxially along the grid aperture centerline.

Two-species testing was done using mixtures of argon and krypton to demonstrate that appropriate application of the retarding potential to the decel grid with the system operating at an appropriate frequency, resulted in extraction of one ion species while the other one was filtered out of the beam. This testing was done with the single-hole grid configuration and the **ExB** probe was used to differentiate between two species of ions being extracted from the three-grid optics/RF mass discriminator. During these experiments, ions were typically decelerated to less than 30 eV at the decel grid. At these energies it would have been impossible to differentiate between two species because the difference in their speeds would have been smaller than the **ExB** probe could resolve. In order to obtain speed differences large enough to resolve the two species easily, kinetic energies on the order of a few hundred eV were needed. In order to accelerate the ions into this energy range before they reached the probe, the **ExB** probe was held at ground potential and the discharge chamber was biased to a few hundred volts above ground potential.

Once species separation was demonstrated with argon and krypton, testing was performed using oxygen. Since extraction of atomic oxygen from a broad-beam source was desired, this testing was conducted with current being extracted through all 19 holes of the grid system. The **ExB** probe was used to verify that atomic ions could be extracted while diatomic ions were stopped.

Once demonstration that diatomic oxygen could be removed from the beam while atomic oxygen was being extracted from the three-grid optics/RF mass discriminator, the Faraday probe was used to measure atomic oxygen current density profiles. Testing was conducted using the 19-hole grid system configuration. Due to the configuration of the probe support structure, only one probe could be placed

inside the vacuum system at a time; therefore, the current density measurements were made without determining that atomic oxygen was the only species being extracted. However, the point at which diatomic oxygen was removed from the beam could be estimated from **ExB** probe data. The stopping potentials for both diatomic and atomic oxygen ions were measured with the **ExB** probe. Due to slight variations in operating conditions, these potentials could vary from one experiment to the next; however, the difference between these potentials was observed to be constant. Therefore, experiments that involved current density measurements were conducted by raising the retarding potential to the point where the Faraday probe did not sense any current (i.e. the stopping potential for atomic oxygen ions). Then the potential was decreased by the difference in stopping potentials for diatomic and atomic ions determined from **ExB** probe data. At this condition, where the probe should have sensed only atomic oxygen ions, current density profiles were measured.

Experimental Results (Argon and/or Krypton)

As with the preliminary experiments, experimental results are presented in terms of non-dimensional frequency and potential. Again, dimensional values are listed to enable identification of the actual operating conditions. As with the single-stage Bennett mass spectrometer, the source gas and grid spacing are listed. However, the dimensional values associated with system potentials are different for the three-grid optics/RF mass discriminator. Instead of listing the mean ion energy, the difference between discharge chamber anode potential and the mean potential applied to the decel grid, called the mean-total-accelerating voltage, is used. In addition, the mean potential applied to the accel grid is also listed. Given these dimensional values the actual operating conditions can be determined using the definitions in Appendix A.

As noted above, systematic stopping potential offsets are observed when

experiments are repeated. Variations in discharge chamber plasma potential (the potential at which ions are created) and variations in the RF voltage applied to the accel grid contribute to the observed shifts in stopping potentials. The amplitude of the RF voltage can be measured within ± 2 V. The actual plasma potential is not measured during experiments. However, the discharge chamber plasma potential is usually within a few volts of the potential of the most positive surface in the discharge chamber, which is the anode (Fig. 10). Therefore, it is assumed that the discharge chamber plasma potential is equal to the anode potential. The anode potential can vary from one experiment to the next due to the resolution of the voltmeters used to measure the potentials. The discharge chamber bias supply potential can be measured within ± 3 V and the anode power supply voltage can be measured within ± 1 V. Additionally, variations in discharge currents during different experiments also can cause some variation in discharge chamber plasma potential. It is also noted that the potential applied to the decel grid can be measured within ± 1 V. The systematic stopping potential offsets from different experiments varied as much as 7 V.

One additional note about non-dimensional potentials is given here. For the experimental data presented below, the potential is non-dimensionalized using the mean-total-accelerating voltage which is 500 V. Therefore, in the data presented below, 1 V corresponds to a non-dimensional potential of 0.002.

To determine the retarding potential required to stop all ions during single species testing, RPA traces like the one in Fig. 14 were obtained. Two traces, obtained at typical operating conditions, are shown; one (solid line) is obtained at an effective frequency of zero (no RF signal applied) and the other (dashed line) is obtained with an RF voltage of 0.08 and an effective frequency for argon of 0.5. Two phenomenon cause the observed shape of these traces; beam focusing varies as the decel potential varies (i.e. the current directed toward the RPA depends on the

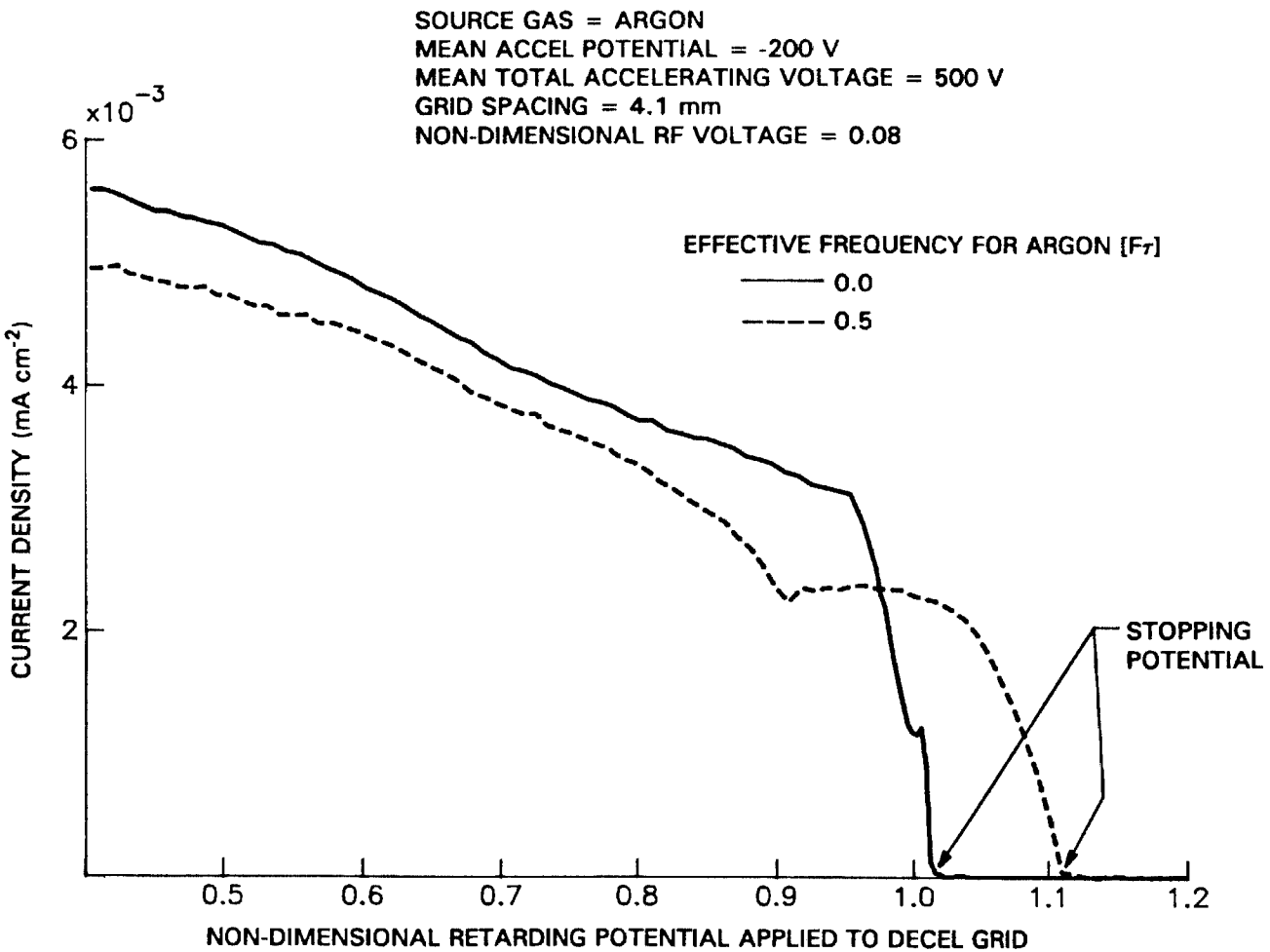

Fig. 14 Typical RPA Data

electric field in the grid system and the field changes as the decel potential changes) and at high enough decel potentials the current decreases because ions are being stopped. The minimum retarding potential required to stop all ions is the potential at which the collector current goes to zero. This potential is called the stopping potential and is identified for each of the RPA traces. When the effective frequency is zero the stopping potential is 1.01. For the case where the RF signal is applied, the stopping potential is substantially greater (about 1.11), indicating that a significant energy spread can be induced with the three-grid optics/RF mass discriminator.

As noted, at the zero effective-frequency (no RF signal applied), the stopping potential is slightly greater than unity. Theoretically these ions would be stopped at a retarding potential of unity because the ions have negligible kinetic energy when they are produced in the discharge chamber plasma which is assumed to be at a potential of unity. Three possibilities, which have been previously discussed, could contribute to this shift. The potential applied to the decel grid may have to be slightly higher than unity to stop ions from passing through the center of the holes in the nickel wire mesh attached to the decel grid. It is also possible that the potential of the discharge chamber plasma is slightly different than the anode potential which is used in computing the stopping potential. In addition, systematic errors in reading potentials due to volt meter resolution could also contribute to this shift. Regardless of the reason for the shift, it is noted that in general, the stopping potential measured during experiments is between 1 to 5% higher than the theoretical predictions.

The stopping potential for a given species can be calculated using the first-order model derived in Appendix A. The first-order solution for the stopping potential is

$$\nu_s = 1 + \nu_{RF}\Phi(F\tau) \quad . \tag{3}$$

where Φ, the stopping potential parameter, is a function of effective frequency ($F\tau$). The equation for Φ is given in Appendix A. Figure 15 shows a comparison of theoretically and experimentally obtained stopping potentials for RF voltages of 0.04, 0.06 and 0.08 at effective frequencies for argon ranging from 0 to about 1.4. The solid curves are the theoretical values for stopping potential and they are seen to increase from unity as the effective frequency increases from 0 to about 0.5 where they go through a maximum. The traces then decrease to a relatively constant value at an effective frequency of about 1.2. The experimental traces exhibit the same trend; however, the whole trace is shifted to a slightly higher potential. Aside from the shift, the experimental maxima appear to be somewhat broader and to be shifted to a slightly higher effective frequency than predicted theoretically. Nevertheless, the theoretical and experimental results correlate fairly well.

Similar data were obtained for krypton at similar operating conditions and some of them are shown in Fig. 16. Here the stopping potentials shifted to even higher values than were observed with argon. Slight variations in power supply settings and changes in discharge chamber operating conditions caused by switching form argon to krypton could easily have caused the observed shift. Aside from the shift to higher energies, the comparison of experimental and theoretical results for krypton is similar to that obtained with argon.

The single species testing is useful because it gives a guide to the frequency and retarding potential ranges over which separation of the two species might be achieved. This information is shown in the direct comparison of the stopping potential data for argon and krypton made in Fig. 17 for the 0.06 RF voltage data from Figs. 15 and 16. A few words about the comparison are in order. First it is

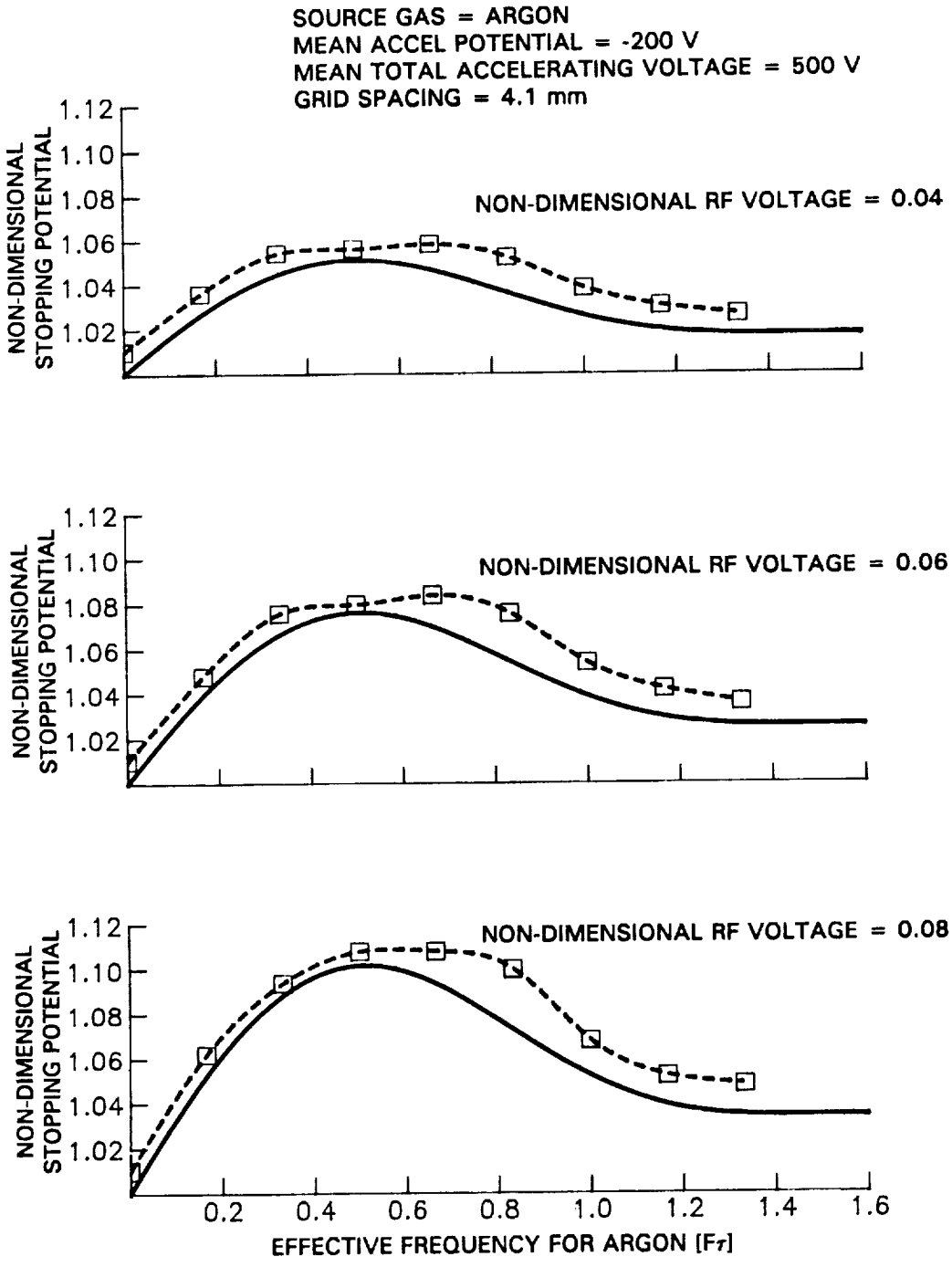

Fig. 15 Comparison of Theoretical and Experimental Stopping Potentials for Argon

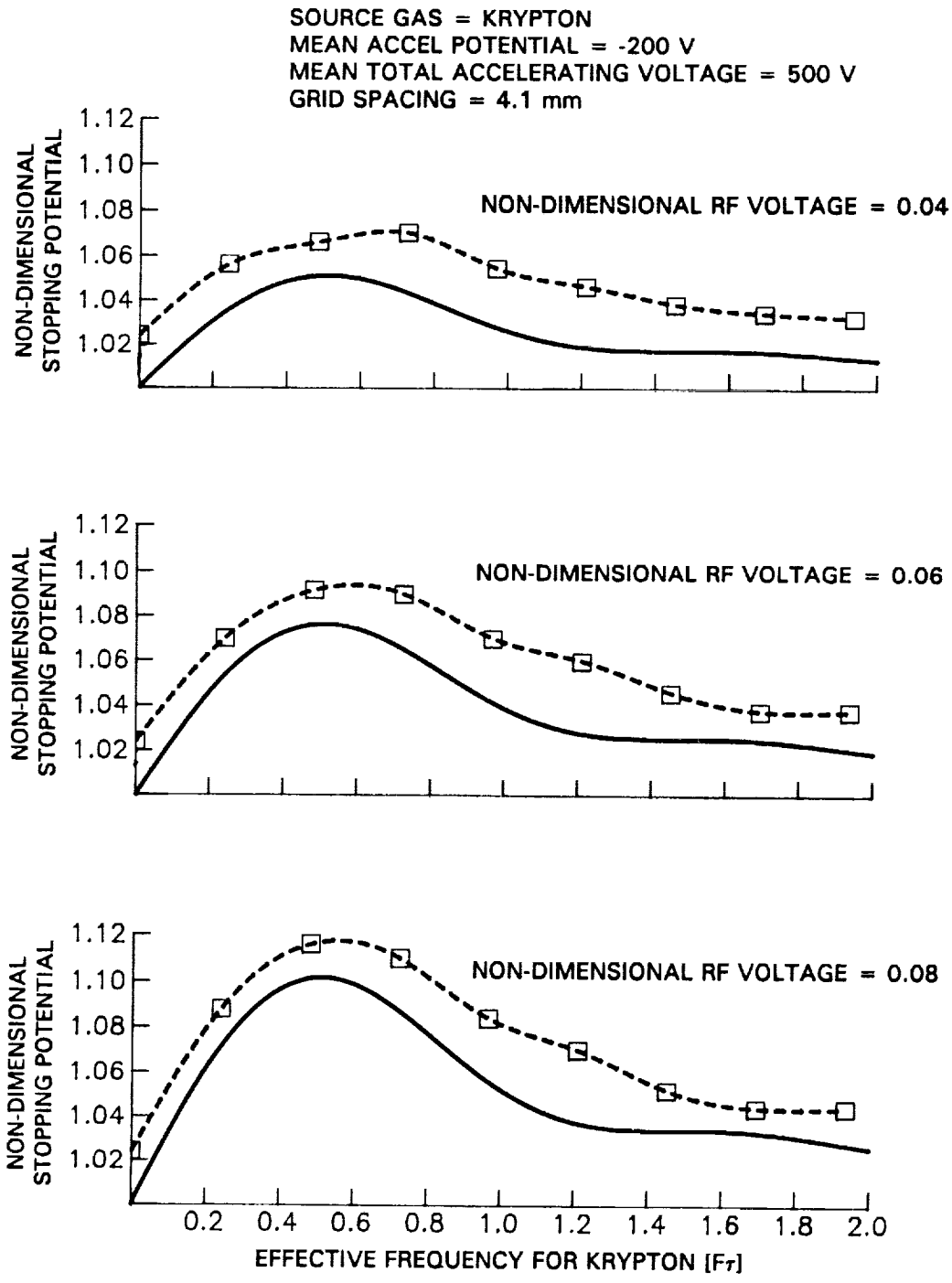

Fig. 16 Comparison of Theoretical and Experimental Stopping Potentials for Krypton

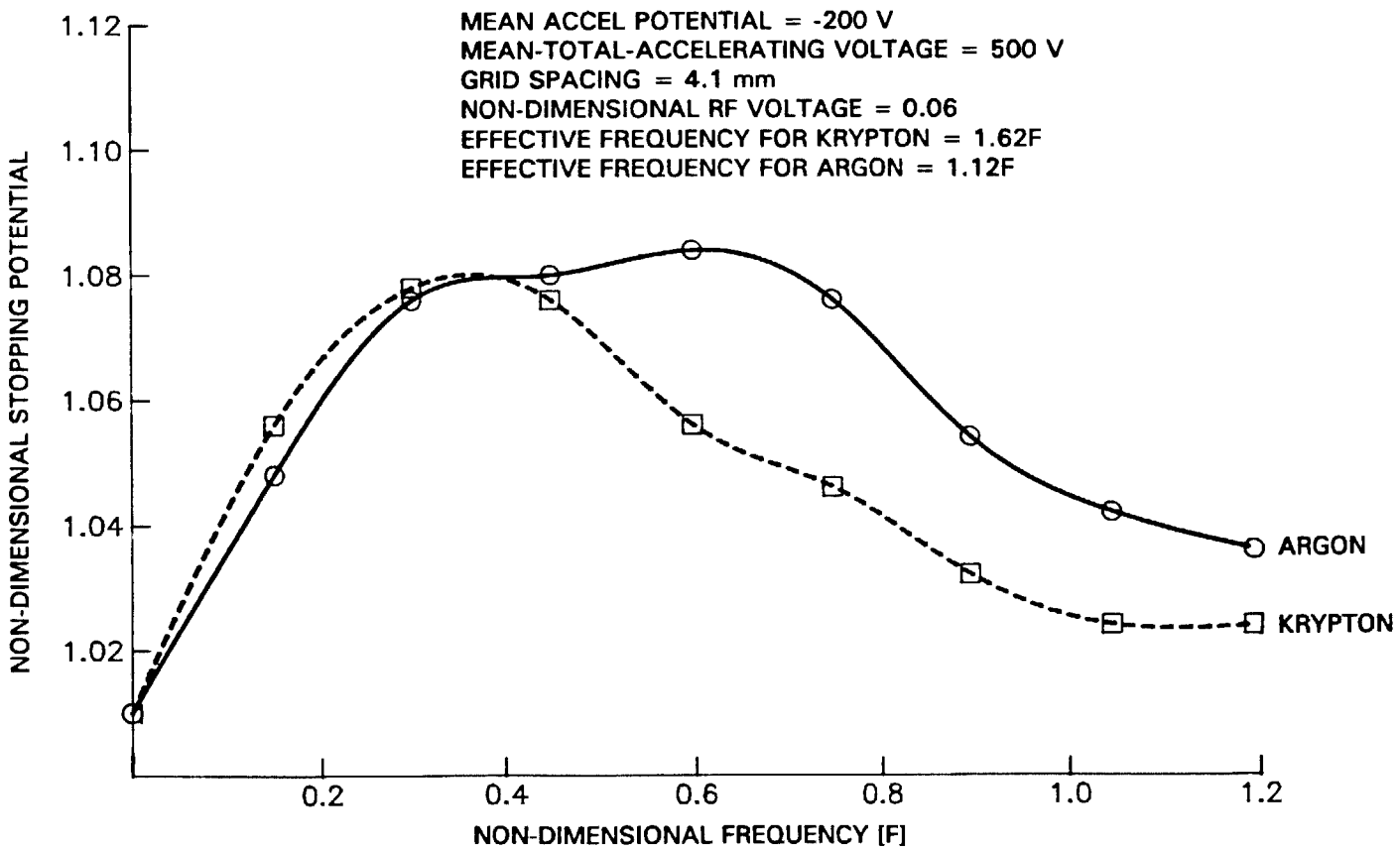

Fig. 17 Comparison of Stopping Potentials for Krypton and Argon

noted that frequency and not effective frequency is used in this comparison. Recall that frequency is held fixed during system operation. Since ions travel at different speeds due to their mass difference each species has a different effective frequency resulting in different stopping potentials at a given operating condition. By examining the stopping potentials for each species, the frequency range over which one species can be stopped while the other is extracted can be determined. Second, comparing the data of Figs. 15 and 16 a systematic shift in the krypton and argon stopping potential data is observed. However, if both species are simultaneously produced and extracted from the discharge chamber plasma, the stopping potential should be the same for both species at a frequency of zero (corresponds to steady-state operation). Therefore, to compare these data the krypton curve is shifted so that the argon and krypton stopping potentials match at zero. When the argon curve lies above (below) the krypton curve, argon (krypton) can be extracted from the three-grid optics/RF mass discriminator. These curves suggests that it is possible to extract krypton at frequencies between 0 and about 0.4 and that argon can be extracted at frequencies greater than 0.4.

To verify this, two species testing was conducted using argon and krypton mixtures. Figure 17 suggests that the difference in stopping potentials for krypton and argon is greatest (about 0.028) near a frequency of 0.6. Figure 18 shows **ExB** probe traces taken at this frequency and an RF voltage of 0.06. The top trace is obtained with a retarding potential of 1.060 applied to the decel grid and the krypton and argon peaks are clearly evident. When the retarding potential is increased to 1.070, the middle trace of Fig. 18 is obtained. It is evident that most of the krypton has been removed from the beam while a significant portion of the argon is still being extracted. At a retarding potential of 1.074, all the krypton is stopped while argon is still being extracted as seen in the bottom trace of Fig. 18. Figure 19 shows **ExB**

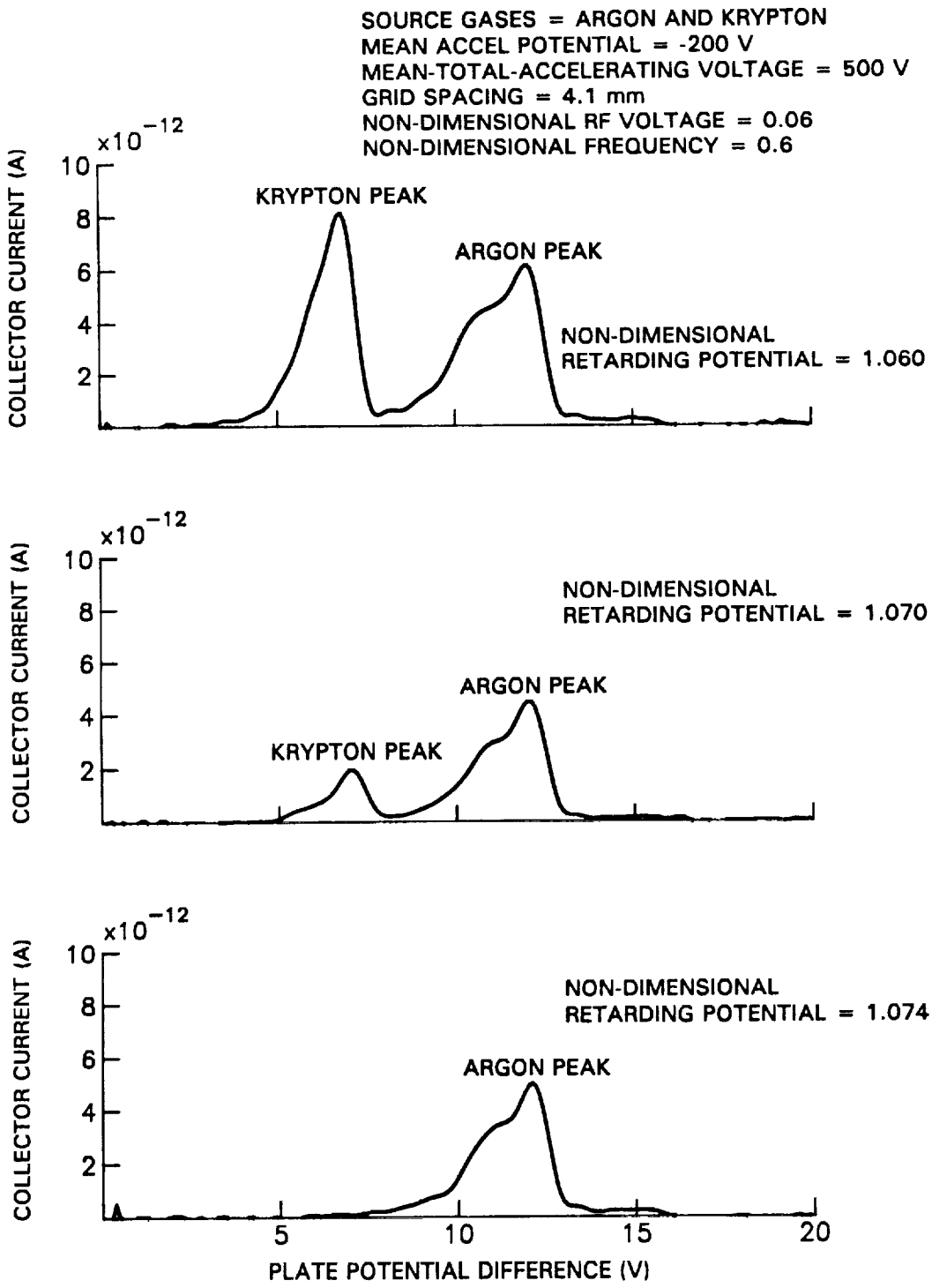

Fig. 18 ExB Data Demonstrating Krypton Filtering for Krypton-Argon Ion Beam

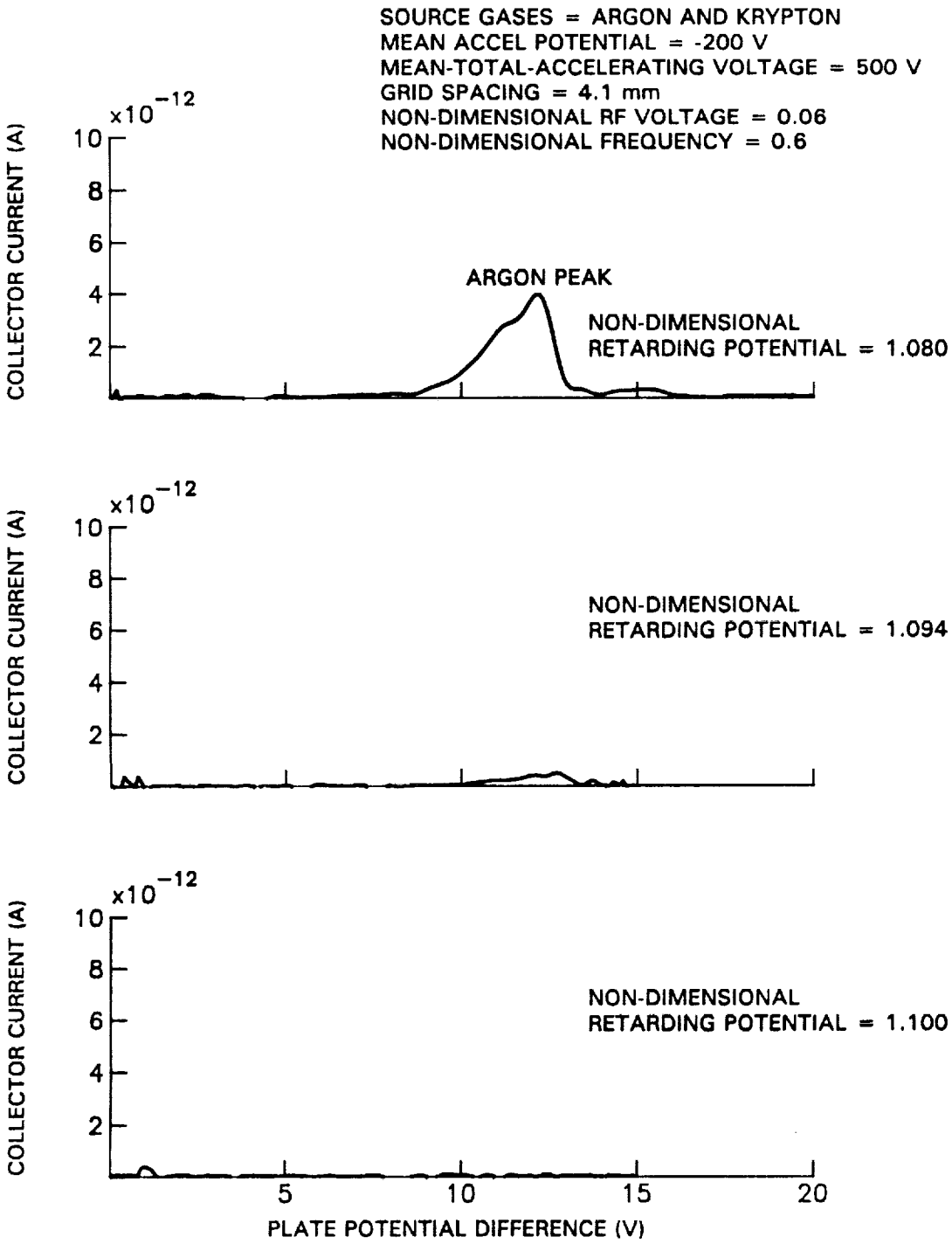

Fig. 19 ExB Data for Argon After Krypton is Stopped

probe traces obtained as the retarding potentials are increased to 1.080, 1.094 and 1.100 (top, middle and bottom traces, respectively). Comparing the bottom trace in Fig. 18 with the top trace in Fig. 19, it is seen that the amount of argon being extracted decreases slightly as the retarding potential changes from 1.074 to 1.080. At 1.094 the argon peak has almost disappeared and at 1.100 there is no trace of argon. These data show that the difference in the stopping potential for krypton and argon is greater than 0.02 but less than 0.03, in agreement with the single species data[5].

Although the goal of this study is to demonstrate extraction of the less massive species while stopping the more massive one, it is interesting to note that Fig. 17 suggests that it should be possible to extract krypton while stopping argon at frequencies between 0 and about 0.4. Figure 20 shows **ExB** probe traces taken at a frequency of 0.3. The top trace in Fig. 20 is obtained at a retarding potential of 1.080; at this condition, the krypton peak is evident and the argon peak is small indicating that most of the argon ions are being stopped. At a retarding potential of 1.090 the argon peak has disappeared and krypton, albeit less than at a retarding potential of 1.080, is still being extracted as seen in the middle trace of Fig. 20. When the retarding potential increases to 1.100, the krypton peak also disappears as seen in the bottom trace of Fig. 20. Because this particular test was not considered essential, finer resolution of the retarding potentials required to stop each species was not obtained. Nonetheless, these data show that the range of retarding potentials over which argon in stopped but krypton is still being extracted is smaller than 0.02, which is in agreement with the data of Fig. 17.

---

[5] At the particular operating conditions of Figs. 18 and 19, 0.02 to 0.03 amounts to argon ions being slowed to kinetic energies between 10 and 15 eV at the decel grid when it is biased to the stopping potential for krypton.

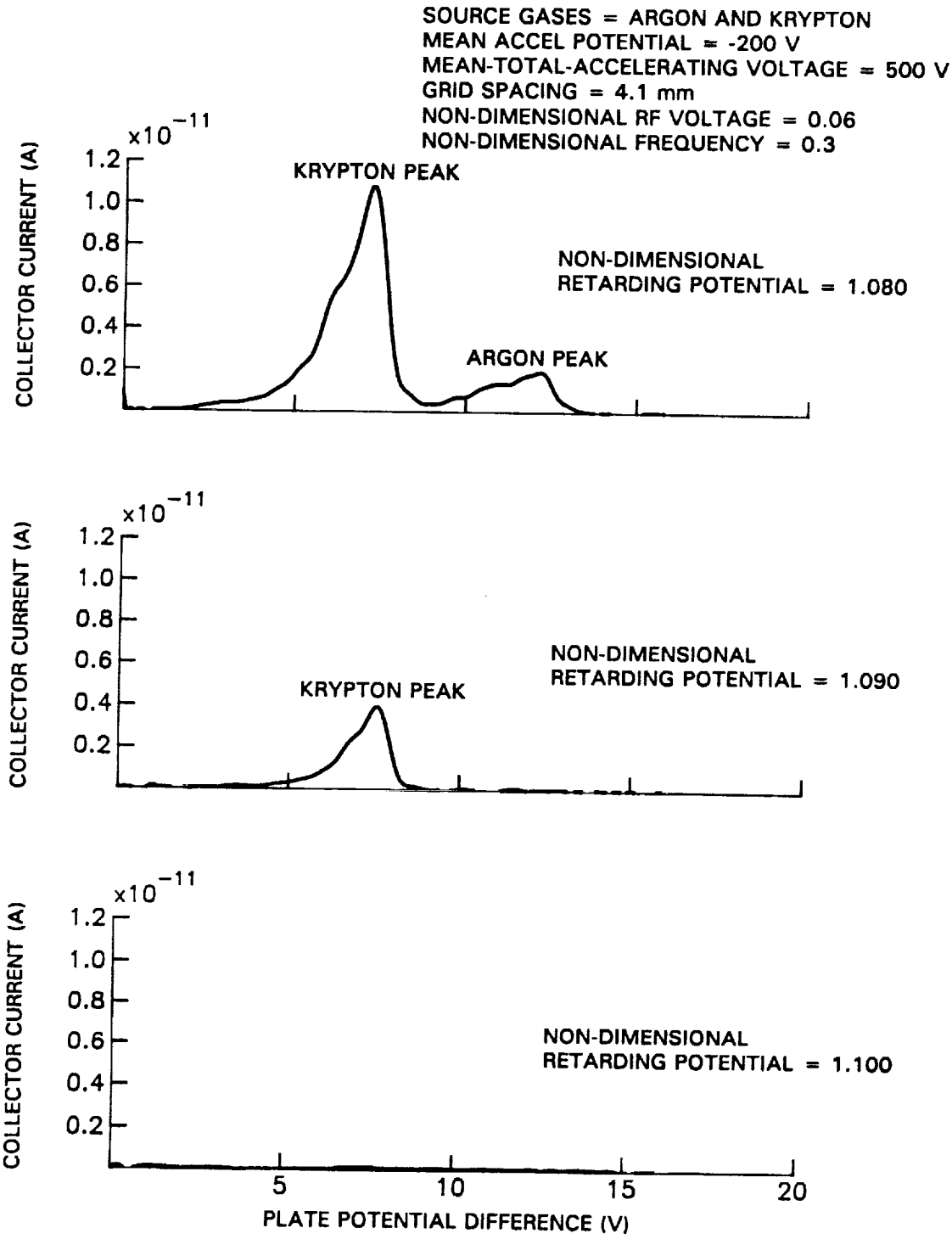

Fig. 20 **ExB** Data Demonstrating Argon Filtering for Krypton-Argon Ion Beam

Experimental Results (Oxygen)

Since testing with argon and krypton verified that the more massive species can be removed while the less massive species is being extracted, testing was conducted to demonstrate that separation of atomic and diatomic oxygen can also be achieved using the three-grid optics/RF mass discriminator. To obtain a guide for the range of frequencies over which atomic oxygen ions can be separated from diatomic oxygen ions, theoretical curves of stopping potential v. frequency were generated for both species. Figure 21 shows the theoretical curves at an RF voltage of 0.06 which suggest that diatomic oxygen can be stopped at a lower potential than atomic oxygen for frequencies greater than 0.6. The curves suggest that, for the given RF voltage, the largest difference is about 0.02 and that this difference should be observed at frequencies between about 0.75 and 1.2.

Figure 22 shows **ExB** traces obtained with the RF discriminator operating at a frequency of 1.2 at various retarding potentials. The top trace is obtained with a retarding potential of 1.040 applied to the decel grid and both the atomic and diatomic oxygen peaks are evident. When the retarding potential is increased to 1.050, most of the diatomic oxygen is stopped while most of the atomic oxygen is still being extracted as shown in the middle trace of Fig. 22. When the retarding potential is increased further to 1.056 the diatomic oxygen is completely removed from the beam and the trace at the bottom of Fig. 22 is obtained. Another trace (not shown) indicates that all the atomic ions are stopped when the retarding potential is raised to 1.070. Considering the actual dimensional conditions at which these oxygen data are collected, it is evident that the difference between the stopping potential for diatomic and atomic oxygen is about 7 V. This demonstrates that the three-grid optics/RF mass discriminator can be used to extract an atomic oxygen beam with ions being decelerated to near 5 eV kinetic energy at the decel grid.

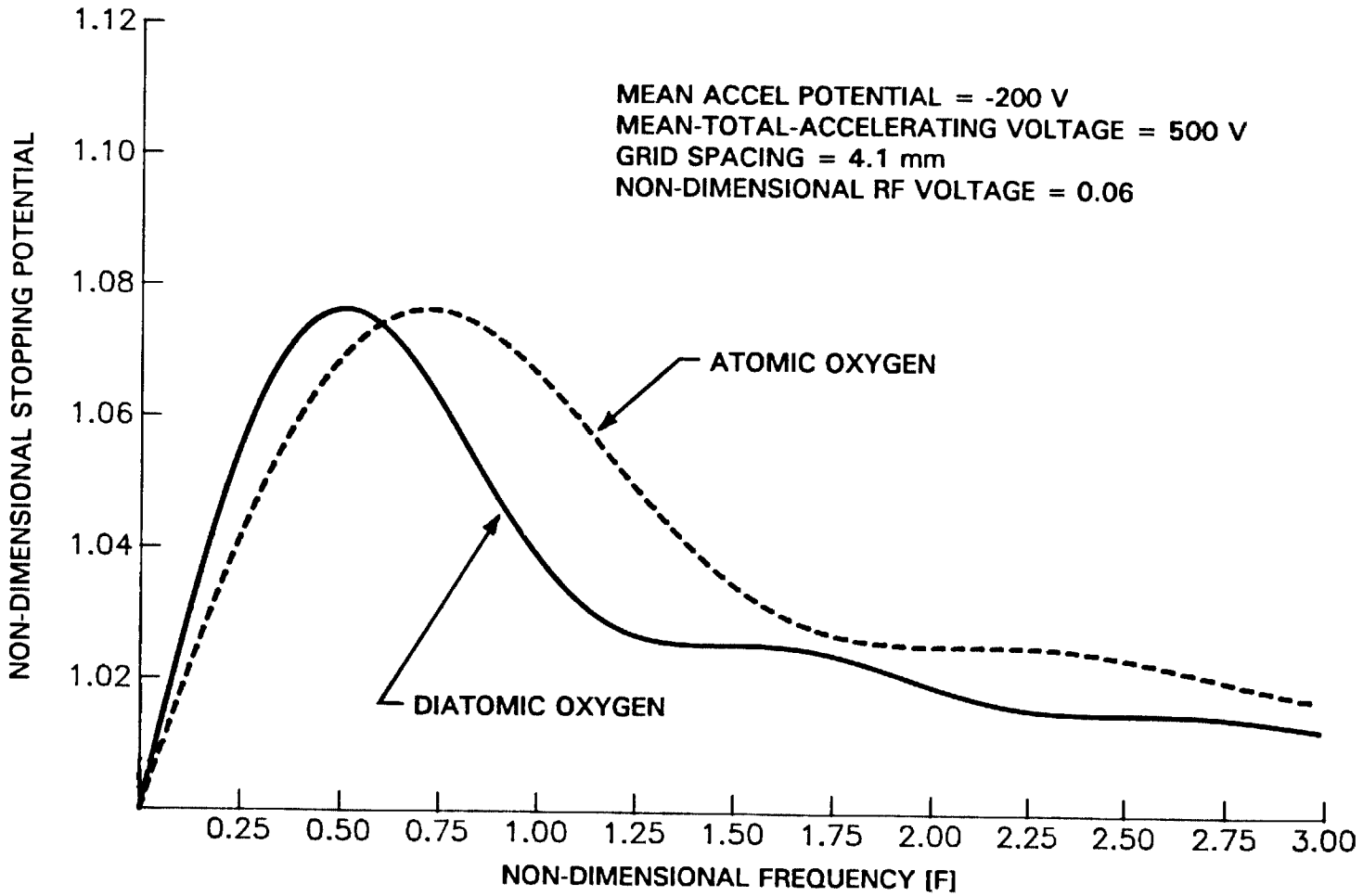

Fig. 21 Theoretical Stopping Potentials for Atomic and Diatomic Oxygen

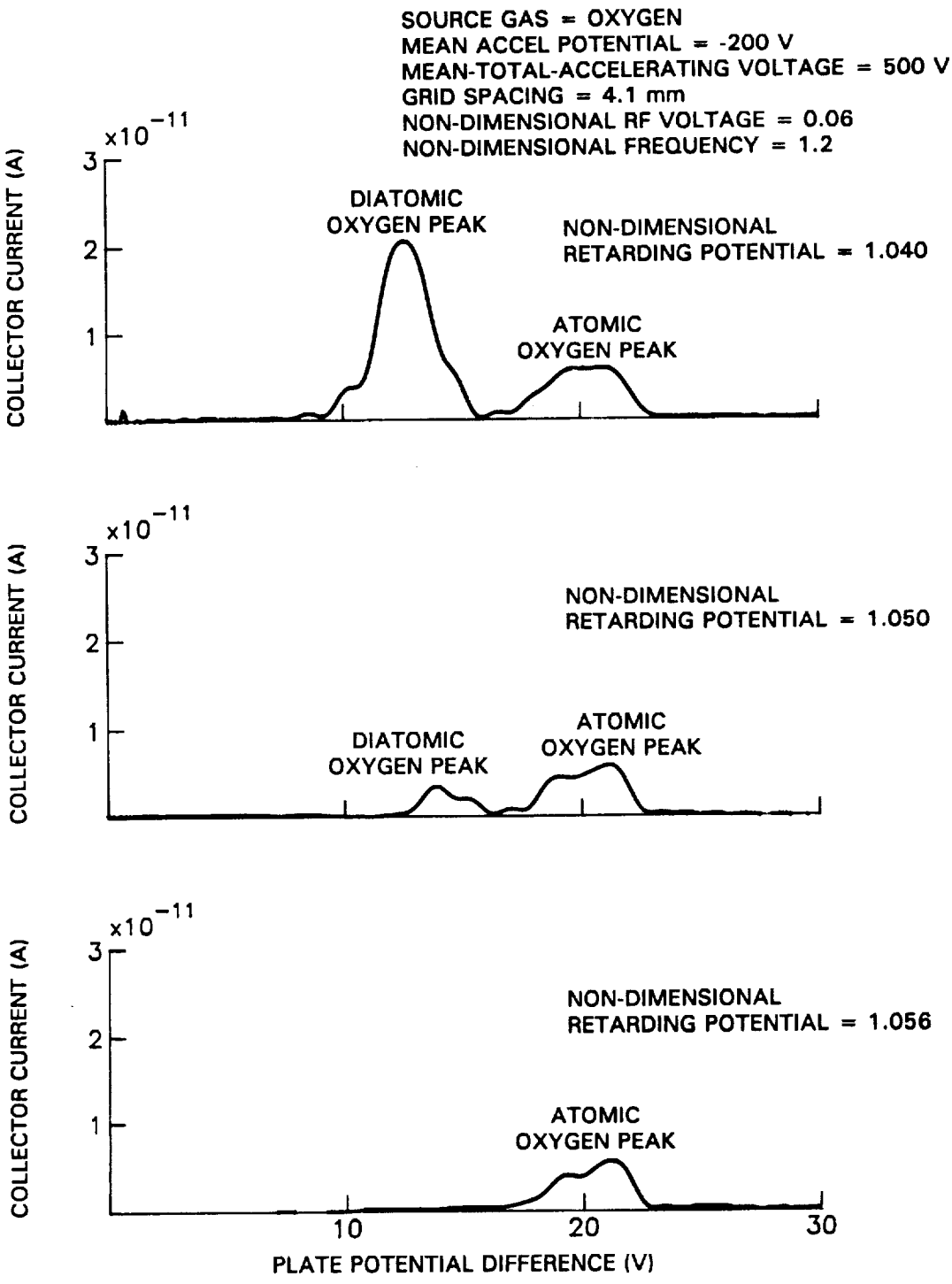

Fig. 22 ExB Data Demonstrating Filtering of Diatomic Oxygen

Since demonstration that atomic oxygen with about 5 eV kinetic energy can be extracted from the three-grid optics/RF mass discriminator, testing to determine the atomic oxygen current density was conducted. Figure 23 shows a typical Faraday probe trace obtained with the 19-hole grid system configuration. Shown is the current density measured on an arc 4.5 cm downstream of the decel grid. This trace is obtained at operating conditions that maximize the current density at an angle of 0°. Although it is possible to extract more current from the system, the beam becomes more divergent and, therefore, the current density decreases. The current density is largest at an angle of about -10° because the probe passes near the center of a grid hole at this angular location. At 0° the probe passes near the edge of a hole and at about 10° the probe passed near the webbing between grid holes. The current density in the central portion of the beam varies between 2.5×10^{-4} to 4.5×10^{-4} mA/cm^2 and the mean value is about 3×10^{-4} mA/cm^2. This is 0.3% of the current density needed to simulate the low-Earth-orbit environment (0.1 mAeq/cm^2). However, by decreasing the grid spacing and increasing the radio frequency (as discussed in the Future Work section) it might be possible to obtain current densities on the order of 0.1 mA/cm^2.

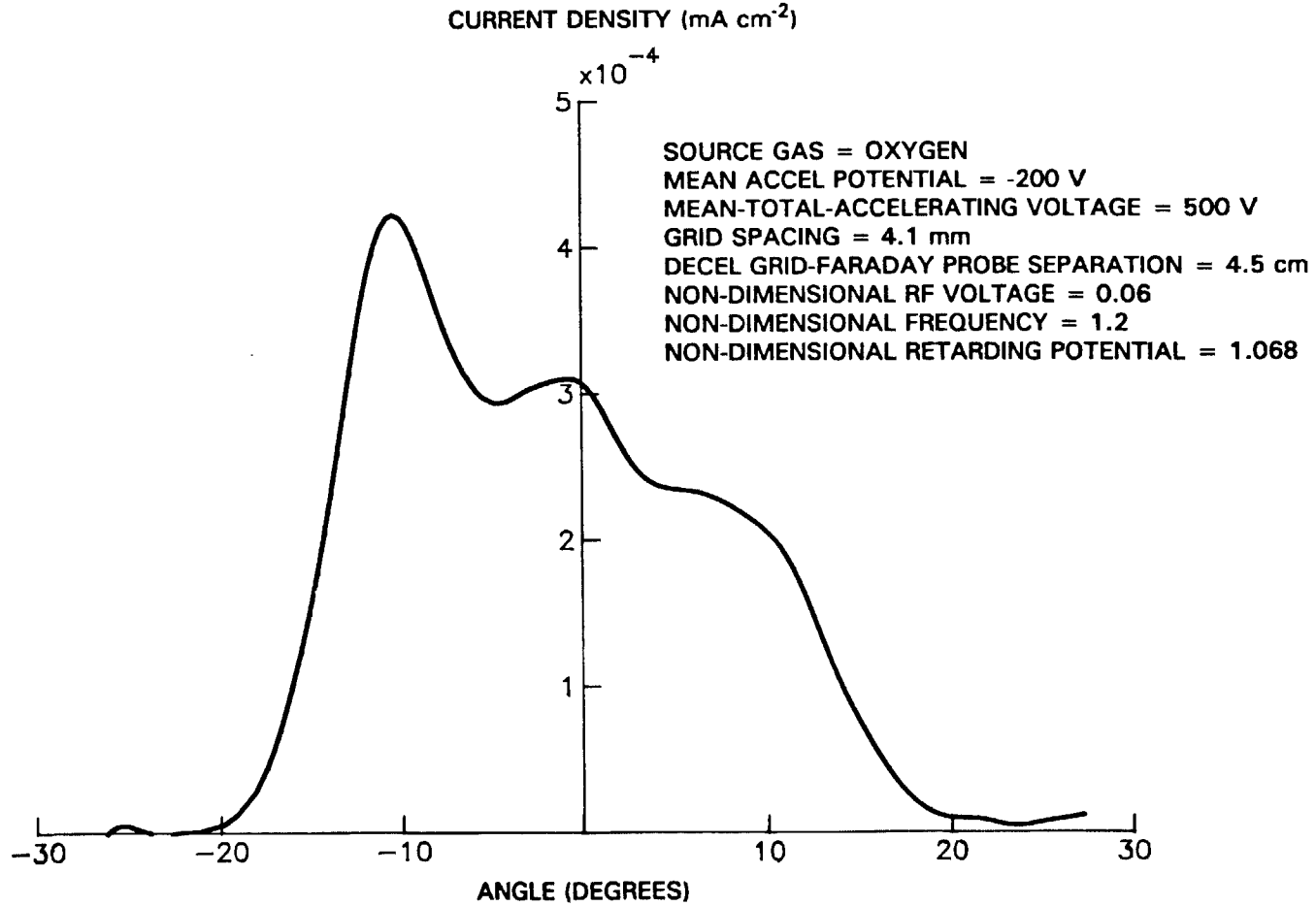

Fig. 23 Atomic Oxygen Current Density Data for 19-Hole Grid System

V. CONCLUSIONS

Discrimination of ions having about a 2-to-1 mass ratio in a three-grid optics/RF mass discriminator based on a modified single-stage Bennett mass spectrometer has been demonstrated. To gain an understanding of how mass discrimination is accomplished, physical insight into the intra-grid acceleration process was sought through a simple first-order, one-dimensional model. Application of this model to a single-stage Bennett mass spectrometer suggests that if the frequency of the applied RF voltage is selected so that ions of one species experiences two full RF cycles while travelling through the system, they will emerge with the same kinetic energy that they had when they entered the spectrometer. Due to the difference in mass, ions of the other species travel at a different speed and do not experience an integer number of cycles while travelling through the single-stage Bennett mass spectrometer. As a result, they have a significant spread induced in their energies when they emerge from the system. Ion energies measured during preliminary experiments conducted with the single-stage Bennett mass spectrometer show good agreement with these theoretical predictions.

The simple model can also be used to predict the stopping potential for a given species in the three-grid optics/RF mass discriminator. Examination of the model shows that the stopping potential is different for different species of ions at a given frequency. This suggests that it should be possible to stop all ion of one species while still extracting ions of the other species. Further investigation suggests that below a certain frequency the more massive species can be extracted and above this frequency the less massive species can be extracted. Experiments conducted using

mixtures of argon and krypton ions demonstrate that either krypton or argon can be extracted from the three-grid optics/RF mass discriminator, while the other species is stopped, in the frequency ranges predicted by theory.

Experiments demonstrating that the three-grid optics/RF mass discriminator can be used in a 5 eV atomic oxygen source were also conducted. Using the model predictions as a guide in choosing system operating conditions, experiments showed that the three-grid optics/RF mass discriminator can be used to filter out diatomic oxygen ions while extracting an atomic oxygen ion beam with kinetic energies near 5 eV. Extraction of these atomic oxygen ions has been demonstrated using a 19-hole grid system representative of a broad-beam ion source. Although higher current densities of atomic oxygen than those demonstrated during experiments are desired to simulate the low-Earth-orbit environment, it is anticipated that the desired current densities can be achieved by scaling down the system dimensions and increasing the frequency of the applied RF signal to values suggested by the simple model.

VI. FUTURE WORK

The work presented in this dissertation demonstrates that the three-grid optics/RF mass discriminator can separate diatomic and atomic oxygen ions and produce a beam of atomic oxygen ions with about 5 eV kinetic energy. However, if a 5 eV atomic oxygen source is to be constructed, two additional concerns must be addressed. First a system which charge neutralizes the atomic oxygen ions must be incorporated into the system and secondly the atomic oxygen current density should be increased to low-Earth-orbit flux levels.

Figure 24 shows a system configuration incorporating a charge neutralization system along with the three-grid optics/RF mass discriminator which could be used to produce a 5 eV atomic oxygen beam. Shown is the screen grid attached to one end of the discharge chamber within which atomic and diatomic oxygen ions are produced. The accel grid has a sinusoidal RF voltage superposed on a negative mean potential applied to it. The decel grid serves two functions; it stops the diatomic oxygen ions and also charge neutralizes ions that impinge on the glancing incidence charge-exchange surface. An array of charge-exchange surfaces might be arranged on the decel grid as shown in Fig. 24. Since about half of the atomic oxygen ions are not charge neutralized, an electric field--set up between a pair of metal deflection plates located downstream of the decel grid--is used to deflect atomic oxygen ions out of the oxygen atom beam. Hence, all the functions required to deliver the low energy atomic oxygen are accomplished within a very compact grid system located immediately adjacent to the ion source. Because the atomic oxygen does not travel long distances between the ion source and the target, this system should minimize

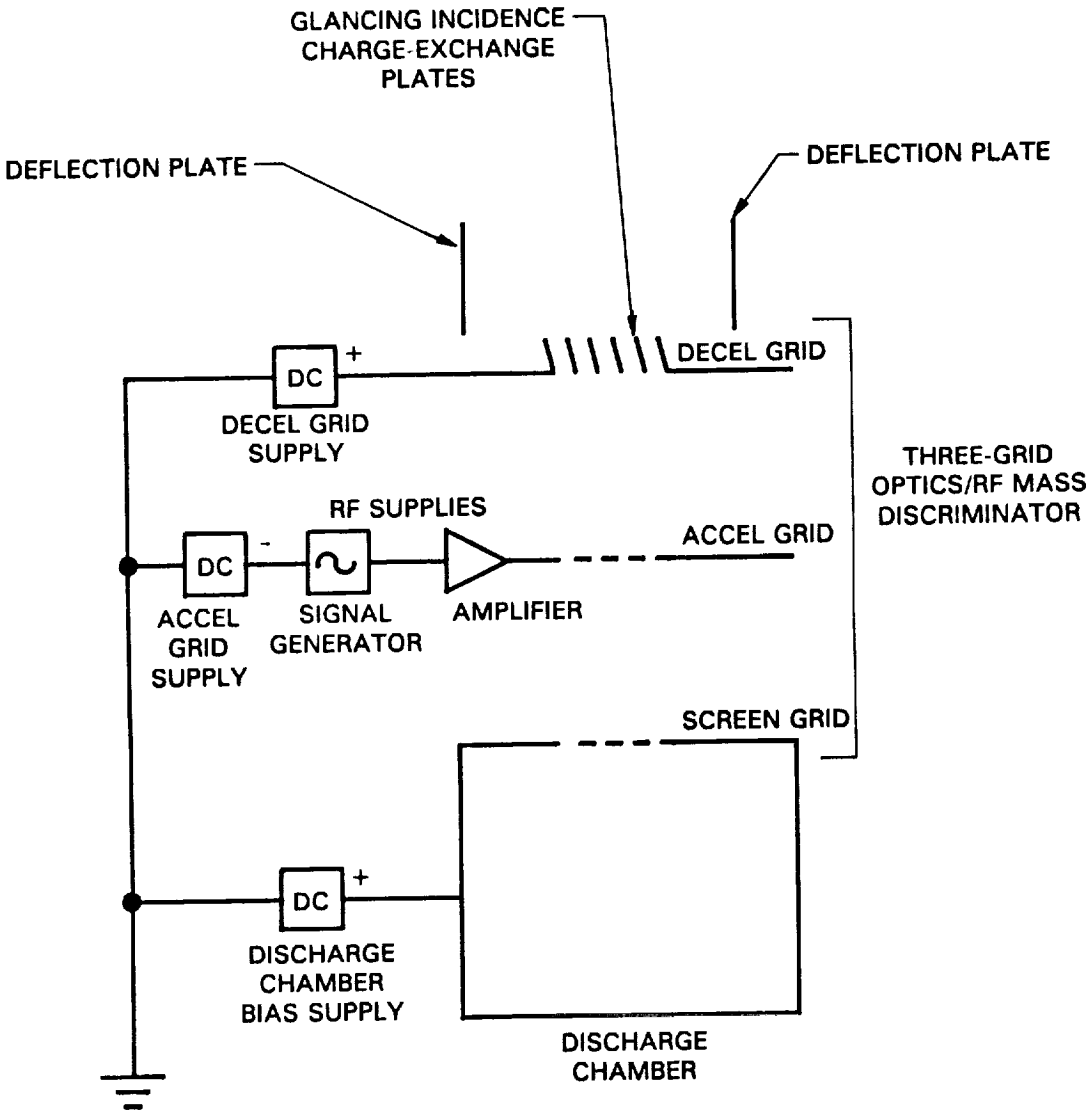

Fig. 24 Envisioned Configuration for a 5 eV Atomic Oxygen Source

loses of atoms on divergent trajectories.

Increasing the atomic oxygen flux could be accomplished by increasing the fraction of atomic oxygen ions produced in the discharge chamber and by scaling the dimensions of the grid system to increase the current density obtained from the discharge chamber. A microwave discharge can be used to increase the fraction of atomic oxygen over that produced in an arc discharge [25] with atomic oxygen ion fractions as high as 0.85 having been reported. A more than 4-fold increase in atomic oxygen current density should be obtained from such a source. (Recall that the atomic oxygen ion fraction was about 0.2 in the arc discharge used during the experiments reported in this dissertation.) Since only about half of these ions would be charge neutralized, the atomic oxygen flux downstream of the glancing incidence plate would be about double that shown in Fig. 23 (about $6x10^{-4}$ mAeq/cm^2).

In order to obtain fluxes of 0.1 mAeq/cm^2, needed to simulate the low-Earth-orbit environment, the grid system must be scaled. The atomic oxygen current density extracted at the decel grid is proportional to the current density extracted from the discharge chamber. The current density drawn from the discharge chamber depends on the electric field between the screen and accel grids. In turn, the electric field depends on the grid spacing and the mean-total-accelerating voltage (i.e. the difference between the discharge chamber plasma potential and the mean potential applied to the accel grid). The RF voltage is a small perturbation, typically less than 0.1 times the mean-total-accelerating voltage, and it therefore should not significantly affect the current density being extracted from the discharge chamber. Thus, scaling laws which are applicable to systems operated at steady-state conditions also should be applicable for this system. For a system operated at steady-state operating conditions, it is known that keeping the hole-diameter-to-grid-spacing ratio and the

total-accelerating voltage constant while reducing the size of the grid system will result in increase current density [26]. Specifically, the current density increases as the inverse square of the grid spacing. Thus, to obtain current densities on the order of 0.1 mA/cm^2, the grid spacings must be reduced from 4.1 mm, used while obtaining the data of Fig. 23, to 0.3 mm and the hole diameter must be decreased from 2 mm dia to 0.15 mm dia. Ion optics systems have been operated at grid spacings as small as 0.22 mm with the total-accelerating voltages as high as 900 V [27]. Therefore, it is feasible to scale the system to 0.3 mm grid spacings while operating at a 500 V mean-total-accelerating voltage (used while obtaining the current density data shown in Fig. 23).

In addition to scaling the grid system dimensions, the frequency of the RF signal applied to the accel grid also must be scaled. The frequency scales as the inverse of the grid spacing. The oxygen data presented in this dissertation were obtained at a frequency of 8 MHz. Scaling the grid spacing down to 0.3 mm requires that the frequency be increased to about 110 MHz. The RF amplifier, used during the experiments reported above, has a bandwidth of 15 MHz and , therefore, it could not be operated at 110 MHz. Because of this equipment limitation, experiments could not be conducted on a scaled-down system.

REFERENCES

1. Leger, L. J. and Visentine, J. T., "Protecting Spacecraft from Atomic Oxygen", Aerospace America, July 1986, pp. 32-35.

2. Zimcik, D. G. and Maag, C. R., "Results of Apparent Atomic Oxygen Reactions with Spacecraft Materials During Shuttle Flight STS-41G", J. of Spacecraft and Rockets, V. 25, March-April 1988, pp. 162-168.

3. Vaughn, J. A., Linton, R. C., Carruth, M. R., Jr., Whitaker, A. F., Cuthbertson, J. W., Langer, W. D., and Motley, R. W., "Characterization of a 5-eV Neutral Atomic Oxygen Beam Facility", Fourth Annual Workshop on Space Operations Applications and Research (SOAR '90), Albuquerque, New Mexico, June 26-28, 1990, NASA Conference Publication 3101, Vol. II, R. T. Savely, ed., pp. 764-771.

4. Banks, B. A., Rutledge, S. K., Paulsen, P. E., Steuber, T. J., "Simulation of the Low Earth Orbital Atomic Oxygen Interaction With Materials by Means of an Oxygen Ion Beam", NASA TM-101971, Feb. 1989.

5. Vaughn, J. A., NASA Marshall Space Flight Center, Private Communication, Feb. 1992.

6. Cole, R. K., Albridge, R. G., Dean D. J., Harlund, R. F., Jr, Johnson, C. L., Pois, H., Savundararaj, P. M., Tolk, N. H., Ye, J., Daech, A. F., "Atomic Oxygen Simulation and Analysis", Acta Astronautica, Vol. 15, No. 11, 1987, pp. 887-891.

7. A. A. Lucas, "Self-image excitation mechanism for fast ions scattered by metal surfaces at grazing incidence", Physical Review B, Vol. 20, No. 12, 15 December 1979, pp. 4990-5001.

8. Cuthbertson, J. W., Langer, W. D., Motley, R. W., Vaughn, J. A.,"Atomic Oxygen Beam Source for Erosion Simulation", Fourth Annual Workshop on Space Operations Applications and Research (SOAR '90), Albuquerque, New Mexico, June 26-28, 1990, NASA Conference Publication 3103, Vol. II, R. T. Savely, ed., pp. 734-741.

9. Holmes, A. J. T., The Physics and Technology of Ion Sources, John Wiley and Sons, New York, 1989, I. G. Brown, ed., pp. 66-69.

10. Enge, H. A., Focusing of Charged Particles, Academic Press, New York, 1967, A. Septier, ed., Vol. II, pp. 203-264.

11. Wilson, R. G., Brewer, G. R., Ion Beams With Applications to Ion Implantation, John Wiley and Sons, New York, 1973, pp. 431-444.

12. Bennett, W. H., "Radiofrequency Mass Discriminator," J. Appl. Phys., V. 21, February 1950, pp. 143-149.

13. Aston, G. and Kaufman, H. R., "Ion Beam Divergence Characteristics of Three-Grid Accelerator Systems", AIAA Journal, Vol. 17, No. 1, January 1979, pp. 64-70.

14. Rapp D., Englander-Golden P., and Briglia D. D., "Cross Sections for Dissociative Ionization of Molecules by Electron Impact", The Journal of Chemical Physics, Volume 42, Number 12, 15 June 1965, pp. 4081-4084.

15. Kaufman H. R., and Reader, P. D., "Experimental Performance of Ion Rockets Employing Electron-Bombardment Ion Sources", presented at the ARS Electrostatic Propulsion Conference, U. S. Naval Postgraduate School, Monterey, California, November 3-4, 1960.

16. Reader, P. D., "Investigation of a 10-Centimeter-Diameter Electron-Bombardment Ion Rocket", NASA Tech. Note TN D-1163, Jan. 1962.

17. Reader, P. D., "Experimental Effects of Scaling on the Performance of Ion Rockets Employing Electron-Bombardment Ion Sources", presented at the National IAS-ARS Joint Meeting, Los Angeles, California, June 13-16, 1961.

18. Kaufman, H. R., "An Ion Rocket with an Electron-Bombardment Ion Source", NASA Tech. Note TN-585, Jan. 1961.

19. Wilbur, P. J. and Han, J. Z., "Constrained-Sheath Optics for High Thrust-Density, Low Specific-Impulse Ion Thrusters," AIAA Paper No. 87-1073, May 1987.

20. Chen, F. F., Introduction to Plasma Physics and Controlled Fusion, Plenum Press, New York, 1984, pp. 8-11.

21. Rapp, D., Englander-Golden, P. "Total Cross Sections for Ionization and Attachment in Gases by Electron Impact",The Journal of Chemical Physics, Volume 43, Number 5, 1 September 1965, pp. 1464-1479.

22. Friedly, V. J., "Hollow Cathode Operation at High Discharge Currents", NASA CR-185238, April 1990, pp. 83-87.

23. Anderson, J. R., Wilbur, P. J., Carruth, M. R., Jr., "An Ion Optics System Incorporating Radio Frequency Mass Separation", AIAA Paper No. 90-2567, July 1990.

24. Vahrenkamp, R. P., "Measurements of Double Charged Ions in the Beam of a 30-cm Mercury Bombardment Thruster",AIAA Paper No. 73-1057, October 1973.

25. Sakudo, N., The Physics and Technology of Ion Sources, John Wiley and Sons, New York, 1989, I. G. Brown, ed., p. 240.

26. Jahn, R. G., Physics of Electric Propulsion, McGraw-Hill Book Company, New York, 1968, pp. 164-165.

27. Rovang, D. C., "Ion Extraction Capabilities of Two-Grid Accelerator Systems", NASA CR-174621, Feb. 1984, p. 90.

28. Press, W. H., Flannery, B. P., Teukolsky, S. A., Vetterling, W. T., Numerical Recipes The Art of Scientific Computing (FORTRAN Version), Cambridge University Press, Cambridge, 1989, pp. 147-151.

29. Press, W. H., Flannery, B. P., Teukolsky, S. A., Vetterling, W. T., Numerical Recipes The Art of Scientific Computing (FORTRAN Version), Cambridge University Press, Cambridge, 1989, pp. 498-515.

30. Lanczos, C., Applied Analysis, Prentice-Hall, Englewood Cliffs, New Jersey, 1964, pp. 219-221.

31. Haberman, R., Elementary Applied Partial Differential Equations, 2nd Edition, Prentice-Hall, Englewood Cliffs, New Jersey, 1987, pp. 75-78.

32. Press, W. H., Flannery, B. P., Teukolsky, S. A., Vetterling, W. T., Numerical Recipes The Art of Scientific Computing (FORTRAN Version), Cambridge University Press, Cambridge, 1989, pp. 401-407.

33. Press, W. H., Flannery, B. P., Teukolsky, S. A., Vetterling, W. T., Numerical Recipes The Art of Scientific Computing (FORTRAN Version), Cambridge University Press, Cambridge, 1989, pp. 386-387.

APPENDIX A

A One-Dimensional Model of the Intra-Grid Acceleration Process

The important parameters for both the single-stage Bennett mass spectrometer and the three-grid optics/RF mass discriminator are the terminal ion energy and the stopping potential, respectively. In order to predict the values of these parameters, a simple one-dimensional model of the intra-grid acceleration process for both systems has been developed. Since the model does not account for three-dimensional effects, such as ion divergence due to radial electric fields, it can be used only as a guide to predict general trends. Therefore, other effects which are even less significant are also neglected.

The magnitude of the magnetic fields set up by the discharge chamber electromagnet were typically less than $5x10^{-3}$ Tesla during experiments; therefore, magnetic effects are neglected. At typical operating conditions background pressures and temperatures in the bell jar were in the 10^{-5} to 10^{-4} Torr range and about 300 K, respectively. In addition, the entire grid system extended less than 10 cm in all experiments; therefore, it is assumed that the ions have no collisions as they pass through the grid system. In order to minimize the divergence of the extracted ion beam, the system was operated at less than 20% of the space-charge limited current density; therefore, space-charge effects are also neglected.

As previously mentioned, the model uses only one spatial variable (x) in addition to the temporal one (t). Because of this and the fact that the grid thickness is much less than the intra-grid spacing, the grids are modelled as evenly-spaced, equipotential planes. Figure A1 shows the planar geometry and boundary conditions

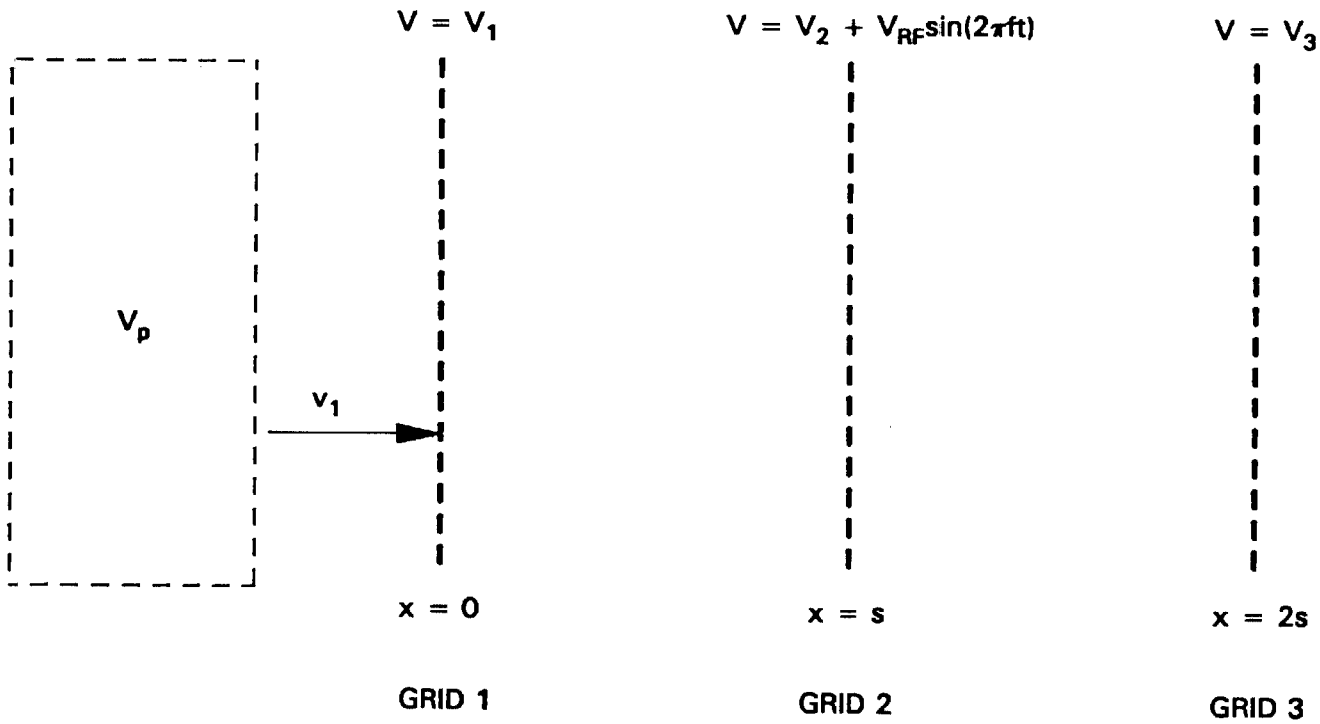

Fig. A1 Geometry and Boundary Conditions for the Single-Stage Bennett Mass Spectrometer and the Three-Grid Optics/RF Mass Discriminator

associated with both the single-stage Bennett mass spectrometer and the three-grid optics/RF mass discriminator. The two systems differ because of the boundary conditions imposed on each. For both systems, ions are generated and have negligible kinetic energy in a discharge chamber plasma which is at potential V_p. Ions extracted from the plasma approach grid 1, located at x=0 and held at a constant potential V_1, at a speed v_1. The equation for the speed at which ions approach grid 1 (v_1) can be obtained from conservation of kinetic and electric potential energy and is

$$v_1 = \sqrt{\frac{2q(V_p - V_1)}{m}} \quad , \tag{A1}$$

where q and m are the charge per ion and mass per ion, respectively, of the ionic species being considered. In the single-stage Bennett mass spectrometer, ions are extracted from the discharge chamber through an optics system and approach grid 1 with a substantial kinetic energy obtained by falling through the potential difference between the discharge chamber plasma and grid 1. In the three-grid optics/RF mass discriminator, ions are extracted directly from the discharge chamber plasma through a sheath which develops near the screen grid (corresponds to grid 1 in Fig. A1). In general, the exact location of the sheath is not known. However, for the modelling done here, it is assumed that ions enter the system with negligible speed from a surface at plasma potential at the location of the screen grid. Therefore, although the screen grid was held at a potential slightly negative of plasma potential during experiments, for this modelling it is assumed to be at plasma potential (i.e. $V_1=V_p$).

Grid 2 is located at x=s and is maintained at a voltage with a constant component V_2 and a superimposed sinusoidal RF component characterized by an amplitude V_{RF} and a frequency f. For the single-stage Bennett mass spectrometer, the same mean potential is applied to each grid; therefore, $V_2=V_1$. In the three-grid

optics/RF mass discriminator, however, the mean potential (V_2) applied to the accel grid (corresponds to grid 2 in Fig. A1) is substantially lower than the screen grid voltage (V_1) to facilitate ion extraction from the discharge chamber.

Grid 3 is located at x=2s and is held at a constant voltage V_3. Again the same mean potential is applied to each of the grids in the single-stage Bennett mass spectrometer so $V_3=V_1$. The three-grid optics/RF mass discriminator uses the decel grid (corresponds to grid 3 in Fig. A1) to slow or stop ions and the value of V_3 can be set to any desired value.

Since magnetic and space-charge effects are neglected, the equation governing the potential variation in the intra-grid region is

$$\frac{d^2V(x,t)}{dx^2} = 0 \quad . \tag{A2}$$

Using this differential equation and the boundary conditions shown in Fig. A1, the potential between grids 1 and 2 (V_{12}) is found to be

$$V_{12}(x,t) = \left[\frac{s-x}{s}\right] V_1 + \left[\frac{x}{s}\right] \left[V_2 + V_{RF}\sin(2\pi ft)\right] \tag{A3}$$

and the potential between grid 2 and 3 (V_{23}) is

$$V_{23}(x,t) = \left[\frac{2s-x}{s}\right] \left[V_2 + V_{RF}\sin(2\pi ft)\right] + \left[\frac{x-s}{s}\right] V_3 \quad . \tag{A4}$$

The equation describing ion acceleration in the intra-grid region is obtained by combining the Lorentz force law with Newton's second law. When magnetic fields are neglected, the Lorentz force acting on a charged particle is equal to the charge multiplied by the electric field. The electric field is the gradient of the potential; therefore, the ion acceleration between grids 1 and 2 is given by

$$\frac{dv}{dt} = \frac{q}{m}\left[\frac{V_1 - V_2}{s} - \frac{V_{RF}}{s}\sin(2\pi ft)\right] \qquad \text{(A5)}$$

and between grids 2 and 3 it is

$$\frac{dv}{dt} = \frac{q}{m}\left[\frac{V_2 - V_3}{s} + \frac{V_{RF}}{s}\sin(2\pi ft)\right] \quad . \qquad \text{(A6)}$$

Before solving for the acceleration of the ions in the intra-grid region, the preceding equations will be non-dimensionalized using important system parameters as shown in the following table.

Mass per ion	$M = \frac{m}{m_{O_2}}$
Charge per ion	$Q = \frac{q}{e}$
Length	$\textcircled{\scriptsize :)} = \frac{x}{s}$
Time	$T = \frac{t}{s}\sqrt{\frac{e(V_p - V_2)}{2\,m_{O_2}}}\left[1 + \sqrt{\frac{V_p - V_1}{V_p - V_2}}\right]$
Frequency	$F = f\,s\left[\sqrt{\frac{e(V_p - V_2)}{2\,m_{O_2}}}\left(1 + \sqrt{\frac{V_p - V_1}{V_p - V_2}}\right)\right]^{-1}$
Speed	$\vartheta = v\sqrt{\frac{m_{O_2}}{2\,e\,(V_p - V_2)}}$
Potentials	$\nu = \frac{V - V_2}{V_p - V_2}$, $\nu_{RF} = \frac{V_{RF}}{V_p - V_2}$
Energy	$\xi = \frac{m\,v^2}{2q\,(V_p - V_3)}$

Table A1. Definition of Non-Dimensional Variables

Figure A2 shows the geometry and boundary conditions associated with the non-dimensional model. Grid 1 is located at $\textcircled{\scriptsize y}=0$ and is held at a constant potential ν_1. Ions extracted from the discharge chamber plasma at a potential $\nu_p=1$, approach grid 1 at a speed ϑ_1. Grid 2, located at $\textcircled{\scriptsize y}=1$, has a sinusoidal RF voltage with an amplitude ν_{RF} and a frequency F applied to it. Note that the mean potential applied to grid 2 is used as the non-dimensional reference potential. Grid 3 is located at $\textcircled{\scriptsize y}=2$ and it is held at a constant potential ν_3.

Recasting the dimensional equations in terms of non-dimensional variables, Eq. A1 becomes

$$\vartheta_1 = \sqrt{(Q/M)\,(1-\nu_1)} \quad . \tag{A7}$$

Eqs. A5 and A6 become

$$\frac{d\vartheta}{dT} = \frac{Q}{M}\left[1-\sqrt{1-\nu_1}-\left(\frac{\nu_{RF}}{1+\sqrt{1-\nu_1}}\right)\sin(2\pi FT)\right] \tag{A8}$$

and

$$\frac{d\vartheta}{dT} = \frac{Q}{M}\left[-\left(\frac{\nu_3}{1+\sqrt{1-\nu_1}}\right)+\left(\frac{\nu_{RF}}{1+\sqrt{1-\nu_1}}\right)\sin(2\pi FT)\right] \quad , \tag{A9}$$

respectively. Also, the non-dimensional kinetic energy is

$$\xi = \frac{M\,\vartheta^2}{Q(1-\nu_3)} \quad . \tag{A10}$$

In addition, the relationship between non-dimensional speed, position and time is

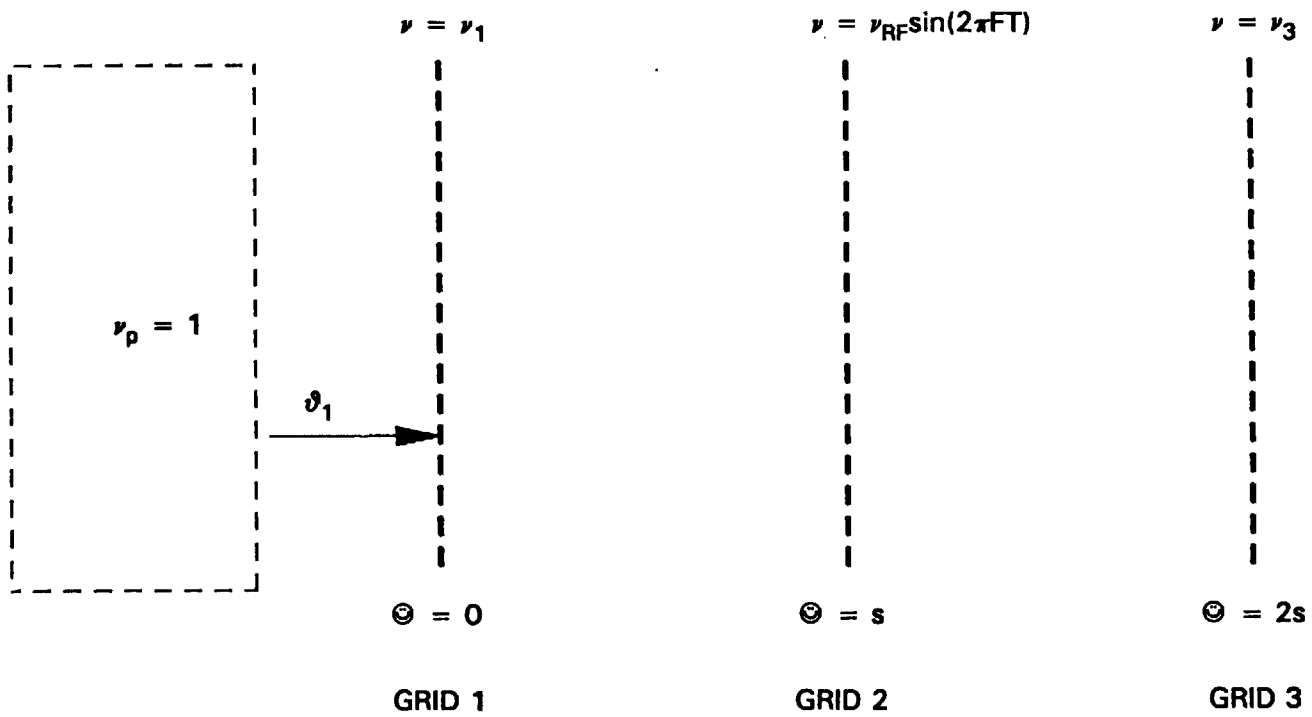

Fig. A2 Non-dimensional Geometry and Boundary Conditions for the Single-Stage Bennett Mass Spectrometer and the Three-Grid Optics/RF Mass Discriminator

$$\vartheta = \left[\frac{1+\sqrt{1-\nu_1}}{2}\right]\frac{d\textcircled{\scriptsize :)}}{dT} \quad . \tag{A11}$$

In order to determine the speed of an ion, which enters the system at time T_1 with speed ϑ_1 (given by Eq. A7), in the region between grids 1 and 2, Eq. A8 is solved to give

$$\vartheta(T) = \sqrt{\frac{Q}{M}(1-\nu_1)} + \frac{Q}{M}\left(1-\sqrt{1-\nu_1}\right)(T-T_1)$$

$$+\frac{Q}{M}\frac{\nu_{RF}}{2\pi F\left(1+\sqrt{1-\nu_1}\right)}\left[\cos(2\pi FT)-\cos(2\pi FT_1)\right] \quad . \tag{A12}$$

Using the relationship in Eq. A11 in Eq. A12, and solving for the time-dependent position of an ion that passes grid 1 at time T_1 yields

$$\textcircled{\scriptsize :)}(T) = \left[2\sqrt{\frac{Q}{M}}\left[\frac{\sqrt{1-\nu_1}}{1+\sqrt{1-\nu_1}}\right] - \frac{Q}{M}\frac{\nu_{RF}}{\pi F\left(1+\sqrt{1-\nu_1}\right)^2}\cos(2\pi FT_1)\right](T-T_1)$$

$$+\frac{Q}{M}\left[\frac{1-\sqrt{1-\nu_1}}{1+\sqrt{1-\nu_1}}\right](T-T_1)^2$$

$$+\frac{Q}{M}\frac{\nu_{RF}}{2\pi^2F^2\left(1+\sqrt{1-\nu_1}\right)^2}\left[\sin(2\pi FT)-\sin(2\pi FT_1)\right] \quad . \tag{A13}$$

In order to determine the speed of an ion, which passes grid 2 at time T_2 with a speed ϑ_2, in the region between grids 2 and 3, Eq. A9 is solved to obtain

$$\vartheta(T) = \vartheta_2 - \frac{Q}{M}\left[\frac{\nu_3}{1+\sqrt{1-\nu_1}}\right](T - T_2)$$

$$- \frac{Q}{M}\frac{\nu_{RF}}{2\pi F\left(1+\sqrt{1-\nu_1}\right)}\left[\cos(2\pi FT) - \cos(2\pi FT_2)\right] \cdot \quad \text{(A14)}$$

To obtain the time-dependent position of an ion travelling between grids 2 and 3, Eqs. A11 and A14 are used to find

$$\text{☺}(T) = 1 + \left[\frac{2\vartheta_2}{\left(1+\sqrt{1-\nu_1}\right)} + \frac{Q}{M}\frac{\nu_{RF}}{\pi F\left(1+\sqrt{1-\nu_1}\right)^2}\cos(2\pi FT_2)\right](T - T_2)$$

$$- \frac{Q}{M}\left[\frac{\nu_3}{\left(1+\sqrt{1-\nu_1}\right)^2}\right](T - T_2)^2$$

$$- \frac{Q}{M}\frac{\nu_{RF}}{2\pi^2F^2\left(1+\sqrt{1-\nu_1}\right)^2}\left[\sin(2\pi FT) - \sin(2\pi FT_2)\right] \cdot \quad \text{(A15)}$$

Equations A12-A15 can be solved numerically to obtain the terminal ion energy for the single-stage Bennett mass spectrometer and to determine the stopping potential for the three-grid optics/RF mass discriminator. However, because the RF voltage is a small perturbation to the steady-state solution, a first-order (in ν_{RF}) solution for both the terminal ion energy and the stopping potential are derived. This analytical approximation will show the functional dependence of both parameters on effective frequency ($F\tau$).

To solve for both the terminal ion energy and the stopping potential, the conditions at grid 3 are needed and these are found using Eqs. A14 and A15. In

order to solve these equations, however, the speed of ions at grid 2 is needed. Therefore, a first-order solution for the speed of the ions at grid 2 is found from Eqs. A12 and A13. To obtain the first-order solution, speed, position and time are linearized as a steady-state term plus a perturbation term as follows.

$$\vartheta = \overline{\vartheta} + \nu_{RF}\vartheta' \tag{A16}$$

$$\text{☺} = \overline{\text{☺}} + \nu_{RF}\text{☺}' \tag{A17}$$

$$T = T_1 + \overline{\Delta} + \nu_{RF}\Delta' \tag{A18}$$

In Eq. A18, $\overline{\Delta}$ is the time it takes an ion to travel from grid 1 to a given location under steady-state conditions and Δ' is the first-order perturbation in this travel time.

Plugging Eqs. A16 and A18 into Eq A12 and keeping terms through first order in ν_{RF} yields the steady-state equation

$$\overline{\vartheta} = \sqrt{\frac{Q}{M}(1-\nu_1)} + \frac{Q}{M}\left(1-\sqrt{1-\nu_1}\right)\overline{\Delta} \tag{A19}$$

and the equation due to the first-order perturbation

$$\vartheta' = \frac{Q}{M}\left\{\left(1-\sqrt{1-\nu_1}\right)\Delta'\right.$$

$$+\frac{1}{2\pi F\left(1+\sqrt{1-\nu_1}\right)}\left[\left(1-\cos(2\pi F\overline{\Delta})\right)\cos(2\pi FT)\right.$$

$$\left.\left.-\left(\sin(2\pi F\overline{\Delta})\right)\sin(2\pi FT)\right]\right\} \tag{A20}$$

Plugging Eqs. A17 and A18 into Eq. A13 and keeping terms through first order in

ν_{RF} yields the steady-state equation

$$\overline{\omega} = 2\sqrt{\frac{Q}{M}}\left[\frac{\sqrt{1-\nu_1}}{1+\sqrt{1-\nu_1}}\right]\overline{\Delta} + \frac{Q}{M}\left[\frac{1-\sqrt{1-\nu_1}}{1+\sqrt{1-\nu_1}}\right]\overline{\Delta}^2 \qquad \text{(A21)}$$

and the equation due to the first-order perturbation

$$\omega' = 2\left[\sqrt{\frac{Q}{M}}\left[\frac{\sqrt{1-\nu_1}}{1+\sqrt{1-\nu_1}}\right] + \frac{Q}{M}\left[\frac{1-\sqrt{1-\nu_1}}{1+\sqrt{1-\nu_1}}\right]\overline{\Delta}\right]\Delta'$$

$$-\frac{Q}{M}\frac{\overline{\Delta}}{\pi F\left(1+\sqrt{1-\nu_1}\right)^2}\cos\left(2\pi F(T-\overline{\Delta})\right)$$

$$+\frac{Q}{M}\frac{1}{2\pi^2F^2\left(1+\sqrt{1-\nu_1}\right)^2}\left[\sin(2\pi FT) - \sin\left(2\pi F(T-\overline{\Delta})\right)\right] \qquad \text{(A22)}$$

The first-order solution for the ion speed is desired at $\omega = 1$; therefore, Eqs. A21 and A22 are evaluated at $\overline{\omega}(\omega=1) = 1$ and $\omega'(\omega=1) = 0$. Eq. A21 is evaluated to find the steady-state time which it takes an ion to travel between grids 1 and 2, namely $\overline{\Delta}(\omega=1) = \tau$, which is found to be

$$\tau = \sqrt{\frac{M}{Q}} \qquad \text{(A23)}$$

Equation A22 is then evaluated to determine the first-order perturbation in the ion travel time at grid 2, namely $\Delta'(\omega=1) = \tau'$, which is found to be

$$\tau' = \frac{\sqrt{\frac{M}{Q}}}{\left(1+\sqrt{1-\nu_1}\right)}\left[\frac{\cos[2\pi F(T_2-\tau)]}{2\pi F\tau}\right.$$

$$\left. - \frac{(\sin(2\pi FT_2) - \sin[2\pi F(T_2-\tau)])}{(2\pi F\tau)^2}\right] \quad . \tag{A24}$$

These expressions for τ and τ' are used in Eqs. A19 and A20 to find $\bar{\vartheta}_2$ and ϑ_2', respectively. Combining these speeds as shown in Eq. A16 yields the speed of the ions at the second grid, to first order, which is found to be

$$\vartheta_2 = \sqrt{\frac{Q}{M}}\left\{1+\left[\frac{\nu_{RF}}{1+\sqrt{1-\nu_1}}\right]\left[\left[\frac{1-\sqrt{1-\nu_1}\cos(2\pi F\tau)}{(2\pi F\tau)}\right.\right.\right.$$

$$\left.\left. - \frac{\left(1-\sqrt{1-\nu_1}\right)\sin(2\pi F\tau)}{(2\pi F\tau)^2}\right]\cos(2\pi FT_2)\right.$$

$$\left. - \left[\frac{\sqrt{1-\nu_1}\sin(2\pi F\tau)}{(2\pi F\tau)}\right.\right.$$

$$\left.\left.\left. + \frac{\left(1-\sqrt{1-\nu_1}\right)(1-\cos(2\pi F\tau))}{(2\pi F\tau)^2}\right]\sin(2\pi FT_2)\right]\right\} \tag{A25}$$

This expression for ϑ_2 is valid for both the single-stage Bennett mass spectrometer and the three-grid optics/RF mass discriminator. At this point the problem will be specialized to solve either for the terminal ion energy for the single-stage Bennett mass spectrometer or for the stopping potential for the three-grid optics/RF mass

discriminator.

To begin the derivation of the first-order solution for the terminal ion energy, recall that the same mean potential is applied to all three single-stage Bennett mass spectrometer grids and that the mean potential applied to grid 2 is used as the reference potential in the non-dimensional model. Therefore, the non-dimensional boundary conditions for the single-stage Bennett mass spectrometer are $\nu_1=\nu_3=0$. As was done between grids 1 and 2, speed and distance are linearized as shown in Eqs. A16 and A17 and time is linearized to first order in ν_{RF} between grids 2 and 3 as follows.

$$T = T_2 + \bar{\Delta} + \nu_{RF}\Delta' \tag{A26}$$

Here $\bar{\Delta}$ is the steady-state time that an ion takes to travel from grid 2 to a given location and Δ' is the first-order perturbation in this time.

Using the boundary conditions for the single-stage Bennett mass spectrometer, plugging Eqs. A16, A25 and A26 into Eq. A14 and keeping terms to first order in ν_{RF} yields the following steady-state equation for the ion speed between grids 2 and 3

$$\bar{\vartheta} = \sqrt{\frac{Q}{M}} \tag{A27}$$

and the equation due to the first-order perturbation is

$$\vartheta' = \frac{1}{2}\sqrt{\frac{Q}{M}}\left[\left[\frac{1-\cos(2\pi F\tau)}{2\pi F\tau}\right]\cos\left(2\pi F(T-\bar{\Delta})\right) - \left[\frac{\sin(2\pi F\tau)}{2\pi F\tau}\right]\sin\left(2\pi F(T-\bar{\Delta})\right)\right] - \frac{Q}{M}\frac{1}{4\pi F}\left[\cos(2\pi FT) - \cos\left(2\pi F(T-\bar{\Delta})\right)\right] . \tag{A28}$$

Note that τ' does not appear in the first-order perturbation of the ion speed; therefore, when Eqs. A17, A25 and A26 are plugged into Eq. A15, only the steady-state equation is needed. It is found to be

$$\bar{\vartheta} = 1 + \sqrt{\frac{Q}{M}}\,\bar{\Delta} \quad . \tag{A29}$$

Since the first-order solution for the speed of an ion arriving at the third grid is desired, Eq. A29 is evaluated at $\bar{\vartheta}(\vartheta=2) = 2$, where it is found that $\bar{\Delta}(\vartheta=2) = \sqrt{M/Q} = \tau$. Plugging this back into Eq. A28, the speed, to first order, of the ions when they reach grid 3 is determined to be

$$\vartheta_3 = \sqrt{\frac{Q}{M}}\left\{1 + \left[\frac{\nu_{RF}}{2}\right]\left[\left[\frac{2\sin(2\pi F\tau) - \sin(4\pi F\tau)}{2\pi F\tau}\right]\sin(2\pi FT_3)\right.\right.$$
$$\left.\left. - \left[\frac{1 - 2\cos(2\pi F\tau) + \cos(4\pi F\tau)}{2\pi F\tau}\right]\cos(2\pi FT_3)\right]\right\} . \tag{A30}$$

The ion kinetic energy at grid 3 can also be linearized as

$$\xi = \bar{\xi} + \nu_{RF}\xi' \quad . \tag{A31}$$

Using Eqs. A30 and A31 in Eq. A10 and keeping terms to first order in ν_{RF} yield the following first-order expression for the terminal ion energy from a single-stage Bennett mass spectrometer

$$\xi = 1 + \nu_{RF}\left[\left[\frac{2\sin(2\pi F\tau) - \sin(4\pi F\tau)}{2\pi F\tau}\right]\sin(2\pi FT)\right.$$
$$\left. - \left[\frac{1 - 2\cos(2\pi F\tau) + \cos(4\pi F\tau)}{2\pi F\tau}\right]\cos(2\pi FT)\right] \quad . \tag{A32}$$

Using trigonometric identities this can be rewritten as

$$\xi = 1 + \nu_{RF}\,\psi \sin(2\pi F T + \delta) \tag{A33}$$

where

$$\psi = \sqrt{\left[\frac{2\sin(2\pi F\tau) - \sin(4\pi F\tau)}{2\pi F\tau}\right]^2 + \left[\frac{1 - 2\cos(2\pi F\tau) + \cos(4\pi F\tau)}{2\pi F\tau}\right]^2} \tag{A34}$$

and

$$\delta = \tan^{-1}\left[\frac{-1 + 2\cos(2\pi F\tau) - \cos(4\pi F\tau)}{2\sin(2\pi F\tau) - \sin(4\pi F\tau)}\right] . \tag{A35}$$

Here the product of ψ (the energy spread parameter) and the RF voltage gives the magnitude of the maximum perturbation of the ion energy to first order. Thus Eqs. A33-A35 give the first-order solution for the terminal ion energy from the single-stage Bennett mass spectrometer.

Now that the first-order solution for the terminal ion energy has been derived for the single-stage Bennett mass spectrometer, a first-order solution for the stopping potential in the three-grid optics/RF mass discriminator will be derived. The first-order solution for the terminal ion energy can be derived by linearizing the speed, position and time using Eqs. A16, A17 and A26, respectively. In addition, the potential applied to grid 3 is linearized as follows.

$$\nu_3 = \overline{\nu_3} + \nu_{RF}\nu_3' \tag{A36}$$

Recall that for the three-grid optics/RF mass discriminator $\nu_1 = 1$. Using this boundary condition, plugging Eqs. A16, A25, A26, A36 into Eq. A14 and expanding to first order yields the steady-state equation

$$\overline{\vartheta} = \sqrt{\frac{Q}{M}} - \frac{Q}{M}\overline{\nu_3}\overline{\Delta} \tag{A37}$$

The equation due to the first-order perturbation of the ion speed is not needed to solve for the stopping potential; therefore, it is not listed here. To determine the first-order solution for the stopping potential, however, the position equation must expanded through first order in ν_{RF}. To find these equations, plug Eqs. A17, A25, A26 and A36 into Eq. A15 and keep terms through first order in ν_{RF}. This yields the steady-state equation

$$\overline{\text{☹}} = 1 + 2\sqrt{\frac{Q}{M}}\,\overline{\Delta} - \frac{Q}{M}\overline{\nu_3}\overline{\Delta}^2 \tag{A38}$$

and the equation due to the first-order perturbation

$$\begin{aligned}
\text{☺}' = {} & 2\left[\sqrt{\frac{Q}{M}} - \frac{Q}{M}\overline{\nu_3}\,\overline{\Delta}\right]\Delta' - \left[\frac{Q}{M}\overline{\Delta}^2\right]\nu_3' \\
& + 2\overline{\Delta}\sqrt{\frac{Q}{M}}\left[\left[\frac{1}{2\pi F\tau} - \frac{\sin(2\pi F\tau)}{(2\pi F\tau)^2}\right]\cos\left(2\pi F(T-\overline{\Delta})\right)\right. \\
& \left. - \left[\frac{1-\cos(2\pi F\tau)}{(2\pi F\tau)^2}\right]\sin\left(2\pi F(T-\overline{\Delta})\right)\right] \\
& + \frac{Q}{M}\frac{\overline{\Delta}}{\pi F}\cos\left(2\pi F(T-\overline{\Delta})\right) \\
& - \frac{Q}{M}\frac{1}{2\pi^2F^2}\left[\sin(2\pi FT) - \sin\left(2\pi F(T-\overline{\Delta})\right)\right]
\end{aligned} \tag{A39}$$

The potential required to stop an ion at grid 3 is found be setting $\vartheta = 0$ and ☹ = 2.

Simultaneous evaluation of Eqs. A37 and A38 at $\bar{\vartheta}(\vartheta=0,\ \text{☺}=2) = 0$ and at $\bar{\text{☺}}(\vartheta=0,\ \text{☺}=2) = 2$, respectively, yields the steady-state stopping potential $\nu_3(\vartheta=0,\ \text{☺}=2) = \nu_* = 1$ and the steady-state time for an ion to travel between grids 2 and 3 $\bar{\Delta}(\vartheta=0,\ \text{☺}=2) = \tau_* = \sqrt{M/Q} = \tau$. To find the first-order perturbation of the potential required to stop an ion arriving at grid 3, Eq. A39 is evaluated at $\text{☺}'(\vartheta=0,\ \text{☺}=2) = 0$. Note that when τ is plugged into Eq. A39 the term multiplying the Δ' term is zero; therefore, the first-order perturbation in the potential required to stop an ion arriving at grid 3, $\nu_3'(\vartheta=0,\ \text{☺}=2) = \nu_*'$, can be found directly from Eq. A39 and it is

$$\nu_*' = 2\left[\left[\frac{2\cos(2\pi F\tau)}{2\pi F\tau} - \frac{\sin(4\pi F\tau)}{(2\pi F\tau)^2}\right]\cos(2\pi FT_3) + \left[\frac{2\sin(2\pi F\tau)}{2\pi F\tau} - \frac{1-\cos(4\pi F\tau)}{(2\pi F\tau)^2}\right]\sin(2\pi FT_3)\right] \tag{A40}$$

Using trigonometric identities this can be rewritten as

$$\nu_*' = \Phi\sin(2\pi FT + \delta) \tag{A41}$$

where

$$\Phi = 2\sqrt{\left[\frac{2\cos(2\pi F\tau)}{2\pi F\tau} - \frac{\sin(4\pi F\tau)}{(2\pi F\tau)^2}\right]^2 + \left[\frac{2\sin(2\pi F\tau)}{2\pi F\tau} - \frac{1-\cos(4\pi F\tau)}{(2\pi F\tau)^2}\right]^2} \tag{A42}$$

and

$$\delta = \tan^{-1}\left[\frac{\left[\frac{2\cos(2\pi F\tau)}{2\pi F\tau} - \frac{\sin(4\pi F\tau)}{(2\pi F\tau)^2}\right]}{\left[\frac{2\sin(2\pi F\tau)}{2\pi F\tau} - \frac{1-\cos(4\pi F\tau)}{(2\pi F\tau)^2}\right]}\right] \tag{A43}$$

The stopping potential is the potential which must be applied to grid 3 to stop the most energetic ions at the third grid, which is equal to the steady-state stopping potential plus the maximum value of the first-order perturbation. Since the maximum value of ν_*' occurs, in Eq. A41, when the sine factor is 1, the product of Φ (the stopping potential parameter) and the RF voltage gives the first-order perturbation on the stopping potential. Thus, to first-order the stopping potential ν_s is given by

$$\nu_s = 1 + \nu_{RF}\,\Phi \tag{A44}$$

Thus, the stopping potential is determined, to first order using Eqs. A44 and A42.

Finally, a brief discussion about the use of the non-dimensional values to present experimental data are in order. Experimental results are given in terms of appropriate non-dimensional variables; however, experiments are always carried out at specific conditions which have dimensional values. The equations in Table A1 are used to define the non-dimensional variables. From these equations it is seen that the actual operating conditions can be identified if the ion species as well as dimensional values for three variables is given along with the non-dimensional conditions. To identify the ion species the gas which is fed into the discharge chamber is given and referred to as the source gas. The three variables chosen to identify dimensional operating conditions are the grid spacing (s), a potential difference (V_p - V_2) and the mean potential applied to grid 2 (V_2). These values are listed when experimental data are presented.

Discussion of the potentials is warranted because the potentials are identified with different parameters in the single-stage Bennett mass spectrometer and the three-grid optics/RF mass discriminator. In the single-stage Bennett mass spectrometer $V_2 = 0$; since this is implicitly understood, it is not listed with data. The potential difference (V_p - V_2) multiplied by the charge on an ion corresponds to the energy that such an ion would have while travelling through the spectrometer in the steady-state case and is termed the mean ion energy. Thus in addition to the source gas, the dimensional values which are listed for the single-stage Bennett mass spectrometer are the grid spacing and the mean ion energy.

For the three-grid optic-RF mass discriminator, the potential difference (V_p-V_2) corresponds to the total-accelerating voltage in the steady-state case; here it is referred to as the mean-total-accelerating voltage. The mean potential applied to the accel grid (V_2) is always below ground potential in the three-grid optics/RF mass discriminator and is referred to as the mean accel potential. Thus for the three-grid optics/RF mass discriminator, the dimensional values that are listed along with the source gas are the grid spacing, the mean-total-accelerating voltage and the mean accel potential.

APPENDIX B

Electron-Induced Errors in Probe Data

The retarding potential analyzer (RPA), Faraday probe and ExB probe each have a Faraday cages surrounding the sensor (collector) plate used to measure ions. The Faraday cage of both the RPA and Faraday probe have a 2 mm dia aperture which ions can pass through and the cage is biased negative to keep electrons from passing through the aperture and reaching the collector. Although electrons should not have been able to reach the collector, negative currents were observed in RPA probe data under certain operating conditions.

Before discussing the cases where negative currents were observed, it is worthwhile to describe the conditions at which the RPA works properly. Figure 14 shows raw RPA data obtained from the three-grid optics/RF mass discriminator. These data are obtained with the RPA collector held at ground potential and the decel grid is used to stop ions. Also, the Faraday cage is biased negative enough to stop electrons from entering the aperture. This is observed to be the case because the current density[6] is observed to go to zero and remain zero at high retarding potentials. Thus, the RPA is operating in the desired manner; namely, the only species being detected are positive ions.

Since the RPA functions correctly when data are obtained from the three-grid optics/RF mass discriminator, it might be anticipated that there would be no errors

---

[6]The RPA actually measures the current to the collector and the current density (such as that shown in Fig. 14) is determined by dividing this current by the area of the 2 mm dia aperture.

due to electron collection when the RPA is used to measure ion energies for the single-stage Bennett mass spectrometer. However, this is not the case. Fig. B1 shows the raw RPA data of the "corrected" trace shown in Fig. 7. In Fig. B1 it is observed that the current density arriving at the collector is relatively constant at low retarding potentials and its magnitude is denoted J_+. It is observed that the current density goes negative at a retarding potential near 1.17 and the curve levels out at a relatively constant value at a retarding potential near 1.21. The magnitude of this negative current density is denoted J_- and it is less than 20% of the ion current density measured at low retarding potentials. This is typical for RPA traces obtained while using the single-stage Bennett mass spectrometer. This negative current density represents an error in RPA measurements and a simple equation has been developed to account for these electrons and correct raw RPA data.

In order to determine why the RPA works properly for the three-grid optics/RF mass discriminator but not for the single-stage Bennett mass spectrometer, the difference in modes of operation between the two cases must be examined. In the three-grid optics/RF mass discriminator the retarding potential is applied to the decel grid which stops ions before they reach the Faraday cage. In the single-stage Bennett mass spectrometer the retarding potential is applied to the collector which stops ions after they enter the Faraday cage. To see how ions stopped after they have entered the Faraday cage might cause the observed negative current density, Fig. B2 shows several current associated with RPA data collection. The ion current passing through the 2 mm aperture, denoted I_+, is assumed to remain constant as the retarding potential changes. This current is equal to the maximum positive current density J_+ multiplied by the area of the 2 mm dia aperture. After this current enters the Faraday cage a fraction of it goes to the collector and the rest of the current is repelled away from the collector. The ion current to the collector is denoted I_i and the current

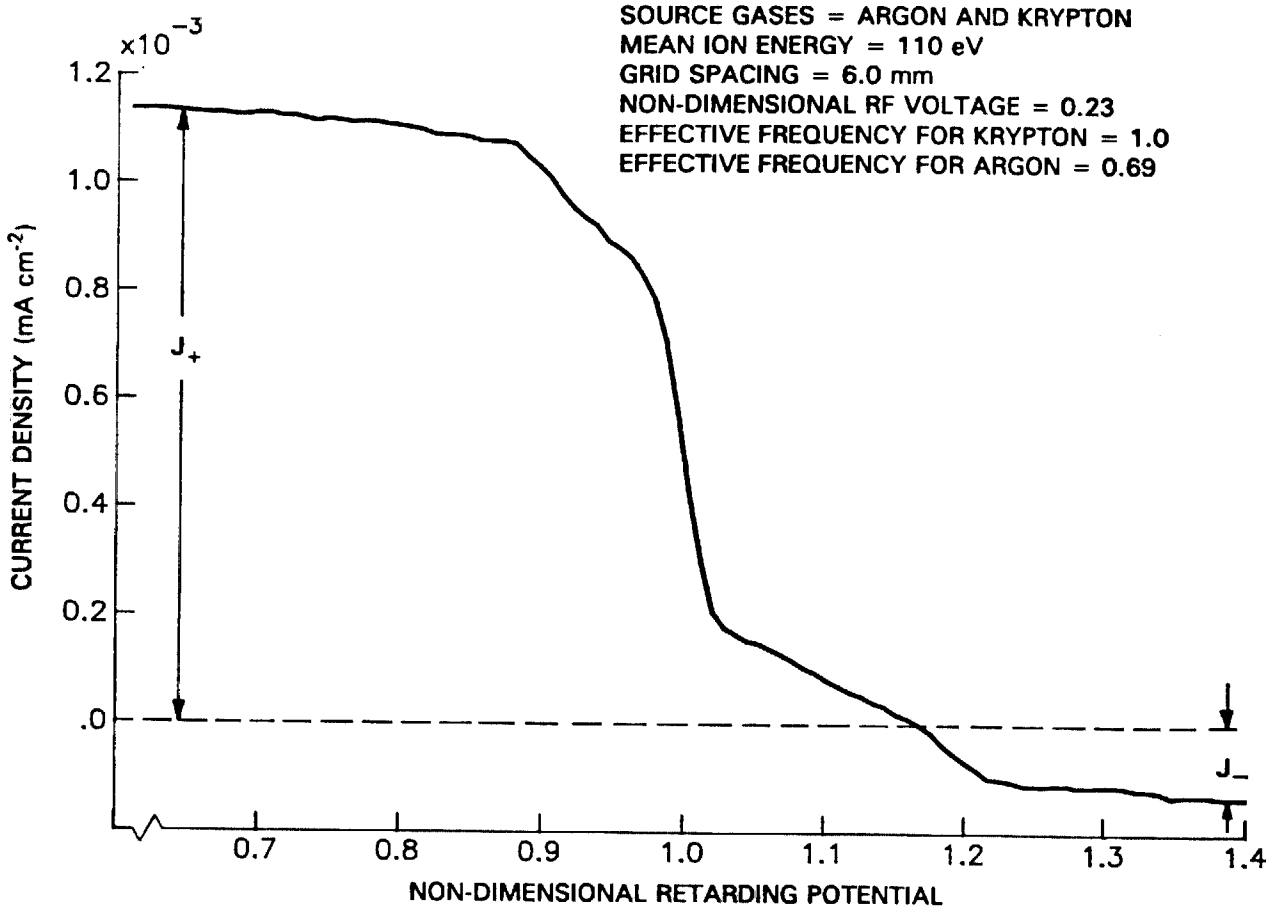

Fig. B1 Raw RPA Data for a Krypton-Argon Ion Beam

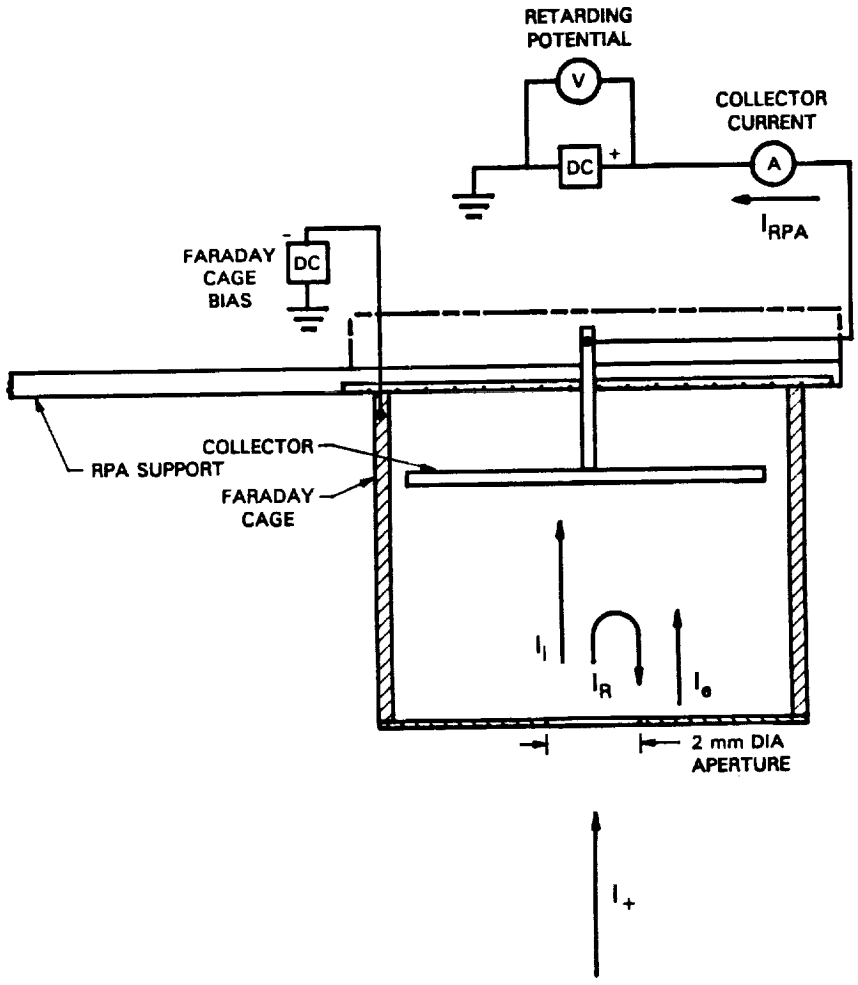

Fig. B2 RPA Currents Flowing During Single-Stage Bennett Mass Spectrometer Testing

repelled by the collector is denoted I_R. The fraction of I_+ going into I_i and I_R depends on the retarding potential applied to the collector. At low retarding potentials all ions strike the collector so $I_+ = I_i$ and at high retarding potentials all ions are repelled and $I_+ = I_R$. The ions which are repelled by the collector can either leave the Faraday cage through the aperture or they can impinge on the inside surfaces of the cage. Ions which are repelled onto the inside surfaces of the Faraday cage can cause secondary electron emission. Since the Faraday cage is always at a more negative potential than the collector these electrons will travel to the collector and be sensed as a negative current. In Fig. B2 the magnitude of this secondary electron current is denoted I_e. The last current to be described is denoted I_{RPA} and it is the current measured with the collector current ammeter shown in Fig. B2. I_- is the magnitude of the secondary electron current going to the collector when all of the ions are repelled. In Fig. B1 the negative current density J_- is equal to I_- divided by the area of the aperture.

The current measured by the ammeter, I_{RPA}, is due to both ions and secondary electrons and is given by

$$I_{RPA} = I_i - I_e \tag{B1}$$

The magnitude of the current due to repelled ions, I_R, is the total ion current passing through the 2 mm dia aperture minus the ion current arriving at the collector and is given by

$$I_R = I_+ - I_i \tag{B2}$$

It is assumed that the fraction f of repelled ions which strike the inside surfaces of the

Faraday cage remains constant over the range of retarding potentials at which ions are repelled (the fraction of repelled ions escaping through the 2 mm dia aperture is 1-f). The magnitude of the secondary electron current I_e is equal to the product of the secondary electron emission coefficient g and the repelled ion current striking the inside surfaces of the Faraday cage and is given by

$$I_e = g f I_R \tag{B3}$$

When the retarding potential is high enough to repel all ions, $I_R = I_+$ and $I_e = I_-$. Using these relations and also assuming that the secondary electron coefficient is constant over the range of energies at which repelled ions strike the inside surfaces of the Faraday cage, Eq. B3 can be solved for the constant product gf to obtain

$$g f = \frac{I_-}{I_+} \tag{B4}$$

Using Eqs. B1, B2, B3 and B4, the following expression for the ion current I_i is obtained

$$I_i = \frac{I_{RPA} + I_-}{1 + \left(\frac{I_-}{I_+}\right)} \tag{B5}$$

This is the formula used to correct raw RPA traces, such as the one in Fig. B1, for secondary electron errors. For this trace the corrected current I_i is divided by the aperture area and is plotted as a function of retarding potential in Fig. 7. It is noted that if $I_- = 0$, $I_i = I_{RPA}$. In words, the current which is measured is the actual ion

current and no correction is necessary. This is the case in RPA traces like those of Fig. 14.

During both three-grid optics/RF mass discriminator and single-stage Bennett mass spectrometer experiments, the Faraday probe was operated with the collector at ground potential. In addition, the Faraday cage was always biased to a potential that was sufficiently negative to keep electrons from passing through the aperture. The probe was operated at conditions where all ions passing through the aperture should have reached the collector and none of the ions should have impinged on the inside surfaces of the Faraday cage. This and the fact that the current to the collector is observed to decrease to zero when the Faraday probe is out of the beam indicate that errors due to electron collection are negligible.

The Faraday cage surrounding the **ExB** probe collector was also biased negative to stop stray electron which might approach it. Although it was anticipated that negative currents would not be observed, a 0.8 pico-amp negative offset was measured in all **ExB** data. The exact cause of this offset has not been determined; however, calibration of the ammeter used to make the measurements indicated that it was zeroed correctly. The negative current is probably a small leakage current in the probe because it is also observed in **ExB** probe traces taken when the ion source is not being operated. Because the negative current appears to be a constant leakage current, it is subtracted off the **ExB** probe data.

It is also noted that the current signal to the **ExB** probe collector tended to be noisy. Therefore, averaging procedure was used to filter out the noise. To obtain the **ExB** probe traces, the plate potential difference was varied between 0 and 30 V in 0.1 V increments. At each plate potential difference, three current measurements were obtained and the average and standard deviation of these measurements were computed. The average and the standard deviation were needed to fit the data with a

Chebyshev polynomial series [28] using the general linear least squares fit technique described in the literature [29]. Once the coefficients of the Chebyshev polynomial series had been computed, the series was summed to obtain **ExB** traces like those shown in Figs. 18-20 and 22.

Appendix C

A Fourier-Series Technique for Differentiating Experimental Data

A general procedure for applying Fourier sine series to obtain derivatives of experimental data is developed in this appendix. The mathematics described can be used in any application requiring differentiation of experimental data; however, analytical functions and Retarding Potential Analyzer (RPA) data will be used to demonstrate the usefulness of the technique.

In experimental work one often obtains discrete data pairs of the form $[\epsilon, I(\epsilon)]$ over some range $\epsilon = \epsilon_o$ to $\epsilon = \epsilon_o + E$. For example, Retarding Potential Analyzer (RPA) data are collected in the form of a plot of positive ion current to a probe (I) as a function of retarding potential applied to the probe (ϵ). Numerically the value of applied retarding potential in volts is equal to the kinetic energy of the ions in eV, assuming singly charged ions are collected and that ions have this kinetic energy at the reference potential (i.e. at 0 V). For RPA traces the ion energy distribution function is obtained using

$$\frac{d\eta}{d\epsilon} = -\sqrt{\frac{m}{2\epsilon}}\,\frac{1}{eA}\,\frac{dI}{d\epsilon} \qquad \text{(C1)}$$

where η is the ion number density (in m^{-3}), m is the ion mass (in kg), ϵ is the ion energy (in J), e is the electronic charge (in Coulombs) and A is the area (in m^2) through which current flows to the plate. Obviously, the function $I(\epsilon)$ must be differentiated to determine the energy distribution function. The method being proposed here to obtain this derivative, is to use a finite Fourier sine series to fit the original data and to then differentiate this series term by term. In order to ensure that

this differentiated series converges, the Lanczos [30] convergence factor should be used. Before discussing this factor, it is appropriate to discuss some of the drawbacks of Fourier series techniques. The Lanczos convergence factor will then be presented and examples (using data pairs obtained from analytical functions and experimental RPA data) demonstrating how this factor improves the convergence of Fourier sine series will be given. These examples will also illustrate some of the problems that can still arise when using this technique.

A standard finite Fourier series [31] representation can be used to represent a function $I(\epsilon)$ on the open interval $(\epsilon_o, \epsilon_o + E)$. This Fourier series is periodic with period E and converges to $I(\epsilon)$ in the open interval $(\epsilon_o, \epsilon_o + E)$, but the series converges to the average value $1/2[I(\epsilon_o) + I(\epsilon_o + E)]$ at the interval endpoints ϵ_o and $\epsilon_o + E$. Therefore, unless $I(\epsilon_o) = I(\epsilon_o + E)$, the Fourier series will not converge to $I(\epsilon)$ at the interval endpoints. If the Fourier series is discontinuous at any point including the interval endpoints, the Gibbs phenomenon is observed when a finite number of terms is used to approximate $I(\epsilon)$. The Gibbs phenomenon is manifest as an overshoot of the finite Fourier series which makes it difficult to estimate $I(\epsilon)$ near points of discontinuity. Another problem that arises if $I(\epsilon)$ has discontinuities, is that the derivative of the Fourier series does not converge. Because of these problems, the standard Fourier series has limited usefulness in many applications. However, the convergence problems can be overcome by using the Lanczos convergence factor. It is also possible to eliminate the discontinuity at the interval end points for both the function and its first derivative. This involves subtracting off the straight line connecting the data at the interval end points and using a Fourier sine series to approximate the remainder. The appropriate math for obtaining the Fourier sine series and the Lanczos convergence factor is described below.

The standard Fourier sine series representation of a function G(u) on the open

interval $(0, 2\pi)$ is given by

$$G(u) = \sum_{n=1}^{N} a_n \sin\left[\frac{nu}{2}\right] \tag{C2}$$

where

$$a_n = \frac{1}{\pi}\int_0^{2\pi} G(u)\sin\left[\frac{nu}{2}\right] du \tag{C3}$$

Since the Fourier sine series is defined on the interval $(0, 2\pi)$ and the data is given on the interval $(\epsilon_o, \epsilon_o + E)$, a method of mapping between the intervals is needed. The simplest mapping is the linear mapping

$$u = \left[\frac{2\pi}{E}\right](\epsilon - \epsilon_o) \tag{C4}$$

Also, for numerical stability, the dependent variable can be mapped from the interval (I_{min}, I_{max}), where I_{min} and I_{max} are the minimum and maximum values of $I(\epsilon)$ in the interval $(\epsilon_o, \epsilon_o + E)$, into the interval (-1, 1) using

$$H = \frac{2I - I_{min} - I_{max}}{I_{max} - I_{min}} \tag{C5}$$

Thus the data pairs $[\epsilon, I(\epsilon)]$ are mapped into [u, H(u)] data pairs.

The function H(u) will now be approximated analytically. As mentioned above, the discontinuity at the interval end points can be eliminated if the straight line connecting these points is subtracted from H(u). This yields a new function G(u) defined by

$$G(u) = H(u) - \left[\left[\frac{H(2\pi) - H(0)}{2\pi} \right] u + H(0) \right] \tag{C6}$$

Using the Fourier sine series representation (obtained from Eqs. 2 and 3), both G(u) and its first derivative will be continuous at the interval end points.

Although the discontinuity at the interval end points has been eliminated for the function and its first derivative, the Gibbs phenomenon can still be encountered if the function has a discontinuity within the interval. To remedy this problem, the standard Fourier sine series in Eq. 2 can be modified with the Lanczos convergence factor. The main idea behind this factor is to modify the standard Fourier sine series so that the derivative will converge by applying a finite difference operator D_N to the finite Fourier series. D_N is defined by

$$D_N F(u) = \frac{F(u + \gamma/N) - F(u - \gamma/N)}{2\gamma/N} \tag{C7}$$

where γ is a finite constant. From this definition it is seen that,

$$\lim_{N \to \infty} D_N F(u) = \frac{dF(u)}{du} \tag{C8}$$

therefore,

$$\lim_{N \to \infty} D_N = \frac{d}{du} \tag{C9}$$

Thus, it is seen that for large N, D_N provides a reasonable approximation of the derivative operator d/du. Applying D_N to G(u) gives

$$D_N G(u) = \frac{N}{2\gamma} \left\{ \sum_{n=1}^{N} a_n \sin \left[\frac{n}{2} \left[u + \frac{\gamma}{N} \right] \right] - \sum_{n=1}^{N} a_n \sin \left[\frac{n}{2} \left[u - \frac{\gamma}{N} \right] \right] \right\} \tag{C10}$$

Using trigonometric identities, the fundamental theorem of calculus and performing

straight forward algebra, the following is obtained

$$D_N G(u) = \frac{d}{du}\left\{ \sum_{n=1}^{N} a_n \left[\frac{\sin\left[\frac{n\gamma}{2N}\right]}{\left[\frac{n\gamma}{2N}\right]} \right] \sin\left[\frac{nu}{2}\right] \right\} \qquad \text{(C11)}$$

The value of the factor γ in Eqs. 10 and 11 must still be chosen. If $\gamma = 0$ is used, the standard Fourier sine series is obtained and the Gibbs phenomenon is observed at discontinuities. As γ increases, the Gibbs overshoot decreases but the Fourier sine series representation broadens at the discontinuity. (That is, the sine series representation accomplishes the jump over an increasingly broader range.) Lanczos does not appear to have addressed the issue of what value of γ gives the optimal trade-off between reducing the Gibbs overshoot and the broadening at a discontinuity; he simply used the length of the interval, $\gamma = 2\pi$. Although no theoretical work has been done to determine the best value, $\gamma = 2\pi$ is deemed to be a reasonable choice and will be used here. Thus, Eq. 11 becomes

$$D_N G(u) = \frac{d}{du}\left\{ \sum_{n=1}^{N-1} a_n \left[\frac{\sin\left[\frac{n\pi}{N}\right]}{\left[\frac{n\pi}{N}\right]} \right] \sin\left[\frac{nu}{2}\right] \right\} \qquad \text{(C12)}$$

(Note that this series is summed from n = 1 to N-1 because $\sin(n\pi/N) = 0$ when n = N.) From this it is evident that the finite Fourier sine series should be written as

$$G(u) = \sum_{n=1}^{N-1} a_n \left[\frac{\sin\left[\frac{n\pi}{N}\right]}{\left[\frac{n\pi}{N}\right]} \right] \sin\left[\frac{nu}{2}\right] \qquad \text{(C13)}$$

The factor $\sin(n\pi/N)/(n\pi/N)$ is called the Lanczos convergence factor; it causes the

finite Fourier sine series to converge to G(u) faster because it attenuates the high frequency terms which cause the Gibbs phenomenon. Consequently, the derivative of G(u) will converge even if G(u) has discontinuities. The derivative of G(u) will converge, if the first power of the Lanczos convergence factor is inserted into the standard Fourier sine series before differentiation; however, better convergence is achieved if the square of this factor is inserted before differentiation. In general, the best convergence is achieved if the Lanczos convergence factor is raised to the m+1 power before the m^{th} derivative of the Fourier sine series is taken.

Including the Lanczos factor, the analytical approximation of H(u) is found by combining Eqs. 6 and 13 to obtain,

$$H(u) = \left[\frac{H(2\pi) - H(0)}{2\pi}\right] u + H(0) + \sum_{n=1}^{N-1} a_n \left[\frac{\sin\left[\frac{n\pi}{N}\right]}{\left[\frac{n\pi}{N}\right]}\right] \sin\left[\frac{nu}{2}\right] \qquad (C14)$$

Although an analytical approximation to H(u) has been obtained, it is the representation of $I(\epsilon)$ that is desired. This is obtained from the inverse linear mapping

$$I(\epsilon) = \left[\frac{I_{max} - I_{min}}{2}\right] H(u) + \left[\frac{I_{max} + I_{min}}{2}\right] \qquad (C15)$$

where H(u) is defined by Eq. 14 and u is related to ϵ by Eq. 4. Eq. 1 requires that the first derivative of I with respect to ϵ be determined. Differentiating both sides of Eq. 4, it is evident that du and $d\epsilon$ are related by

$$du = \left[\frac{2\pi}{E}\right] d\epsilon \qquad (C16)$$

Thus using Eqs. 15 and 16 it is found that

$$\frac{dI(\epsilon)}{d\epsilon} = \pi \left[\frac{I_{max} - I_{min}}{E} \right] \frac{dH(u)}{du} \tag{C17}$$

where, with the square of the Lanczos convergence factor applied, dH(u)/du is

$$\frac{dH(u)}{du} = \left[\frac{H(2\pi) - H(0)}{2\pi} \right] + \sum_{n=1}^{N-1} a_n \left[\frac{\sin\left[\frac{n\pi}{N}\right]}{\left[\frac{n\pi}{N}\right]} \right]^2 \left[\frac{n}{2}\right] \cos\left[\frac{nu}{2}\right] \tag{C18}$$

Thus, $dI(\epsilon)/d\epsilon$ is found using Eqs. 4, 17 and 18. The formulas for higher order derivatives are given below; however, problems can be encountered with these higher order derivatives. Because of the properties of the Fourier sine series, the second derivative will be zero at the interval end points. This is not a problem if the second derivative of the function is zero; if it is not, the second derivative will not be reliably estimated near the interval end points. The latter case will also result in unreliable estimates of third and higher order derivatives. Although indiscriminate use of the formulas for higher order derivatives is cautioned against, the formula for the m^{th} derivative of I with respect to ϵ, when m is greater than or equal to 2, is given by

$$\frac{d^m I(\epsilon)}{d\epsilon^m} = \frac{1}{2} (I_{max} - I_{min}) \left[\frac{2\pi}{E}\right]^m \frac{d^m H(u)}{du^m} \tag{C19}$$

Again u is related to ϵ by Eq. 4 and the m^{th} derivative (for m greater than 1) of H with respect to u is, with the m+1 power of the Lanczos convergence factor applied,

$$\frac{d^m H(u)}{du^m} = \frac{d^m}{du^m} \left\{ \sum_{n=1}^{N-1} a_n \left[\frac{\sin\left[\frac{n\pi}{N}\right]}{\left[\frac{n\pi}{N}\right]} \right]^{m+1} \sin\left[\frac{nu}{2}\right] \right\} \tag{C20}$$

When this technique is to be applied to data pairs, Fourier sine series coefficients must be computed. This can be accomplished using the integral expression for the coefficients given in Eq. 3. Any standard numerical integration technique, such as the trapezoidal rule can be used to do this. The coefficients can also be computed using the least squares method [33] or if there are 2^L evenly spaced data points, where L is an integer, a fast sine transform [32] can be used.

A further practical concern is the number of Fourier sine coefficients needed to achieve a reasonable approximation to the function $I(\epsilon)$. A fast sine transform will return the same number of coefficients as the number of data points. The Nyquist criterion [33], which states that the sampling frequency must be at least twice as high as the highest frequency to be measured, would seem to indicate that only the first half of the coefficients should be used; however, the Lanczos convergence factor damps the high frequency terms and errors in estimating the high frequency coefficients do not significantly affect the results. This is the case through the second derivative; however, an example is given below using the third derivative which shows that using only half the coefficients can result in substantial improvement over using all the coefficients. In the examples below, unless stated otherwise, 128 data pairs are used to obtain the Fourier sine approximation and 128 coefficients are used when the series is summed.

Now that the pertinent mathematics has been discussed, examples illustrating the improved convergence achieved by using the Lanczos convergence factor and some of the possible problems with the Fourier sine series approximation will be given. The first example uses the Heavyside step function to demonstrate the improvement to the approximation due to the Lanczos convergence factor. The step function was chosen because a discontinuous function is more difficult to approximate with a Fourier sine series than a continuous function. Fig. C1 shows the step

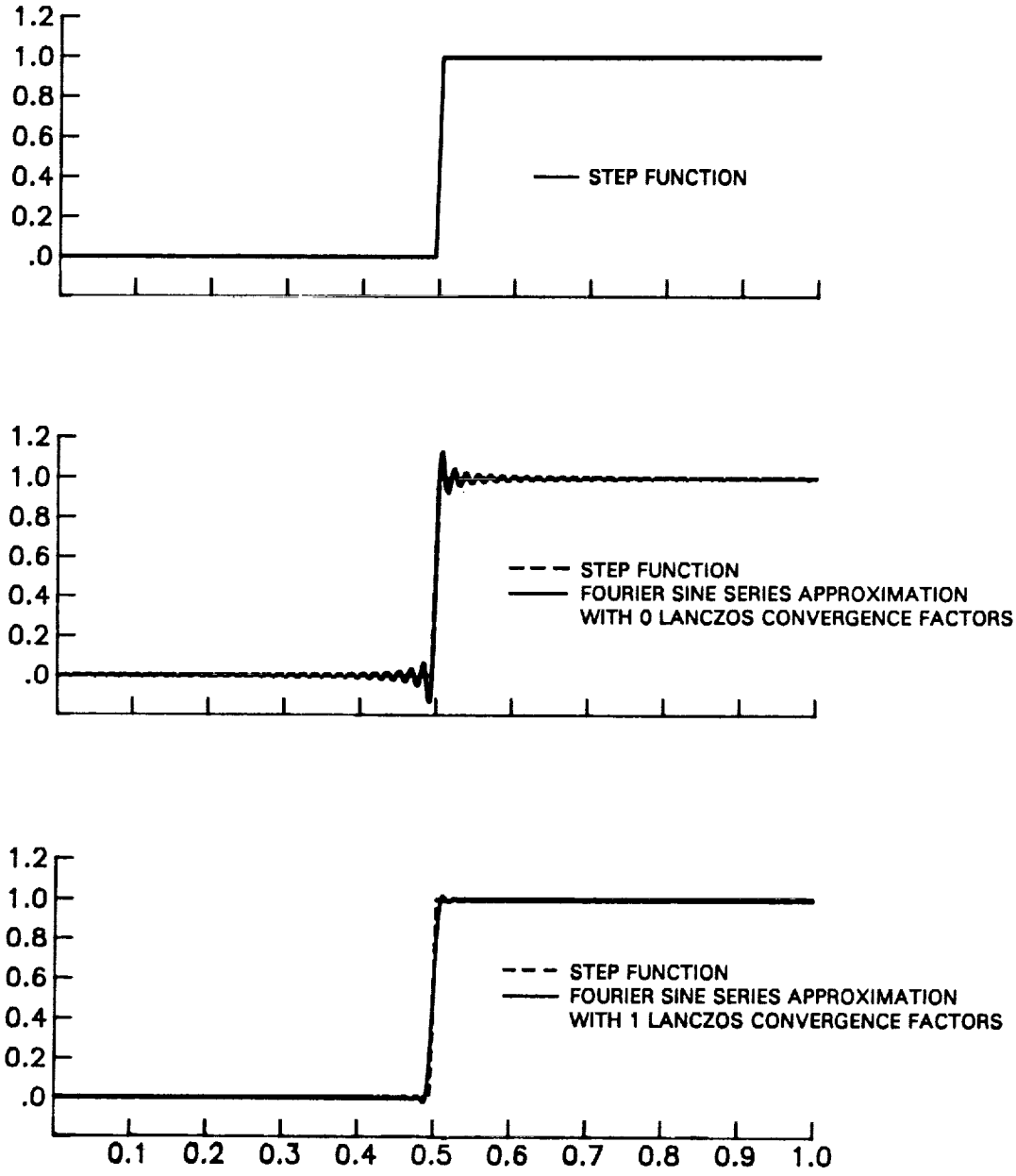

Fig. C1 Step Function and Fourier Sine Series Approximation

function (top), the Fourier sine approximation without (middle) and with (bottom) the Lanczos convergence factor applied. The Gibbs phenomenon is clearly seen in the middle trace where no Lanczos factor is used. In the bottom trace where one Lanczos convergence factor has been applied, the Gibbs phenomenon has nearly disappeared but there is some broadening at the discontinuity. Thus, it is evident that the Lanczos convergence factor ameliorates some of the problems associated with the Gibbs phenomenon and allows a reasonable approximation to the step function to be obtained.

To illustrate how the Lanczos convergence factor can be used to obtain derivatives, the first derivative of the step function was taken. Fig. C2 shows the Fourier sine series approximation of the first derivative of the step function. The top, middle and bottom traces show the approximation using 0, 1 and 2 Lanczos convergence factors, respectively. The first derivative of the step function is the Dirac delta function which is zero everywhere except at 0.5 where it spikes to infinity. Clearly none of the approximations shown in Fig. C2, exactly represent the delta function. This is the result of using a finite number of coefficients in the Fourier sine series. Considerable ringing is observed when no Lanczos factor is used (top). One Lanczos convergence factor substantially reduces the ringing (middle). Two Lanczos convergence factors virtually eliminate the ringing and therefore this is considered to produce the best approximation even though the height of the spike is reduced over those obtained using 0 or 1 Lanczos convergence factor. For the rest of the examples m+1 Lanczos convergence factors will be used to obtain the m^{th} derivative.

The next example illustrates some of the problems that can be encountered when using Fourier sine series to obtain second or higher order derivatives. The function to be approximated is the exponential function on the interval 0 to 1. All

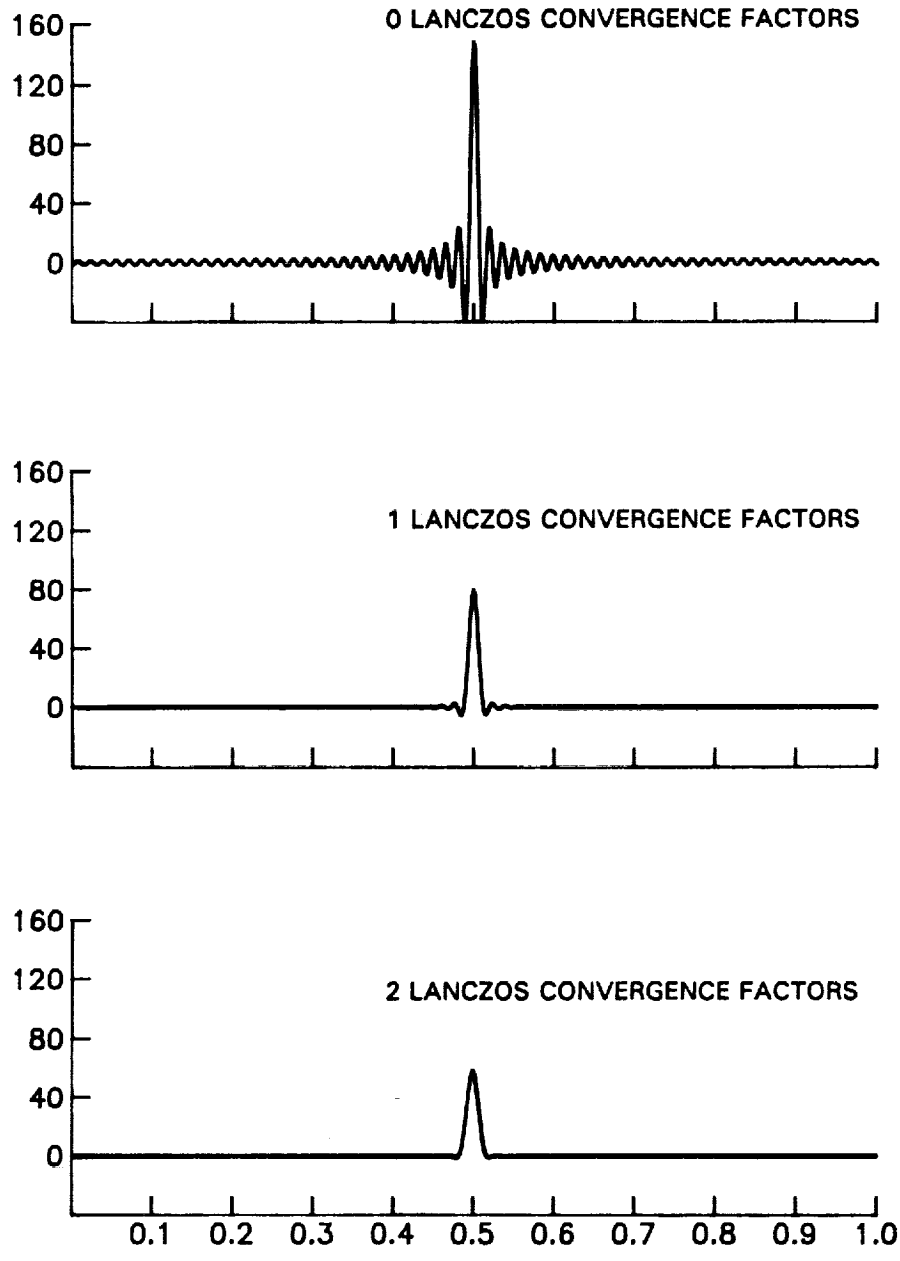

Fig. C2 Fourier Sine Series Approximation to Step Function Derivative

derivatives will again be the exponential function. Fig. C3 shows the exponential function along with the Fourier sine series representation of the function (top), as well as the first (middle) and second (bottom) derivatives. The Fourier sine series representation of the function and its first derivative are in excellent agreement. Actually, there is a slight discrepancy for the first derivative near the interval end points but it is not discernable at the scale of Fig. C3. The second derivative obtained from the Fourier sine series gives a good approximation to the function on the middle 90% of the interval but drops to zero at the interval end points. The series representation is zero at 0. The reason the series representation is not zero at 1 is that the fast sine transform used to obtain the coefficients uses one additional data spacing interval. Since 128 evenly spaced data points were used, the interval 0 to 1 is divided into 127 equal intervals. The fast sine transform uses 128 spacings, so the second derivative goes to zero at 1 + 1/127. Nonetheless, it is evident that the Fourier sine series gives a poor estimate of the second derivative near the interval end points. Therefore, in general, the second derivative should only be used on the middle 90% of the interval.

Fortunately, in most applications, third or higher order derivatives are not needed; however, an example showing some of the problems associated with obtaining a good estimate of these derivatives will be given. Fig. C4 shows the third derivative of the exponential function and the series representation obtained using 128 coefficients. The series representation spikes to a large positive value near 0 and to a large negative value near 1. This occurs because the second derivative of the series decreases to zero at the interval end points. The third derivative of the Fourier sine series is also very noisy on the interior of the interval, resulting in a poor approximation to the third derivative. As mentioned above, the Nyquist criterion suggests that better results might be obtained by using the first 64 coefficients instead

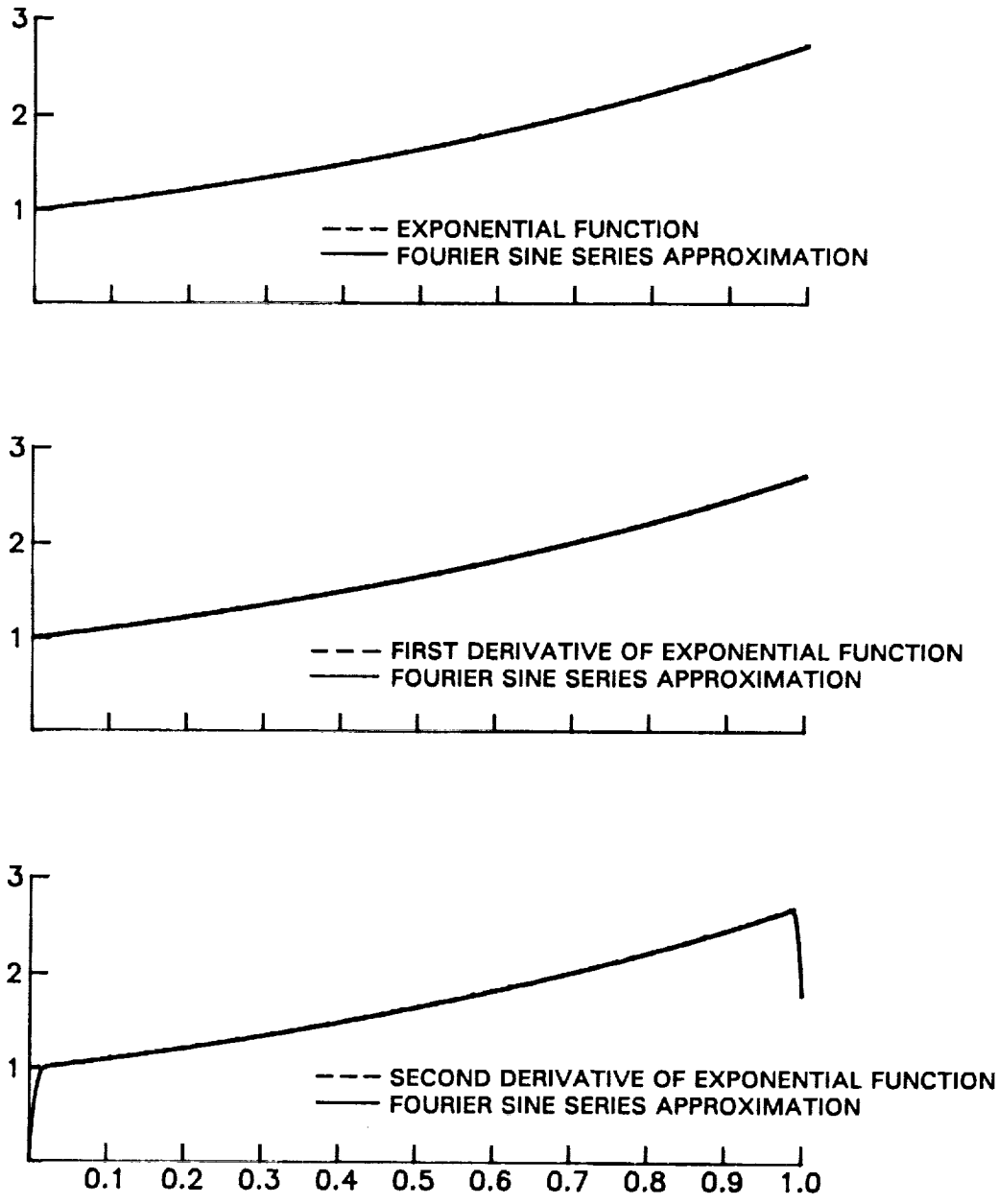

Fig. C3 Fourier Series Approximation to Exponential Function and its First Two Derivatives

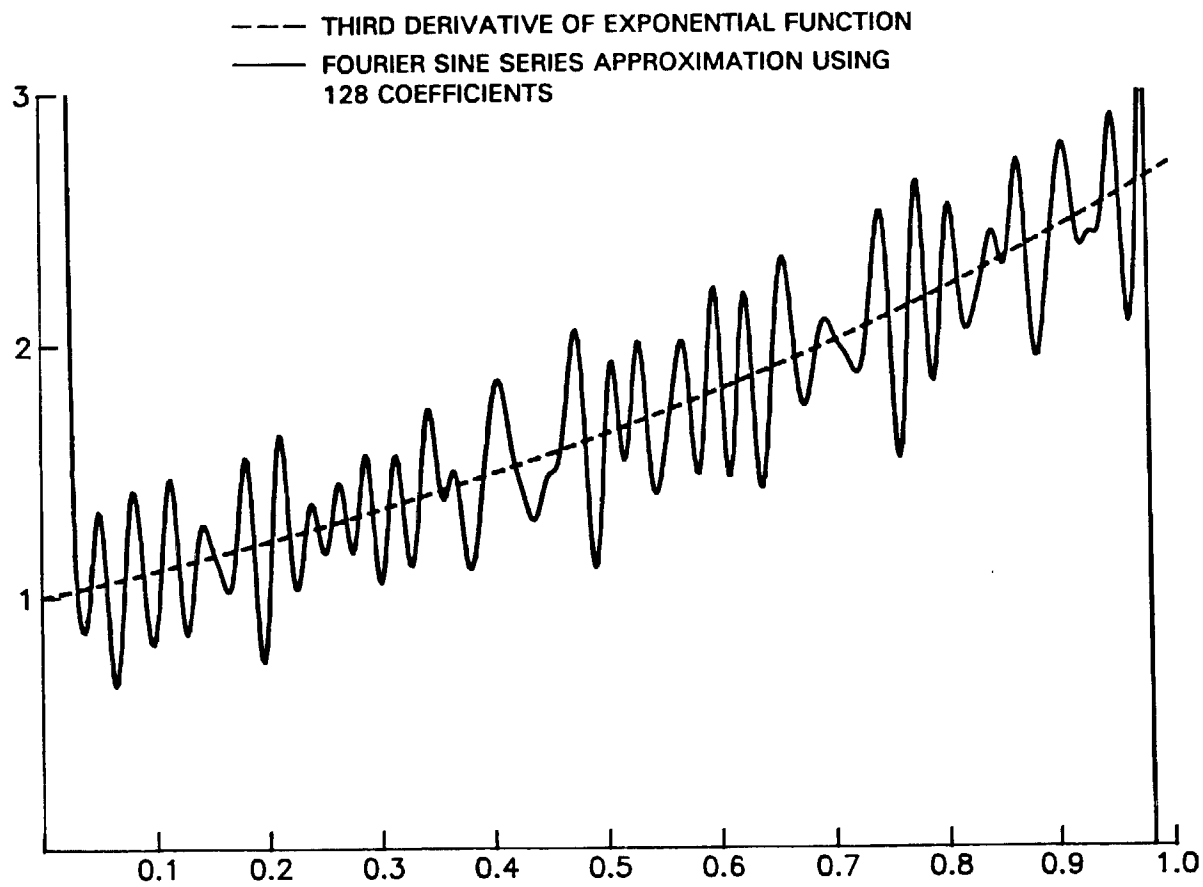

Fig. C4 Third Derivative of Exponential Function Using 128 Coefficients

of all 128. Fig. C5 shows the approximation to the third derivative using 64 coefficients. Again the derivatives spike at the interval end points, but the approximation is much less noisy away from the end points. Some ripple is still evident but it is a better approximation than that obtained using 128 coefficients.

The problems with the second and higher derivatives do not arise if these derivatives are equal to zero at the interval end points. For example, all derivatives of the step function are zero at the interval end points. Fig. C6 shows the second (top), third (middle) and fourth (bottom) derivatives of the step function using 128 coefficients. These curves are not noisy; all are seen to be reasonable approximations to the derivatives of the step function. This suggests that it might be possible to eliminate noise by artificially adding data beyond the ends of the interval in such a way that the higher order derivatives are zero at the end points of this extended data set. This has not been attempted but if good approximations to higher order derivatives are needed, it might be worth investigating.

The final example shows the result obtained when the Fourier sine series technique is applied to experimental data. A retarding potential analyzer trace is shown at the top of Fig. C7. A set of 128 raw data pairs describing this RPA trace were obtained by measuring the singly ionized (assumed) argon ion current flowing through a $3x10^{-6}$ m^2 hole onto a current sensing plate as a function of the voltage applied to the plate. The bottom plot on Fig. C7 shows the energy distribution function ($dn/d\epsilon$) obtained using Eq. 1. The derivative $dI/d\epsilon$ was obtained using a 128 term Fourier sine series with a squared Lanczos convergence factor. The resulting distribution function shown in the bottom curve is seen to be reasonable.

From these examples it is evident that use of the Fourier sine series in conjunction with the correctly applied Lanczos convergence factor does provide a useful technique for analyzing experimental data.

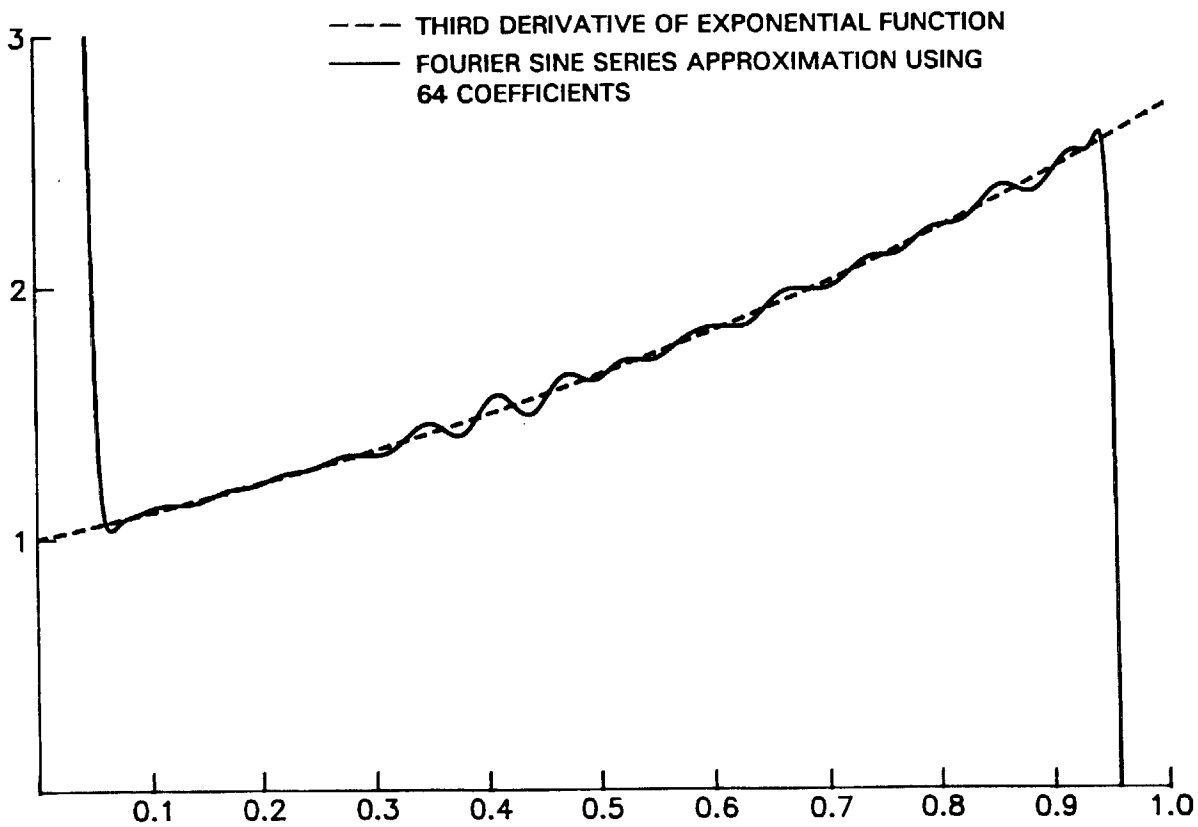

Fig. C5 Third Derivative of Exponential Function Using 64 Coefficients

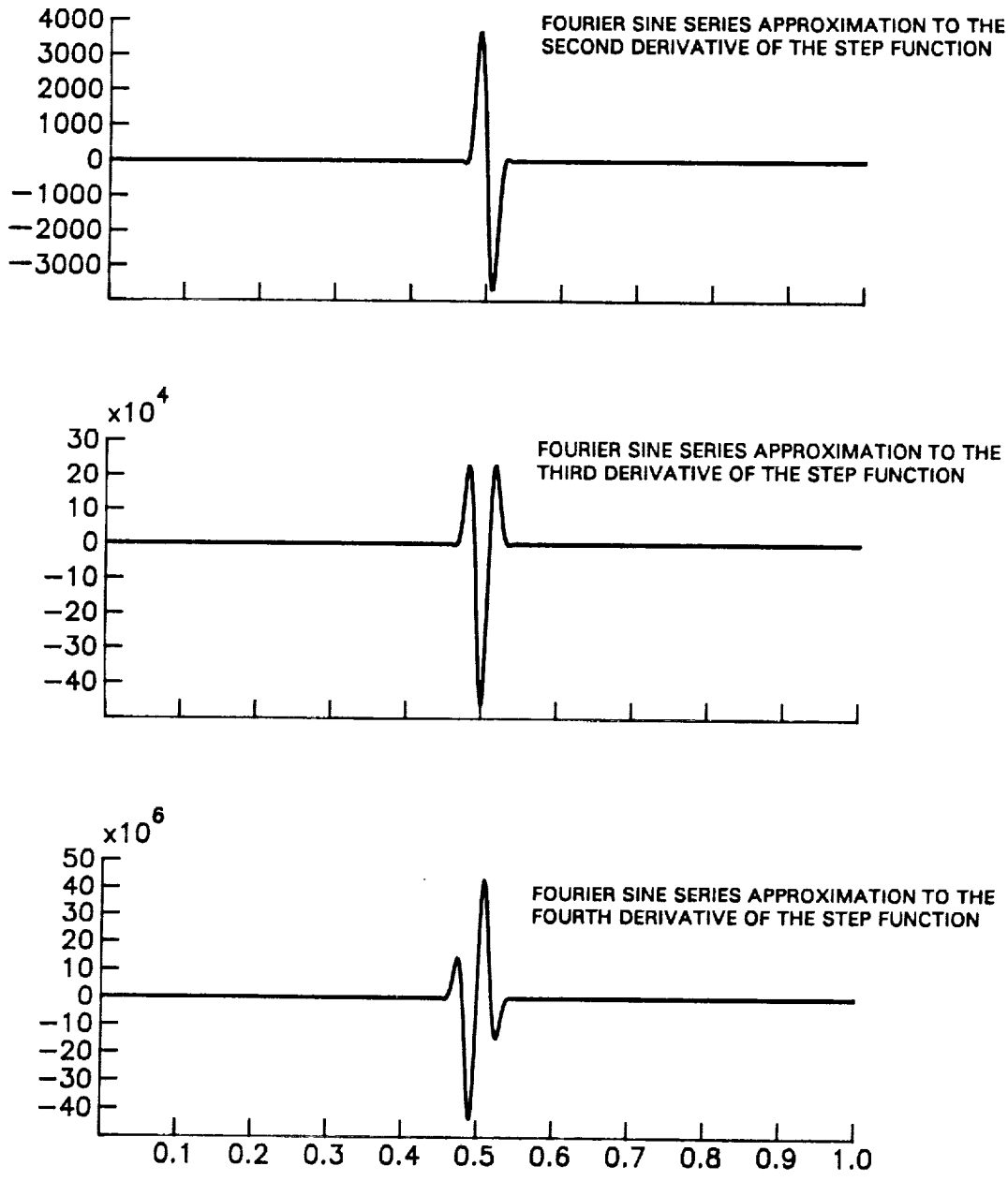

Fig. C6 Fourier Sine Series Approximation to Higher Order Derivatives of the Step Function

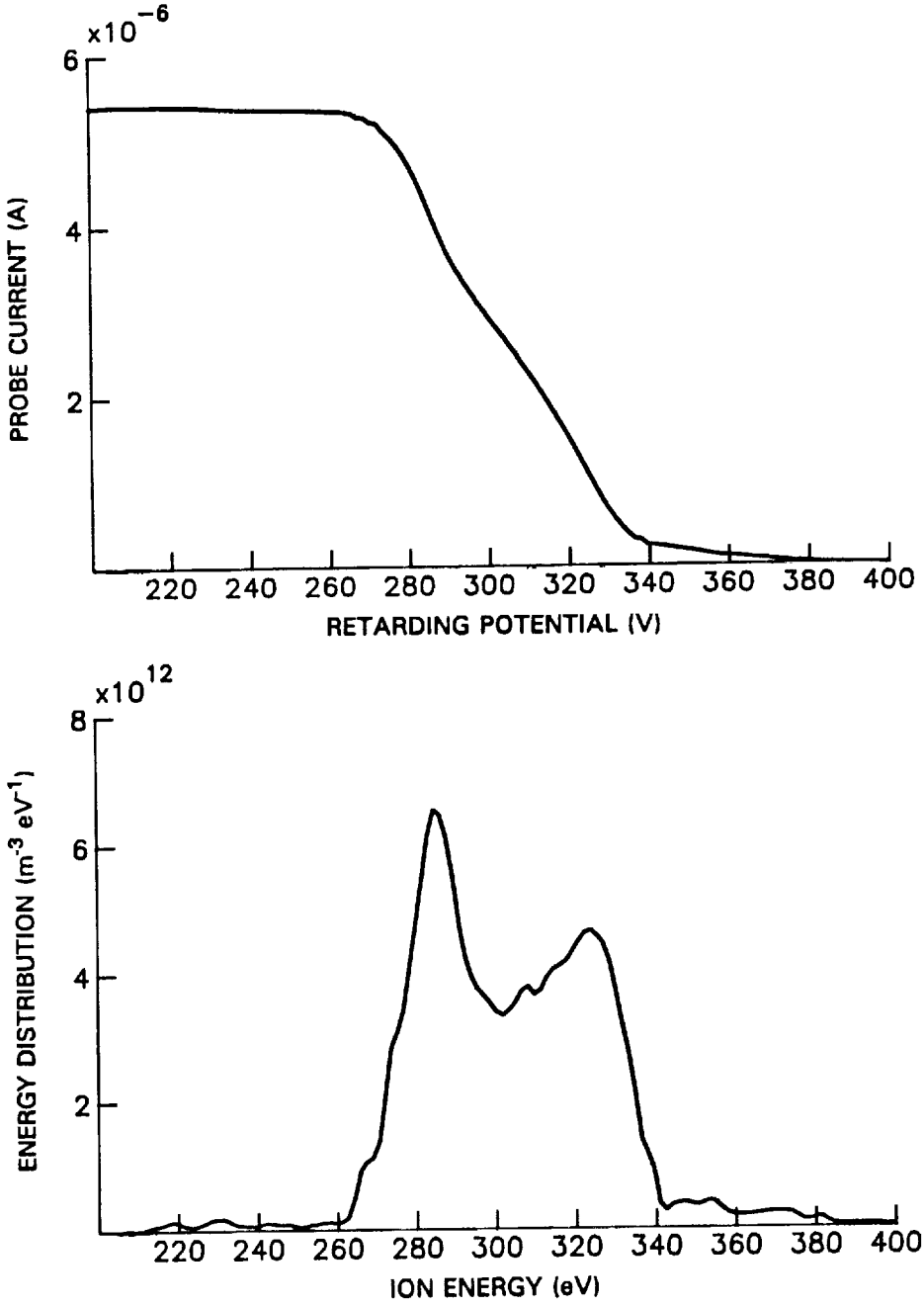

Fig. C7 RPA Trace and Corresponding Ion Energy Distribution Function

Appendix D

Nomenclature

F	Non-dimensional frequency
M	Non-dimensional mass
Q	Non-dimensional charge
T	Non-dimensional time
δ	Phase shift between sinusoidal RF signal and terminal ion energy
ν	Non-dimensional potential
ν_{RF}	Non-dimensional RF voltage amplitude
ξ	Non-dimensional kinetic energy
τ	Non-dimensional steady-state transit time for an ion to travel between grids 1 and 2
Ψ	Energy spread parameter

Appendix A

e	Electronic charge (C)
f	Frequency of sinusoidal RF voltage signal (Hz)
F	Non-dimensional frequency
m	Mass per ion (kg)
m_{O_2}	Mass of diatomic oxygen (kg)
M	Non-dimensional mass per ion
q	Charge per ion (C)
Q	Non-dimensional charge per ion
s	Spacing between adjacent grids (m)

t	Time (s)
T	Non-dimensional time
T_1	Non-dimensional time at which an ion passes grid 1
T_2	Non-dimensional time at which an ion passes grid 2
T_3	Non-dimensional time at which an ion passes grid 3
v	Ion speed (m s^{-1})
v_1	Ion speed at grid 1 (m s^{-1})
V_p	Discharge chamber plasma potential (V)
V_{RF}	RF voltage amplitude (V)
V_1	Potential applied to grid 1 (V)
V_2	Potential applied to grid 2 (V)
V_3	Potential applied to grid 3 (V)
V_{12}	Potential variation between grids 1 and 2 (V)
V_{23}	Potential variation between grids 2 and 3 (V)
x	Length (m)
$\bar{\Delta}$	Non-dimensional steady-state time for an ion to travel from a specified grid to a given point
Δ'	Non-dimensional first-order perturbation of time for an ion to travel from a specified grid to a given point
δ	Phase shift between sinusoidal RF signal and output at grid 3
ν	Non-dimensional voltage
ν_p	Non-dimensional discharge chamber plasma potential
ν_{RF}	Non-dimensional RF voltage amplitude
ν_s	Non-dimensional stopping potential
ν_1	Non-dimensional potential applied to grid 1
ν_3	Non-dimensional potential applied to grid 3
$\bar{\nu}_3$	Non-dimensional steady-state potential applied to grid 3

ν' Non-dimensional first-order perturbation of potential applied to grid 3

ν_* Non-dimensional steady-state potential required to stop ions arriving at grid 3

ν_*' Non-dimensional first-order perturbation of potential required to stop ions arriving at grid 3

ξ Non-dimensional kinetic energy

τ Non-dimensional steady-state transit time for an ion to travel between grids 1 and 2

τ' Non-dimensional first-order perturbation of time for an ion to travel between two grids

τ_* Non-dimensional steady-state transit time for an ion to travel between grids 2 and 3

Φ Stopping potential parameter

Ψ Energy spread parameter

ϑ Non-dimensional ion speed

ϑ_1 Non-dimensional ion speed at grid 1

$\bar{\vartheta}$ Non-dimensional steady-state ion speed

ϑ' Non-dimensional first-order perturbation of ion speed

☺ Non-dimensional length

$\bar{☺}$ Non-dimensional steady-state ion position

☺′ Non-dimensional first-order perturbation of ion position

Appendix B

f Fraction of repelled ions that strike inner surfaces of the Faraday cage

g Secondary electron emission coefficient

I_e Magnitude of secondary electron current emitted by the Faraday cage

I_i Ion current to the RPA collector

I_R Ion current repelled by the collector

I_{RPA} Collector current measured by the RPA ammeter

I_+ Ion current arriving at RPA collector at low retarding potentials

I_- Magnitude of secondary electron current arriving at collector when all ions are repelled

J_+ Current density measured at low retarding potentials

J_- Magnitude of current density measured at high retarding potentials

Appendix C

A Area through which current flows to the RPA collector (m^2)

e Electronic charge (C)

I Current flowing to the collector (A)

m Ion mass (kg)

ϵ Ion energy (J)

η Ion number density (m^{-3})

REPORT DOCUMENTATION PAGE

Form Approved
OMB No. 0704-0188

1. AGENCY USE ONLY (Leave blank)	2. REPORT DATE	3. REPORT TYPE AND DATES COVERED
	January 1993	Contractor Report

4. TITLE AND SUBTITLE
Discrimination of Ionic Species From Broad-Beam Ion Sources

5. FUNDING NUMBERS
G NGT-50370

6. AUTHOR(S)
J.R. Anderson

7. PERFORMING ORGANIZATION NAME(S) AND ADDRESS(ES)
Department of Mechanical Engineering
Colorado State University
Fort Collins, CO 80523

8. PERFORMING ORGANIZATION REPORT NUMBER
M-708

9. SPONSORING / MONITORING AGENCY NAME(S) AND ADDRESS(ES)
National Aeronautics and Space Administration
George C. Marshall Space Flight Center
Marshall Space Flight Center, AL 35812

10. SPONSORING / MONITORING AGENCY REPORT NUMBER
NASA CR-4483

11. SUPPLEMENTARY NOTES
Grant Monitor—M.R. Carruth
Materials and Processess Laboratory, Science and Engineering Directorate.
NASA–Marshall Space Flight Center, AL 35812

12a. DISTRIBUTION / AVAILABILITY STATEMENT
Subject Category: 72
Unclassified—Unlimited

12b. DISTRIBUTION CODE

13. ABSTRACT *(Maximum 200 words)*

The performance of a broad-beam, three-grid, ion extraction system incorporating radio frequency (RF) mass discrimination was investigated experimentally. This testing demonstrated that the system—based on a modified single-stage Bennett mass spectrometer—can discriminate between ionic species having about a 2-to-1 mass ratio while producing a broad-beam of ions with low kinetic energy (<15 eV). Testing was conducted using either argon and krypton ions or atomic and diatomic oxygen ions. A simple one-dimensional model, which ignores magnetic field and space-charge effects, was developed to predict the specie separation capabilities as well as the kinetic energies of the extracted ions. The experimental results correlated well with the model predictions. This RF mass discrimination system can be used in applications where both atomic and diatomic ions are produced, but a beam of only one of the species is desired. An example of such an application is a 5 eV atomic oxygen source. This source would produce a beam of atomic oxygen with 5 eV kinetic energy, which would be directed onto a material specimen, to simulate the interaction between the surface of a satellite and the rarefied atmosphere encountered in low-Earth orbit.

14. SUBJECT TERMS	15. NUMBER OF PAGES
Atomic Oxygen, Broad-Beam Ion Source, Mass Discrimination	124
	16. PRICE CODE: A06

17. SECURITY CLASSIFICATION OF REPORT	18. SECURITY CLASSIFICATION OF THIS PAGE	19. SECURITY CLASSIFICATION OF ABSTRACT	20. LIMITATION OF ABSTRACT
Unclassified	Unclassified	Unclassified	Unlimited